Optical Parametric Amplification: from Nonlinear Interferometry to Black Holes

A thesis presented by

Jefferson Flórez Gutiérrez

to

The Department of Physics

in partial fulfillment of the requirements for the degree of
Doctor of Philosophy
in the subject of
Physics

Centre Max Planck-uOttawa en
photonique extrême et quantique

uOttawa

Max Planck-uOttawa Centre for
Extreme and Quantum Photonics

Faculty of Science
University of Ottawa

Abstract

We explore the optical parametric amplifier, an optical device where a pump field creates a pair of lower-frequency fields: signal and idler. The pump field is usually treated classically, but this thesis focuses on scenarios where the pump must be treated quantum mechanically. One of these scenarios is the growing field of nonlinear interferometry, where the fundamental sensitivity of a probed relative phase can beat the classical bounds and reach the maximum limit allowed by quantum mechanics, the Heisenberg limit. Indeed, we show that a fully quantum nonlinear interferometer displays a Heisenberg scaling in terms of the mean number of input pump photons. This result goes beyond the well-accepted Heisenberg scaling with respect to the down-converted photons inside the interferometer, which predicts unphysical phase sensitivities starting at a particular input pump energy. Our theoretical findings are particularly useful when designing a nonlinear interferometer with bright pump fields or optimized optical parametric amplifiers for quantum metrology and quantum imaging applications.

The quantum nature of the pump field may also play a central role concerning other physical phenomena, like Hawking radiation in the context of black holes. As suggested by several authors, both the optical parametric amplifier and Hawking radiation comprise the creation of fundamental particle pairs. Thus, if the optical parametric amplifier is fully treated quantum mechanically, we may get insight into an open problem in modern physics, namely the black hole information paradox. According to this paradox, the information stored in a black hole can be destroyed once the black hole has evaporated by emitting Hawking radiation, contradicting quantum mechanics. Despite the experimental efforts to build systems that reproduce event horizons and gravitational effects in the laboratory, the evaporation of black holes due to the emission of Hawking radiation remains a challenging task. In this thesis, we experimentally investigate the impact of an evolving pump field in an optical parametric amplifier by optimizing a parametric down-conversion process. We measure the pump and signal photon number properties, finding that the pump field gets chaotic and the signal coherent when the pump displays some sizeable depletion. We arrive at similar conclusions about the pump field from its measured Wigner function. Our experiment is the first step towards a successful experiment that could suggest that information in the black hole is not destroyed but encoded in the emitted Hawking radiation starting at some point in the black hole evolution. We finally discuss further experimental improvements to investigate the parallel between the optical parametric amplifier and Hawking radiation.

Declaration of Authorship

I, Jefferson Flórez Gutiérrez, declare that the scientific research contained in this thesis is entirely my own, including, but not limited to, numerical calculations, experimental work, data processing and analysis, except where otherwise indicated by reference or acknowledgement as follows:

- This thesis was entirely supervised by Prof. J.S. Lundeen, and therefore he contributed as an advisor on every aspect of this thesis.
- The theoretical comparison in Chapter 2 was motivated by Prof. R.W. Boyd.
- The numerical calculations in Chapter 3 were additionally supervised by Dr. E. Giese, and enriched by discussions with D. Curic, S. Lemieux, Dr. L. Giner, and Prof. R.W. Boyd.
- The experimental work in Chapters 4 and 5 was also supervised by Prof. M.V. Chekhova, and supported by discussions with her group members A.M. Pérez, C. Okoth, G. Frascella, T. Santiago-Cruz, S. López-Huidobro, and P. Cutipa.
- The experimental work in Appendix C was additionally supervised by Dr. L. Giner, with the participation of N.J. Carlson and C.H. Nacke in data acquisition, optical alignment and data processing.

Signed: Jefferson Flórez Gutiérrez

Date: March 30, 2022

Acknowledgements

This thesis would not have been possible without the guidance and support from my doctoral supervisor Prof. J.S. Lundeen. His knowledge and intuition in physics were a valuable source of understanding at every stage of my research efforts. I am also in debt to Prof. M.V. Chekhova for kindly welcoming me to her research group and providing permanent advice during my visit to the Max Planck Institute for the Sciences of Light. I would also like to thank Dr. L. Giner and Dr. E. Giese for their enlightening mentoring in several aspects of this thesis.

I want to express special gratitude to all my friends who contributed to my doctoral project from the non-scientific side. Nikou, Felipe, and Marie in Ottawa, and Corina, Antonio, Markus and *Sabina* in Erlangen, Thank You All! To my colleagues, Matt, Aldo, Davor, and Guillaume at uOttawa, and Cameron, Gaetano, Tomás, Santiago and Paula at the Max Planck Institute, I appreciate the time that we shared and the lessons that I learned from each of you. Finally, special thanks to Ángela and Omar for our countless, exciting, and ongoing discussions.

The following agencies provided essential funding for the development of this thesis: Canada Research Chairs, Natural Sciences and Engineering Research Council of Canada, Canada First Research Excellence Fund, Mitacs, Departamento Administrativo de Ciencia, Tecnología e Innovación of Colombia (Colciencias), and Fundación para el futuro de Colombia (Colfuturo).

This thesis is dedicated to my beloved family, Eduardo and Luz Marina, my parents, and Andrés and Diana, my brother and sister in law.

Contents

Abstract ii

Declaration of Authorship iii

Acknowledgements iv

1 Introduction 1
- 1.1 Black holes and the information paradox . . . 1
- 1.2 Parallel with the optical parametric amplifier . . . 5
- 1.3 Solving the black hole information paradox . . . 11
- 1.4 The trilinear Hamiltonian . . . 14
- 1.5 Outline of this thesis . . . 19

2 Classical nonlinear interaction of three evolving optical fields 21
- 2.1 The nonlinear optical wave equation . . . 21
- 2.2 Difference-frequency generation with an evolving pump field . . . 23
- 2.3 Classical optical parametric amplifier . . . 29
- 2.4 Classical vs quantum optical parametric amplifier . . . 30

3 Fully quantum nonlinear interferometer 35
- 3.1 Linear vs nonlinear interferometers . . . 36
- 3.2 Overestimation of the phase sensitivity . . . 38
- 3.3 Three-mode nonlinear interferometer . . . 39
- 3.4 Phase sensitivity of a three-mode nonlinear interferometer . . . 42
- 3.5 Photon number statistics inside the interferometer . . . 46

4 Experimental quantum pump field 49
- 4.1 Parametric down-conversion . . . 49
- 4.2 Experimental setup . . . 51
- 4.3 Mean number of photons . . . 54
- 4.4 Photon number statistics . . . 57
- 4.5 Comparison with the trilinear Hamiltonian . . . 59

5 Wigner function of the pump field **62**
5.1 The Wigner function . . . 63
5.2 Balanced homodyne detection . . . 66
5.3 Balanced homodyne detection in time domain . . . 70
5.4 Homodyne detection results . . . 74
5.5 The pump field in phase space . . . 80

6 Conclusions and future directions **82**

A Purity calculation for the pump field **85**

B MATLAB code to numerically solve the trilinear Hamiltonian **88**

C A variable partially polarizing beam splitter **92**

D Parametric down-conversion angular spectrum **101**

E Making our laser pulses Fourier transform limited **103**

List of Figures **108**

List of Tables **110**

List of Abbreviations **111**

Bibliography **113**

Chapter 1

Introduction

This thesis was initially conceived in a context far away from optics, as far away as astronomical black holes. The idea of investigating these fascinating objects originated after a visit from Prof. C. Adami to our group at uOttawa in late 2016. He and his former postdoc, K. Brádler, had recently published a theoretical paper on their attempt to solve the black hole information paradox by exploiting a parallel with the optical parametric amplifier (OPA) [BA16]. The possibility of experimentally investigating the OPA to support C. Adami and K. Brádler results drove our curiosity and initiated research that took place in two different countries, Canada and Germany, over four years. Although we only obtained circumstantial evidence to solve the black hole information paradox, we investigated the OPA in detail, including one feature that authors usually dismiss: the pump's field quantum nature. As a result of this analysis, we found a fundamental limit to the sensitivity of a promising device in quantum metrology and quantum imaging, the nonlinear interferometer, implemented via two OPAs. We also revisited a theoretical formalism that is usually overlooked, the classical interaction of three evolving optical fields, and compared it with the full OPA quantum model. On the experimental side, we implemented techniques like photon counting statistics and homodyne detection to scrutinize the nature of the bright optical fields involved in the OPA when the pump dynamics must be considered. The results of this thesis have been presented in multiple scientific conferences and published in three papers so far [Fl18a; Fl18b; FLC20].

Let us start this thesis by describing our initial motivation about black holes before developing our findings in subsequent chapters.

1.1 Black holes and the information paradox

A black hole is a region in space-time containing enough mass to curve its geometry drastically [MTW73]. As a consequence of this space-time curvature, events inside the black hole cannot affect the outside universe because that would imply moving faster than light. The boundary where the interior of the black hole causally disconnects from its exterior is known as the *event horizon*. For an observer in the outside universe, any object that falls into a black hole slows down until "freezing" at the event horizon, which never crosses. The in-falling

object then looks increasingly redshifted over time until it fades from the external observer. In contrast, in the reference frame of the in-falling object, it does cross the event horizon in a finite amount of proper time and never returns.

K. Schwarzschild provided the simplest mathematical approach to black holes just after the debut of Einstein's general theory of relativity in 1915 [Sch16b; Sch16a]. Schwarzschild's solution to Einstein field equations describes the gravitational field of a non-rotating, uncharged, and static spherical object of mass M. If the radius of this object is less than the so-called Schwarzschild radius $r_S = 2GM/c^2$, then it forms a black hole, with the event horizon located at r_S. In this expression, G is the universal gravitational constant, and c is the speed of light in vacuum. The Schwarzschild radius is a relatively small length for objects in our solar system. For example, $r_S \sim 3 \times 10^3$ m and $\sim 8 \times 10^{-3}$ m for our Sun and the Earth, respectively, while their actual radii are $\sim 7 \times 10^8$ m and $\sim 6 \times 10^6$ m. This simple comparison provides an idea of how dense stellar-mass black holes (those with a few to tens of solar masses) are in reality.

A few decades later, other solutions to the Einstein field equations for rotating and electrically charged black holes were formulated [Ker63; New+65]. However, it was not until 1965 that R. Penrose (awarded the Nobel Prize in Physics 2020) and S.W. Hawking mathematically proved that black holes unavoidably form due to the gravitational collapse of massive stars, according to the general theory of relativity [Pen65; Haw67]. These theoretical advances, together with the discovery of pulsars [Hew+68] (rapidly pulsating radio sources also formed by the gravitational collapse of massive stars), paved the way to convince the scientific community about the potential existence of black holes in nature. Finally, an X-ray source known as Cygnus X-1 [Bow+65] became the first object to be widely recognized as a black hole during the early 1970s [WM72; Bol72].

In the next few decades, the community's attention focused on supermassive black holes located in galactic centres, starting with Sagittarius A*, a bright and compact radio source detected back in 1932 in the centre of our galaxy, the Milky Way [Jan32; Jan33]. A complete observational and theoretical review of the centre of the Milky Way can be found in Ref. [GEG10]. In particular, A.M. Ghez, R. Genzel (both of them also awarded the Nobel Prize in Physics 2020) and their respective teams used advanced observational techniques to track the motion of stars orbiting around Sagittarius A*. They concluded that this radio source is too small to be any object besides a black hole, with about 4 million solar masses contained within a radius of less than 0.002 light-years or 126 astronomical units [Ghe+08; Gil+09]. Similar conclusions have been drawn about the presence of supermassive black holes in the centres of a few nearby galaxies [KR95], with new supporting evidence accumulated year after year. A review of the supermassive black holes in galactic nuclei can be found in Ref. [FF05].

More recently, the black hole exploration entered a new and exciting era thanks to, on the one hand, the first detection of gravitational waves originated by the merger of two stellar-mass black holes [CC16] (awarded the Nobel Prize in Physics 2017). On the other, to the

first reported image of a supermassive black hole in the centre of the giant elliptical galaxy M87 [Col19]. These two groundbreaking contributions and promising next-level observations based on gravitational wave detectors and very-long-baseline interferometry have put black holes in the spotlight to keep unveiling the natural rules that govern our universe.

In the search for such rules, an open problem in physics is how to reconcile general relativity and quantum mechanics within the same theory. The inconsistency between these two theories can be explicitly seen in the evaporation of black holes, as we shall explain in the remaining of this section. Before the 1970s, scientists believed that black holes were at absolute zero temperature due to their lack of light emission. However, S.W. Hawking theoretically argued in 1974 that black holes are not "black" after all but emit light typical of a hot body at temperature

$$T = \frac{\hbar c^3}{8\pi G M k_B}, \tag{1.1}$$

with $\hbar$ and k_B the reduced Planck and Boltzmann constants, respectively [Haw74; Haw75]. The convergence of constants from different physics subfields, including quantum mechanics, general relativity and statistical mechanics, makes Eq. (1.1) an ideal expression to be predicted by a successful, yet undiscovered, full quantum theory of gravity.

Thermal radiation emitted by black holes, also known as *Hawking radiation* (HR), comes at the expense of a slow reduction in the black hole mass over time up to a complete evaporation [Haw74]. Consequently, the information encoded by an object that gravitationally falls into a black hole may disappear after the black hole evaporates, contradicting the unitarity of quantum mechanics that guarantees information conservation. In particular, the state of such an object cannot be recovered from HR because this is entirely random and carries no information besides the black hole temperature. Moreover, black holes are fully characterized by just three external parameters, mass, angular momentum and electric charge, according to the no-hair theorem, leaving no room to encode any in-falling object information [Car73]. So, if black holes evaporate, what happens to the information trapped in them? Is it destroyed or remains somewhere somehow? The fact that black hole evaporation may be fundamentally an irreversible process due to information loss, and therefore incompatible with quantum theory, is known in the literature as the *black hole information paradox* and highlights a discrepancy between general relativity and quantum mechanics predictions.

In practical terms, HR is complicated to detect because black holes are much colder than the universe's average temperature. For example, the temperature of a black hole with one solar mass is 6×10^{-8} K according to Eq. (1.1), while the temperature of the cosmic microwave background radiation is 2.73 K, masking HR. The lightest black hole detected so far, with around six solar masses and located at the GRO J1655-40 binary system, is even colder and its HR more challenging to detect. More challenging to observe, if not impossible, is the evaporation of a black hole since its lifetime scales with its mass cubed according to $5120\pi G^2 M^3/\hbar c^4$ [LoP03]. Thus, a black hole with one solar mass evaporates in around 10^{74} s,

assuming no extra mass is falling into the black hole during this time. This evaporation time is longer than the age of the universe, which is of the order of 10^{17} s. Consequently, we are dealing with an event that human beings may not witness in our entire life as a civilization.

Nonetheless, many possible solutions to the black hole information paradox have been proposed in the meantime. These proposed solutions can be classified in three directions of thought, namely that information is

1. lost, but this is not a problem within a quantum theory of gravity to be discovered;
2. preserved, but remains inaccessible to us in e.g. a parallel universe;
3. preserved and escapes from the black hole as it evaporates through a still unknown mechanism.

Perhaps the most conservative scenario, and the one that has received substantial attention in the last years, is the third one [Pen+19; Alm+20b; Alm+20a; HIM20; Pen20]. Some of the related solutions are based on an attempt to reconcile quantum mechanics with general relativity through a holographic principle within string theory called the AdS/CFT (Anti-de Sitter space/conformal field theory) correspondence [Mal99]. The explanation of this correspondence is far beyond the scope of this thesis. However, we can say that the AsS/CFT correspondence is a mathematical mapping analogous to a hologram that describes how a curved space-time (AdS) appears from a gravity-free quantum theory (CFT). Thus, gravity on the AdS region maps onto the quantum interactions on the CFT surface, where information is undoubtedly preserved [Alm+20b; Pen20]. However, the AdS/CFT correspondence has raised some scepticism because it relies on a controversial theory, string theory. Hence, other authors have resorted to a quantum theory of gravity based on the path integral formulation of quantum mechanics, an idea explored by S.W. Hawking [Haw78], to prove that information is preserved and remains accessible to us [Pen+19; Alm+20a].

The vast majority of authors cited so far employ a standard way to illustrate that information is preserved and escapes from the black hole, the so-called *Page curve*. In 1993, D.N. Page imagined a total system in a pure state formed by two subsystems, the black hole and the radiation field, although his reasoning is general and equally applies to any two quantum subsystems [Pag93; Pag13]. Then, he calculated the radiation von Neumann entropy [NC00] of one of the subsystems at different stages in the black hole evolution. The von Neumann entropy quantifies the amount of information encoded in the radiation field, being maximum if this subsystem is in a complete mixed state and encodes no information [Pag93]. D.N. Page found that the calculated entropy must exhibit an inverted V shape, also known as Page curve, starting at zero when the black hole just formed and has still emitted no radiation, and going back to zero *if the information is preserved* when the black hole fully evaporates. The maximum point occurs roughly halfway in the black hole evaporation, at the so-called *Page time*. We shall present an example of a Page-like curve in Sec. 1.3. A brief historical review of HR and black hole thermodynamics can be found in Ref. [Pag05].

It is in this scenario that K. Brádler et al. derived a Page-like curve for the evolution of black holes [BA16]. However, instead of using potential candidates for a quantum theory of gravity, like string theory, they took advantage of a proposed parallel between HR and the OPA with a quantum pump field. In Secs. 1.2 and 1.3, we discuss the core of this parallel in detail and expand on the theoretical results obtained so far by others.

1.2 Parallel with the optical parametric amplifier

The parallel between HR and the OPA, investigated by several authors in the last decade [NB10; Nat+12; Als15; AF16; BA16], has been motivated by some features that these two phenomena have in common, like the amplification of zero-point or vacuum fluctuations and the resulting emission of thermal radiation. Indeed, the HR-OPA parallel is not limited to only these two processes but rather has been extended to include other intriguing phenomena in modern physics, such as the Unruh and the dynamical Casimir effect [Nat+12]. At the core of these four phenomena rests a mathematical tool called the Bogoliubov transformation, which is a linear transformation in the creation and annihilation operators preserving either the commutation or anticommutation relations [Leo10]. In HR, a Bogoliubov transformation approximates the effect of curved space-time on quantum fields by smoothly connecting regions of flat space. In the OPA, a Bogoliubov transformation links input and output creation and annihilation operators, as we shall see later in this section. The Bogoliubov transformation was independently introduced by N.N. Bogoljubov and J.G. Valatin in 1958 in the context of superconductivity theory [Bog58; Val58], and has found applications in other areas like nuclear physics.

It is important to note that the HR-OPA parallel is more fundamental than some wave phenomena carefully engineered to resemble relativistic-like effects, such as those in nonlinear optics [Phi+08; Bel+10], water waves [Rou+08; Wei+11], and Bose-Einstein condensates [Lah+10], to mention a few [JWK20]. In other words, the OPA study in this thesis is not intended to mimic HR like in some of these analogues but instead to exploit an underlying connection with HR by treating the full OPA quantum mechanically.

The best way to illustrate the HR-OPA parallel is using a heuristic picture of HR. Quantum field theory, and more precisely the Heisenberg uncertainty principle, allows the random creation of particle-antiparticle pairs that most of the time self-annihilate. However, if one of these pairs is created close enough to the event horizon of a black hole, one particle from the pair can gravitationally fall into the black hole. At the same time, the other one remains outside the event horizon. The particles outside the event horizon whose counterparts are inside can escape the black hole gravitational pull, giving rise to HR. In the OPA, a similar pair creation process takes place when a single optical field, the pump field, amplifies vacuum fluctuations in the presence of a nonlinear dielectric material [LYS61]. The resulting photon pairs, historically known as signal and idler, are generated in optical modes that display a

thermal distribution when looked independently from each other, just like HR. Therefore, one of these photons, let us say the signal, plays the role of a particle in the HR, while the idler corresponds to the in-falling particle.

It is important to remember that the HR-OPA comparison is a tool to better understand a more complicated problem at the expense of simplifying it. For example, the event horizon resulting from a curved space-time is absent in the OPA. Likewise, it is not clear what exactly in the black hole is modelled by the pump field, how to quantify the number of modes the black hole emits into, and the role played by the particle fields that remain outside the event horizon. The proposed parallel is just an ad-hoc model pursuing the idea that information is not destroyed but instead encoded in the HR at later stages in the black hole evolution. More importantly, it is susceptible to be tested in the laboratory, given the elusive observation of black hole evaporation. With this possibility in mind, we describe our attempt to experimentally study the HR-OPA parallel in Chapters 4 and 5, and discuss in Chapter 6 further experimental conditions where this comparison can be tested.

To expand on the HR-OPA parallel, we shall look at the simplest theoretical model that describes a non-degenerate OPA, where signal and idler photons are produced in two different modes. A degenerate OPA, where signal and idler photons are produced in the same mode such that they are no longer distinguishable, is not considered here. Moreover, this thesis focuses on the parametric amplifier operating at optical frequencies, although most of our theoretical descriptions apply well to any other frequency range.

The dynamics of the signal and idler modes are dictated by a bilinear Hamiltonian, where an undepleted classical field associated with a constant complex number rather than a quantum operator approximates the pump field. This approximation for the pump field, known as the *parametric approximation*, is justified by the low conversion efficiencies exhibited by the OPA in most common experimental scenarios, where approximately only one out of 10^{12} pump photons down-converts into a signal and idler photon pair on average. Thus, the pump remains unchanged by the process, making it unnecessary to deal with its dynamics. In the interaction picture, the bilinear Hamiltonian resulting from the parametric approximation reads [LYS61]

$$\hat{H}_{\mathrm{bi}} = \hbar\sqrt{N_p}\kappa e^{i\theta}\hat{b}^\dagger\hat{c}^\dagger + \mathrm{h.c.} \tag{1.2}$$

In this expression, N_p is the mean number of pump photons, $\hat{b}^\dagger$ and $\hat{c}^\dagger$ are the creation operators for the signal and idler modes, respectively, h.c. stands for hermitian conjugate, and $\kappa e^{i\theta}$ is a complex coupling constant with magnitude κ proportional to the optical nonlinearity of the material, and argument θ equal to the relative phase between the pump and down-converted fields. In this thesis, we consider the general case of an arbitrary relative phase θ, in contrast to several textbooks where $\theta = \pi/2$, as in Refs. [GK04; WM08]. This generalization will be useful in Chapter 3, where we investigate nonlinear interferometers. We will derive in detail a more general Hamiltonian in Sec. 1.3, where the pump is no longer a constant complex number

but a quantized field.

The evolution of the operators $\hat{b}$ and $\hat{c}^\dagger$ can be found analytically in the interaction picture, starting with the Heisenberg equations of motion [WM08]

$$i\hbar\frac{d\hat{b}}{dt} = [\hat{b}, \hat{H}_{\rm bi}] = \hbar\sqrt{N_p}\kappa e^{i\theta}\hat{c}^\dagger,$$
$$i\hbar\frac{d\hat{c}^\dagger}{dt} = [\hat{c}^\dagger, \hat{H}_{\rm bi}] = -\hbar\sqrt{N_p}\kappa e^{-i\theta}\hat{b}.$$

The solution to these equations is a *Bogoliubov transformation* for the initial operators in the form

$$\begin{bmatrix}\hat{b}(t)\\ \hat{c}^\dagger(t)\end{bmatrix} = \begin{bmatrix}\cosh\Gamma & -ie^{i\theta}\sinh\Gamma\\ ie^{-i\theta}\sinh\Gamma & \cosh\Gamma\end{bmatrix}\begin{bmatrix}\hat{b}(0)\\ \hat{c}^\dagger(0)\end{bmatrix}, \tag{1.3}$$

where we have introduced the so-called *parametric gain* $\sqrt{N_p}\kappa t \equiv \Gamma$, with $0 \leq \Gamma < \infty$. Please keep in mind that Γ depends on t, although we do not express this dependence explicitly to simplify our notation.

We can show that the Bogoliubov transformation in Eq. (1.3) preserves the commutation relations [Leo10]

$$[\hat{b}(t), \hat{c}^\dagger(t)] = 0 = [\hat{b}(t), \hat{c}^\dagger(t)],$$
$$[\hat{b}(t), \hat{b}^\dagger(t)] = 1 = [\hat{c}(t), \hat{c}^\dagger(t)],$$

among other interesting mathematical properties that we briefly define in Chapter 3 in relation to the SU(1,1) group.

If the signal and idler modes are initially in vacuum, i.e. if both $\langle\hat{b}^\dagger(0)\hat{b}(0)\rangle \equiv N_s$ and $\langle\hat{c}^\dagger(0)\hat{c}(0)\rangle \equiv N_i$ identically vanish, with N_s and N_i the initial number of signal and idler photons, respectively, the solution in Eq. (1.3) predicts an exponential behaviour in the mean number of photons given by

$$\langle\hat{b}^\dagger(t)\hat{b}(t)\rangle = \sinh^2\Gamma = \langle\hat{c}^\dagger(t)\hat{c}(t)\rangle, \tag{1.4}$$

as shown later in Fig. 1.1. This initial condition over the signal and idler modes defines the *spontaneous case*, and Eq. (1.4) is interpreted as the amplification of vacuum fluctuations in the presence of a nonlinear material [LYS61]. This vacuum amplification has no classical counterpart, as we shall discuss in Chapter 2.

More generally, for arbitrary initial conditions N_s, $N_i \geq 0$, we arrive to [LYS61]

$$\langle\hat{b}^\dagger(t)\hat{b}(t)\rangle = N_s\cosh^2\Gamma + N_i\sinh^2\Gamma + \sinh^2\Gamma, \tag{1.5}$$

$$\langle\hat{c}^\dagger(t)\hat{c}(t)\rangle = N_s\sinh^2\Gamma + N_i\cosh^2\Gamma + \sinh^2\Gamma. \tag{1.6}$$

In Sec. 1.4 and Chapter 2, we compare the mean number of signal photons in Eq. (1.5)

for several initial conditions, including the spontaneous case, with a full OPA quantum and classical model, respectively.

The OPA plays a central role in quantum optics not only because it amplifies vacuum fluctuations, but because this amplification generates a special kind of quantum states, the so-called *squeezed states* [Tak65; MG67]. To describe squeezed states, we first define the concept of field quadratures, which are the real and imaginary components of the electric field. By following the definitions and derivations in Ref. [GK04] in the remaining of this section, the field quadratures of a two-mode field can be defined as

$$\hat{X}_1 = \frac{1}{\sqrt{2^3}}\left(\hat{b} + \hat{b}^\dagger + \hat{c} + \hat{c}^\dagger\right), \tag{1.7}$$

$$\hat{X}_2 = \frac{1}{i\sqrt{2^3}}\left(\hat{b} - \hat{b}^\dagger + \hat{c} - \hat{c}^\dagger\right). \tag{1.8}$$

These are not standard quadratures since they combine operators of the two modes. However, they satisfy all the mathematical properties of standard quadratures, like the commutation relation $[\hat{X}_1, \hat{X}_2] = i/2$. In Chapter 5, we define the field quadratures in the simpler case of a single-mode field. Now, the temporal evolution of the bilinear Hamiltonian, dictated by the unitary operator

$$\hat{U}_{\rm bi}(t) = \exp\left(-i\hat{H}_{\rm bi}t/\hbar\right),$$

and the Bogoliubov transformation in Eq. (1.3), allows us to obtain the useful identities

$$\hat{U}^\dagger_{\rm bi}(t)\hat{b}(t)\hat{U}_{\rm bi}(t) = \hat{b}(0)\cosh\Gamma - ie^{i\theta}\hat{c}^\dagger(0)\sinh\Gamma, \tag{1.9}$$

$$\hat{U}^\dagger_{\rm bi}(t)\hat{c}(t)\hat{U}_{\rm bi}(t) = -ie^{i\theta}\hat{b}^\dagger(0)\sinh\Gamma + \hat{c}(0)\cosh\Gamma. \tag{1.10}$$

In the context of squeezing, the unitary operator $\hat{U}_{\rm bi}(t)$ and the parametric gain Γ are known as the two-mode squeezed operator and the squeeze parameter, respectively. With the help of identities (1.9) and (1.10), it is possible to show that the quantum state resulting from the action of $\hat{U}_{\rm bi}(t)$ over the vacuum state $|0\rangle_b|0\rangle_c \equiv |0,0\rangle$ in the interaction picture,

$$\hat{U}_{\rm bi}(t)|0,0\rangle = \frac{1}{\cosh\Gamma}\sum_{\nu=0}^{\infty}(-i)^\nu e^{i\nu\theta}\tanh^\nu\Gamma|\nu,\nu\rangle \equiv |\psi_{\rm bi}(t)\rangle, \tag{1.11}$$

satisfies $\langle\hat{X}_1\rangle = 0 = \langle\hat{X}_2\rangle$, and

$$\mathrm{Var}(\hat{X}_1) = \frac{1}{4}\left(\cosh^2\Gamma + \sinh^2\Gamma + 2\sinh\Gamma\cosh\Gamma\sin\theta\right),$$

$$\mathrm{Var}(\hat{X}_2) = \frac{1}{4}\left(\cosh^2\Gamma + \sinh^2\Gamma - 2\sinh\Gamma\cosh\Gamma\sin\theta\right).$$

For $\theta = \pi/2$, the quadrature variances become

$$\mathrm{Var}(\hat{X}_1) = \frac{1}{4}e^{2\Gamma}, \tag{1.12}$$

$$\mathrm{Var}(\hat{X}_2) = \frac{1}{4}e^{-2\Gamma}, \tag{1.13}$$

which describe a reduction (squeezing) in one of the quadrature variances, $\mathrm{Var}(\hat{X}_2)$, at the expense of an increase (stretching) in the conjugate quadrature variance, $\mathrm{Var}(\hat{X}_1)$, as a function of Γ. Therefore, the quantum state $|\psi_{\mathrm{bi}}(t)\rangle$ in Eq. (1.11) defines a quadrature squeezed state of the two modes signal and idler. Moreover, the variances in Eqs. (1.12) and (1.13) saturate the Heisenberg uncertainty relation

$$\mathrm{Var}(\hat{X}_1)\mathrm{Var}(\hat{X}_2) \geq \frac{1}{16},$$

for two non-commuting operators satisfying $[\hat{X}_1, \hat{X}_2] = i/2$. Therefore, the two-mode squeezed state $|\psi_{\mathrm{bi}}(t)\rangle$ is an example of a minimum uncertainty state. For values of θ different from $\pi/2$, it is possible to redefine the two-mode field quadratures in Eqs. (1.7) and (1.8) by diagonalizing a quadrature covariance matrix [OKL02; FT20], so that we can observe the same type of stretching and squeezing as in Eqs. (1.12) and (1.13), respectively.

The quantum state $|\psi_{\mathrm{bi}}(t)\rangle$ also exhibits a strong intermodal photon number correlation, as can be seen from the non-factorability of the modes $\hat{b}$ and $\hat{c}$ in Eq. (1.11). Indeed, we can calculate the density matrix for each of these modes by tracing out the degrees of freedom of the partner mode, i.e.

$$\hat{\rho}_b = \mathrm{Tr}_c\left(|\psi_{\mathrm{bi}}(t)\rangle\langle\psi_{\mathrm{bi}}(t)|\right) = \frac{1}{\cosh^2\Gamma}\sum_{\nu=0}^{\infty}\tanh^{2\nu}\Gamma|\nu\rangle_b\langle\nu|_b, \tag{1.14}$$

$$\hat{\rho}_c = \mathrm{Tr}_b\left(|\psi_{\mathrm{bi}}(t)\rangle\langle\psi_{\mathrm{bi}}(t)|\right) = \frac{1}{\cosh^2\Gamma}\sum_{\nu=0}^{\infty}\tanh^{2\nu}\Gamma|\nu\rangle_c\langle\nu|_c, \tag{1.15}$$

and then, calculate the corresponding von Neumann entropy $S(\hat{\rho}) = -\mathrm{Tr}(\hat{\rho}\ln\hat{\rho})$,

$$S(\hat{\rho}_b) = -\sum_{\nu=0}^{\infty}\frac{\tanh^{2\nu}\Gamma}{\cosh^2\Gamma}\ln\left[\frac{\tanh^{2\nu}\Gamma}{\cosh^2\Gamma}\right] = S(\hat{\rho}_c). \tag{1.16}$$

For a composite system like the OPA, with the signal and idler modes as subsystems, the von Neumann entropy is an entanglement quantifier, which vanishes if the subsystems are completely uncorrelated, or reduces to a positive real number depending on the degree of entanglement [NC00]. As shown in Fig. 1.1, the entropies $S(\hat{\rho}_b)$ and $S(\hat{\rho}_c)$ grow monotonically as a function of Γ, starting at zero for $\Gamma = 0$ when both modes are in uncorrelated vacuum states. Therefore, as the von Neumann entropy increases with Γ, the entanglement between the signal and idler modes increases as well.

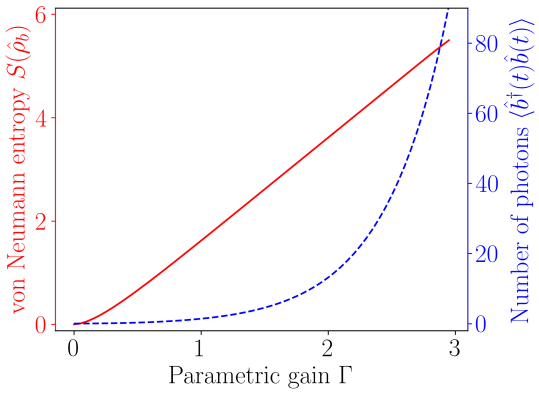

FIGURE 1.1: von Neumann entropy (red solid) and number of photons (blue dashed) in the signal mode $\hat{b}$ of an optical parametric amplifier operating in the spontaneous case. The idler mode $\hat{c}$ displays exactly the same features as $\hat{b}$, according to Eqs. (1.16) and (1.4), respectively.

The von Neumann entropy also quantifies how mixed a quantum state is, starting at zero if it is a pure quantum state, like $|\psi_2(t)\rangle$ for all $0 \leq \Gamma < \infty$. In contrast, the signal and idler modes are in a mixed state when looked independently, according to the result in Eq. (1.16) for $\Gamma > 0$. To describe the signal and idler mixed state, we calculate the probability of finding n photons in each of these modes,

$$P_n^{(b)} = \langle n|_b \hat{\rho}_b |n\rangle_b = \frac{\tanh^{2n}\Gamma}{\cosh^2\Gamma} = \langle n|_c \hat{\rho}_c |n\rangle_c = P_n^{(c)}.$$

Now, by rewriting the resulting probabilities in terms of $\sinh^2\Gamma$, which is the mean number of photons according to Eq. (1.4), we arrive to

$$P_n^{(b)} = \frac{\sinh^{2n}\Gamma}{(1+\sinh^2\Gamma)^{n+1}} = P_n^{(c)}. \tag{1.17}$$

The probability in Eq. (1.17) is exactly the probability of finding n photons in a single-mode thermal field with effective temperature [YP87; Kly88]

$$T_{\text{eff}} = \frac{\hbar\omega}{2k_B \ln(\coth\Gamma)}, \tag{1.18}$$

where ω is the field angular frequency. Therefore, the signal and idler modes are both in a thermal state with effective temperature T_{eff} and angular frequency ω_s or ω_i, depending on the field, if these modes are observed independently.

We have arrived at one of the features that the OPA and black holes have in common,

namely the thermal nature of both the signal (or idler) field and HR, each of them with temperatures given in Eqs. (1.18) and (1.1), respectively. However, it is important to mention that the thermal nature of the signal field in the case of the OPA manifests in the photon number distribution and not in the signal frequency spectrum. In other words, the superposition of number states $|\nu\rangle_b\langle\nu|_b$ in Eq. (1.14) is dictated by the classical probabilities $P_\nu^{(b)}$ in Eq. (1.17), which correspond to a thermal state, but the signal field does not display a blackbody spectrum. Instead, its frequency spectrum is determined by energy and momentum conservation conditions in the OPA, the so-called phase-matching conditions, that we shall mention in Sec. 1.3 and describe in more detail in Chapter 4.

In summary, the bilinear Hamiltonian, which describes the OPA under the parametric approximation, produces a two-mode state whose degree of quadrature squeezing, entanglement between the signal and idler modes, and photon number thermal distribution depends on the parametric gain Γ. In Sec. 1.3, we review the OPA beyond the parametric approximation, i.e. when the quantum nature of the pump is taken into account, and how this approach can provide some clues to solve the black hole information paradox.

1.3 Solving the black hole information paradox

The main limitation of Hawking's original derivation is that the black hole remains stationary while emitting HR, i.e. its dynamics are neglected. Any theory that considers the evolution of the black hole would potentially predict where the information goes once it evaporates. In the absence of such a theory, authors like K. Brádler et al. have postulated that a quantum pump field in the OPA may resemble an evaporating black hole. As described in this section, they have demonstrated a Page-like curve for the pump field, bringing insight into the black hole information paradox.

The inclusion of a quantum pump field in the OPA theory is seldomly done within the quantum optics community due to the low conversion efficiency in most OPA implementations, as commented before. However, this low conversion efficiency has not been an obstacle in the vast majority of quantum applications running at the single- or few-photon level, like in quantum computing [KLM01], cryptography [Urs+07], imaging [Str+95], metrology [Nas+03], and fundamental aspects of quantum mechanics [HOM87]. The second reason for not considering pump dynamics is that the mathematical treatment for the interaction of two optical fields, the signal and idler [LYS61], is notably more straightforward than for three fields, including the pump. Nevertheless, full classical (analytical) [Arm+62], and quantum (numerically exact) [WB70; BP70] models for the interaction of these three fields have been available almost since the early 1960s. We present a thorough analysis of the classical interaction of three evolving optical fields in Chapter 2, while we discuss the equivalent quantum analysis in this section and Sec. 1.4.

To incorporate the quantum nature of the pump field into the OPA theory, we must investigate the interaction of the pump, signal and idler fields without resorting to the parametric approximation. Let us start by reviewing the response of a dielectric material to an electric field presented in Ref. [TW69]. This response, described by a polarization vector $\hat{\mathbf{P}}(\mathbf{r},t)$, can be expanded in powers of the instantaneous electric field $\hat{\mathbf{E}}(\mathbf{r},t)$ [Blo65],

$$\hat{\mathbf{P}}(\mathbf{r},t) = \epsilon_0 \left[\chi^{(1)} \cdot \hat{\mathbf{E}}(\mathbf{r},t) + \chi^{(2)} : \hat{\mathbf{E}}(\mathbf{r},t)\hat{\mathbf{E}}(\mathbf{r},t) + \cdots\right] \equiv \hat{\mathbf{P}}^{(1)}(\mathbf{r},t) + \hat{\mathbf{P}}^{(2)}(\mathbf{r},t) + \cdots,$$

where $\chi^{(1)}$ is a second-rank tensor known as the linear susceptibility, $\chi^{(2)}$ is a third-rank tensor known as the second-order nonlinear susceptibility, and so on. The double dot symbol (:) is equivalent to the following element-wise product,

$$P_i^{(2)}(\mathbf{r},t) = \epsilon_0 \sum_{jk} \chi_{ijk}^{(2)} E_j(\mathbf{r},t) E_k(\mathbf{r},t),$$

with $i,j,k = 1,2,3$ vector component labels. The time-dependent Hamiltonian describing the nonlinear interaction of the material with the electric field is given by

$$\hat{H}_{\text{int}}(t) = -\epsilon_0 \int \hat{\mathbf{E}}^{\dagger}(\mathbf{r},t) \cdot \hat{\mathbf{P}}^{(2)}(\mathbf{r},t) d^3\mathbf{r}. \tag{1.19}$$

Now, the electric field can be expanded in terms of normal modes in the form

$$\hat{\mathbf{E}}(\mathbf{r},t) = i \sum_k \mathbf{e}_k \left(\frac{\hbar\omega_k}{2V\epsilon_k}\right)^{1/2} \left(\hat{a}_k e^{i(\mathbf{k}\cdot\mathbf{r}-\omega_k t)} - \hat{a}_k^{\dagger} e^{-i(\mathbf{k}\cdot\mathbf{r}-\omega_k t)}\right), \tag{1.20}$$

with V a normalization volume, ϵ_k the dielectric constant evaluated at frequency ω_k, $\mathbf{e}_k$ a unit polarization vector, $\mathbf{k}$ the wave vector, and the sum running over all possible field modes k. The operators $\hat{a}_k$ and $\hat{a}_k^{\dagger}$ satisfy the bosonic commutation relations

$$[\hat{a}_k, \hat{a}_{k'}] = 0 = [\hat{a}_k^{\dagger}, \hat{a}_{k'}^{\dagger}],$$
$$[\hat{a}_k, \hat{a}_{k'}^{\dagger}] = \delta_{k,k'}.$$

If we substitute Eq. (1.20) into Eq. (1.19), the creation and annihilation operators in each of the fields in Eq. (1.20) lead to a Hamiltonian of the form

$$\hat{H}_{\text{tri}} = \hbar\kappa e^{i\theta} \hat{a}\hat{b}^{\dagger}\hat{c}^{\dagger} + \text{h.c.} \tag{1.21}$$

where $\hat{a}$ is the annihilation operator for the pump field, and the second-order susceptibility $\chi^{(2)}$ has reduced to a scalar proportional to the coupling constant κ. Therefore, κ quantifies the nonlinear interaction of the three fields within the material. In Eq. (1.21), we have kept the term with no time dependence, i.e. the term with perfect energy and momentum conservation, in which all the exponential factors in the fields vanish. At optical frequencies, the other terms

in the Hamiltonian will oscillate quickly compared to the optical frequency, and thus their effect tends to average to zero over many optical cycles.

The Hamiltonian in Eq. (1.21) is known in the literature as the *trilinear Hamiltonian* and can be diagonalized in a number state basis [WB70], as we shall review in Sec. 1.4. The energy and momentum conservation expressions, known as phase-matching conditions, read $\omega_1 + \omega_2 = \omega_3$ and $\mathbf{k}_1 + \mathbf{k}_2 = \mathbf{k}_3$, where the subscripts 1, 2, and 3 refer to the signal, idler and pump fields, respectively, as we will discuss in Chapter 4 in connection with the parametric down-conversion process.

In the context of the HR-OPA parallel, and based on the Hamiltonian in Eq. (1.21), P.D. Nation et al. observed that the signal field deviates from thermal radiation when around half of the pump has depleted [NB10]. As the authors claim, this supports the idea that HR encodes information about the black hole at late times in its evolution, as predicted by D. Page via the Page curve. Moreover, they found that the pump becomes entangled with the signal and idler fields, suggesting that HR is entangled with the quantized black hole internal degrees of freedom. This tripartite entanglement has been numerically studied for the OPA via the trilinear Hamiltonian dynamics for a few numbers of pump photons [DJB93] and has been explored experimentally [Cas+07]. The novelty here is that recent work on the AdS/CFT correspondence reported on a deep connection between radiation and the black hole around the Page time [Alm+19], similar to the one predicted for the OPA. These results support the idea that the black hole interior must be taken into account when studying HR since it contains information linked to the radiation.

In contrast to P.D. Nation et al., K. Brádler et al. presented a non-oscillatory black hole entropy based on a "non-continuous" unitary evolution of the total system, which is composed by the black hole and the radiation fields [BA16]. In particular, these authors calculated the total system state at time $t = N\Delta t$ after N finite time slices of duration Δt. In each time slice, the unitary evolution of the total system is given by the trilinear Hamiltonian, starting with the black hole in the Fock state $|N_p\rangle_a$ at $t = 0$, where $N_p = 1, 2, 3, \ldots$ is the initial number of pump photons, and the radiation fields in the vacuum state $|0\rangle_b|0\rangle_c$ at every slice. Since the black hole gradually "decouples" from the radiation fields after each time slice, this method is called one-shot decoupling, which has multiple applications both in physics and information theory [Dup+14]. The resulting black hole von Neumann entropy after each time slice, reproduced in Fig. 1.2, closely resembles the Page curve. According to this result, the von Neumann entropy gradually increases as the black hole slowly depletes, leading to HR with a thermal nature. Later, when roughly half of the initial black hole has evaporated, the corresponding entropy is reduced by encoding information into the HR that now deviates from a thermal state. In the end, the black hole approaches the vacuum state with zero entropy. Thus, the information is not lost but instead emitted by the black hole at late times of its evaporation. In Appendix A we study the black hole evolution in terms of its purity, arriving at similar conclusions.

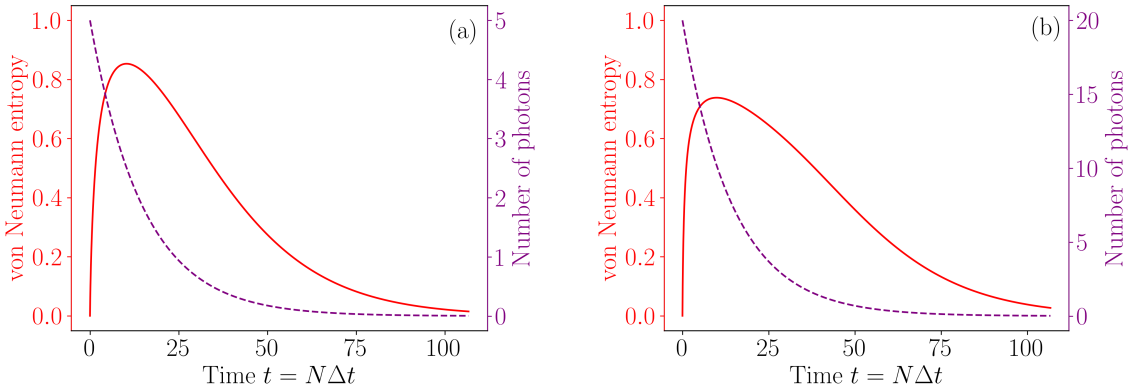

FIGURE 1.2: Black hole von Neumann entropy (red solid) from the one-shot decoupling method for $\Delta t = 1/15$ and $N_p = 5$ (a) and $N_p = 20$ (b), reproduced after K. Brádler et al. [BA16]. The von Neumann entropy has been normalized to $\ln(N_p{+}1)$, which is its maximum value. We also show the mean number of pump photons (purple dashed) to illustrate that the Page time occurs when around half of the black hole has evaporated. The one-shot decoupling method was implemented via the Quantum Toolbox in Python (QuTiP) [JNN12; JNN13].

As mentioned above, one advantage of the HR-OPA parallel is its susceptibility to being experimentally tested. Therefore, this thesis aims to experimentally explore the black hole information paradox in connection with the OPA, including the quantum nature of the pump field. In this sense, one possibility to test the theoretical results based on the trilinear Hamiltonian is to measure the properties of the pump in an OPA. Since the von Neumann entropy is experimentally challenging to measure, we can investigate other physical properties of the pump field that are more accessible in practice, like its photon number statistics or its Wigner function. This is exactly what we present in Chapters 4 and 5, respectively. Furthermore, in Chapter 6 we provide an overall discussion about the black hole information paradox and its experimental investigation. In the meantime, we review in Sec. 1.4 the solution to the trilinear Hamiltonian in terms of the expected number of pump, signal and idler photons as a function of the parametric gain and compare these results with the ones predicted by the parametric approximation in Sec. 1.2.

1.4 The trilinear Hamiltonian

In general, the trilinear Hamiltonian in Eq. (1.21) describes many fundamental phenomena in optics and atomic physics, like frequency down- and up-conversion [WB70], coherent Raman and Brillouin scattering [Blo65], the coherent emission of light by N_p two-level atoms [BP70], the coupling between normal modes of motion in trapped ions [Din+17], and the black hole evaporation discussed in this thesis, to mention a few. Table 1.1 summarizes the role played by

TABLE 1.1: Some phenomena described by the trilinear Hamiltonian in Eq. (1.21) with the role played by each bosonic mode.

Bosonic mode	**Frequency down- (up-) conversion**	**Raman and Brillouin scattering**	**Coherent emission by N two-level atoms**	**Trapped ions (degenerate)**	**Hawking radiation**
$\hat{a}$	pump (idler)	incoming photon	upper-atomic level	axial phonon	black hole
$\hat{b}$	signal	scattered phonon	lower-atomic level	radial phonon	Hawking radiation
$\hat{c}$	idler (pump)	scattered photon	emitted photon	radial phonon	in-falling particle

each bosonic mode in these phenomena. Despite its usefulness, the trilinear Hamiltonian has no analytical solution, except for at least a couple of initial conditions that we will present later in this section. Nevertheless, D.F. Walls and R. Barakat proved that the trilinear Hamiltonian can be diagonalized using the basis of number states for each mode [WB70]. Additionally, these authors simplified the representation of this basis so that the trilinear Hamiltonian can be diagonalized without resorting to any approximation. We shall outline their exact solution to the trilinear Hamiltonian in the following.

In the case of frequency down-conversion, and assuming that we start with an arbitrary number N_p and N_s of pump and signal photons, respectively, and vacuum in the idler, i.e. $N_i = 0$, each element of the diagonalization basis has the form

$$|N_p - \nu\rangle_a |N_s + \nu\rangle_b |\nu\rangle_c \equiv |\nu\rangle^{(N_p,N_s)}, \quad \nu = 0, 1, \ldots, N_p. \tag{1.22}$$

Here ν is the number of annihilated pump photons and, at the same time, the number of photons created in the signal and idler modes. Please note that the three modes are characterized by six numbers, three describing their actual state plus the other three defining their initial state. However, by energy conservation arguments and assuming $N_i = 0$, we have reduced this number to only three, N_p, N_s and ν. Also note that $\{|\nu\rangle^{(N_p,N_s)}\}$ is a $N_p + 1$-dimensional basis, instead of a more complicated $N_p \times N_s \times N_i$-dimensional basis.

In the Schrödinger picture, the total quantum state $|\psi(t)\rangle$ describing the three modes at time t can be decomposed in the basis $\{|\nu\rangle^{(N_p,N_s)}\}$ as

$$|\psi(t)\rangle = \sum_{\nu=0}^{N_p} c_\nu(t) |\nu\rangle^{(N_p,N_s)}, \tag{1.23}$$

where we have introduced the probability amplitudes $c_\nu(t)$. By replacing Eq. (1.23) into the time-dependent Schrödinger equation $i\hbar\partial|\psi(t)\rangle/\partial t = \hat{H}|\psi(t)\rangle$, we get the following system of

coupled differential equations for the coefficients $c_\nu(t)$,

$$i\dot{c}_\nu(t) = \kappa[m_{\nu-1}(\theta)c_{\nu-1}(t) + m^*_\nu(\theta)c_{\nu+1}(t)], \tag{1.24}$$

with the quantity $m_\nu(\theta) = e^{i\theta}\left[(N_p-\nu)(N_s+\nu+1)(\nu+1)\right]^{1/2}$. This quantity vanishes for $\nu = N_p$, so that the recurrence relation in Eq. (1.24) terminates and we do not need to introduce an additional truncation. We can anticipate the solution to this system of differential equations by rewriting Eq. (1.24) as

$$\dot{c}_\nu(t) = -i\kappa \sum_{\mu=0}^{N_p} M_{\nu\mu}(\theta)c_\mu(t),$$

with $M_{\nu\mu}(\theta) = m_{\nu-1}(\theta)\delta_{\nu,\mu+1} + m^*_\nu(\theta)\delta_{\nu,\mu-1}$, or in matrix form as

$$\dot{\mathbf{c}}(t) = -i\kappa\mathbf{M}(\theta)\mathbf{c}(t). \tag{1.25}$$

Here, $\mathbf{M}(\theta)$ is a complex Hermitian $(N_p+1)\times(N_p+1)$-dimensional matrix defined as

$$\mathbf{M}(\theta) = \begin{bmatrix} 0 & m^*_0(\theta) & 0 & 0 & & & & & \\ m_0(\theta) & 0 & m^*_1(\theta) & 0 & & & & & \\ 0 & m_1(\theta) & 0 & m^*_2(\theta) & & & & & \\ 0 & 0 & m_2(\theta) & 0 & \cdot & & & & \\ & & & \cdot & \cdot & \cdot & & & \\ & & & & \cdot & \cdot & \cdot & & \\ & & & & & \cdot & \cdot & m^*_{N_P}(\theta) & \\ & & & & & & m_{N_P}(\theta) & 0 & \end{bmatrix}, \tag{1.26}$$

and $\mathbf{c}(t)$ is a N_p+1-dimensional column vector with vector elements $c_\nu(t)$. As seen in Eq. (1.26), matrix $\mathbf{M}(\theta)$ is a band matrix whose nonzero elements are those above and below the main diagonal. The solution to Eq. (1.25) is then

$$\mathbf{c}(t) = \exp\left[-i\mathbf{M}(\theta)\kappa t\right]\mathbf{c}(0), \tag{1.27}$$

or, in component form as

$$c_\nu(t) = \left\{\exp\left[-i\mathbf{M}(\theta)\kappa t\right]\right\}_{\nu 0}, \tag{1.28}$$

where we have used the initial condition $c_\nu(0) = \delta_{\nu 0}$, i.e. $|\psi(0)\rangle = |0\rangle^{(N_p,N_s)}$. To explicitly calculate $\exp[-i\mathbf{M}(\theta)\kappa t]$ we recall that $\mathbf{M}(\theta)$ is a Hermitian matrix, and therefore satisfies

$$\exp(-i\mathbf{M}\kappa t) = \mathbf{V}\exp(-i\mathbf{\Lambda}\kappa t)\mathbf{V}^\dagger,$$

with $\mathbf{V}$ a matrix whose columns are the eigenvectors of $\mathbf{M}$, and $\mathbf{\Lambda}$ a diagonal matrix whose

nonzero elements are the eigenvalues of $\mathbf{M}$, i.e. $\mathbf{M} = \mathbf{V}\mathbf{\Lambda}\mathbf{V}^\dagger$. More importantly, once matrix $\mathbf{M}(\theta)$ is numerically diagonalized, we know the quantum state $|\psi(t)\rangle$ in Eq. (1.23) at all times $t \geq 0$, i.e. we only need to diagonalized matrix $\mathbf{M}(\theta)$ once for each set of initial conditions N_p and N_s. The MATLAB code that we wrote to diagonalize matrix $\mathbf{M}(\theta)$ and obtain the coefficients $c_\nu(t)$ is presented in Appendix B, along with the computation time.

Now, we can access all the quantum features of the modes by means of the probabilitiy amplitudes $c_\nu(t)$. For example, we can calculate the mean number of pump, signal and idler photons at time t as

$$\langle\psi(t)|\hat{a}^\dagger\hat{a}|\psi(t)\rangle = \sum_{n=0}^{N_p} n|c_{N_p-n}(t)|^2, \tag{1.29}$$

$$\langle\psi(t)|\hat{b}^\dagger\hat{b}|\psi(t)\rangle = \sum_{n=N_s}^{N_p+N_s} n|c_{n-N_s}(t)|^2, \tag{1.30}$$

$$\langle\psi(t)|\hat{c}^\dagger\hat{c}|\psi(t)\rangle = \sum_{n=0}^{N_p} n|c_n(t)|^2. \tag{1.31}$$

Figure 1.3 shows the relative mean number of photons for the OPA in the spontaneous case. The particular choice of initial conditions for the signal and idler leads to an equal number of photons in these two modes. Therefore, we also refer to the idler when referring to the signal mode. In Figure 1.3(a), we get a periodic energy transfer between the pump and signal modes for $N_p = 1$, with the turning points in the number of pump and signal photons located at the same parametric gains with respect to each other. This periodic energy transfer can be predicted from the analytical solution to the trilinear Hamiltonian for $N_p = 1$,

$$|\psi(t)\rangle = \cos\Gamma|0\rangle^{(1,0)} - ie^{i\theta}\sin\Gamma|1\rangle^{(1,0)},$$

which leads to

$$\langle\psi(t)|\hat{a}^\dagger\hat{a}|\psi(t)\rangle = \cos^2\Gamma, \tag{1.32}$$

$$\langle\psi(t)|\hat{b}^\dagger\hat{b}|\psi(t)\rangle = \sin^2\Gamma = \langle\psi(t)|\hat{c}^\dagger\hat{c}|\psi(t)\rangle. \tag{1.33}$$

The conditions studied in panel (a) have found experimental evidence, for instance, in trapped ions [Din+17]. As a side note, we found an analytical and periodic solution to the trilinear Hamiltonian for $N_p = 2$, which reads

$$|\psi(t)\rangle = \frac{1}{3}\left[2 + \cos\left(\sqrt{3}\Gamma\right)\right]|0\rangle^{(2,0)} - \frac{ie^{i\theta}}{\sqrt{3}}\sin\left(\sqrt{3}\Gamma\right)|1\rangle^{(2,0)} + \frac{\sqrt{2}e^{2i\theta}}{3}\left[\cos\left(\sqrt{3}\Gamma\right) - 1\right]|2\rangle^{(2,0)},$$

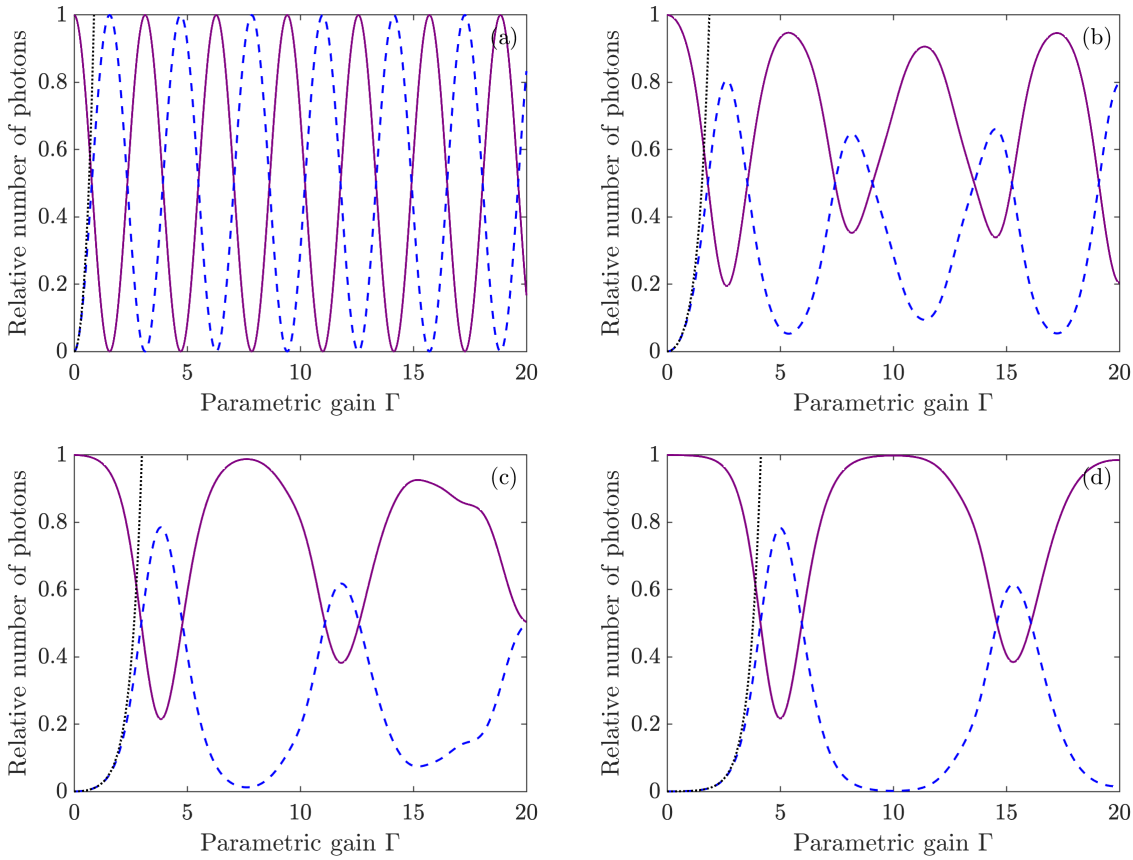

FIGURE 1.3: Mean number of pump (purple solid) and signal (blue dashed) photons resulting from the trilinear Hamiltonian for $N_s = N_i = 0$ and $N_p = 1$ (a), $N_p = 10$ (b), $N_p = 10^2$ (c), and $N_p = 10^3$ (d). In each panel, we also show the number of signal photons (black dotted) under the parametric approximation. The number of idler photons is equal to the number of signal photons.

and yields to

$$\langle\psi(t)|\hat{a}^\dagger\hat{a}|\psi(t)\rangle = \frac{2}{9}\left[2+\cos\left(\sqrt{3}\Gamma\right)\right]^2 + \frac{1}{3}\sin^2\left(\sqrt{3}\Gamma\right), \tag{1.34}$$

$$\langle\psi(t)|\hat{b}^\dagger\hat{b}|\psi(t)\rangle = \frac{1}{3}\sin^2\left(\sqrt{3}\Gamma\right) + \frac{4}{9}\left[\cos\left(\sqrt{3}\Gamma\right)-1\right]^2 = \langle\psi(t)|\hat{c}^\dagger\hat{c}|\psi(t)\rangle. \tag{1.35}$$

There is an analytical solution for $N_p = 3$, but it is no longer periodic. These analytical solutions suggest that there may be analytical results for other N_p values, although none have appeared in the literature, to the best of our knowledge.

Interestingly, the mean number of photons in Eqs. (1.32) through (1.35) are θ independent, which means that we cannot quantify the relative phase between the pump and down-converted fields by detecting their number of photons. This observation also applies to the different initial conditions studied in Fig. 1.3. However, if we redirect the pump, signal and idler fields

towards a second OPA, we observe a modulation in the number of photons that depends on the relative phase between the two OPAs. This configuration is known as a nonlinear interferometer [YMK86], and we will investigate its phase sensitivity in detail in Chapter 3 with the formalism presented in this section.

Coming back to Fig. 1.3, we observe in panel (b) a quasi-periodic energy transfer for $N_p = 10$, with different conversion efficiencies depending on the turning point. We shall investigate the conversion efficiency at the first turning point in Chapter 2 as a tool to compare with the classical predictions for the OPA. Panels (c) and (d), where $N_p = 10^2$ and 10^3, respectively, display maxima and minima with different shapes and varying conversion efficiencies as well. We also observe that the first turning point location shifts to higher parametric gains as N_p increases, or equivalently, the brighter the pump, the lower the quasi-periodic oscillation frequency in the number of photons.

We present in Fig. 1.3 the exact solution to the trilinear Hamiltonian along with the parametric approximation prediction from Sec. 1.2 for comparison. We observe that the exponential growth in Eq. (1.4) closely resembles the exact solution for $\Gamma \lesssim 1$, but for higher gains, the parametric approximation is no longer valid. In particular, the parametric approximation cannot predict the turning points in the number of signal photons because the bilinear Hamiltonian disregards the interplay between the pump and the down-converted modes.

After reviewing the OPA with a quantum pump field employing the trilinear Hamiltonian and illustrating how some authors have exploited its connection with HR in the context of the black hole information paradox, we conclude the present chapter with a general overview of this thesis in Sec. 1.5.

1.5 Outline of this thesis

In Chapter 2 we investigate a classical approach to the OPA based on a similar nonlinear phenomenon, the difference-frequency generation, which holds a classical solution with an evolving pump field. Specifically, we compare the mean number of photons for the OPA predicted by the trilinear Hamiltonian with the ones predicted by the classical OPA model. We find that the classical solution describes fairly well pump depletion, the quasi-periodic energy transfer between the three fields, and the parametric gains for the turning points in the number of photons shown in Fig. 1.3. However, there is an apparent discrepancy in the conversion efficiencies that we analyze in detail. In Chapter 3, we investigate the phase sensitivity of a fully quantum three-mode nonlinear interferometer based on the trilinear Hamiltonian. We show, for example, that such a phase sensitivity exhibits a Heisenberg scaling with the mean number of pump photons [Fl18b]. This result goes beyond the conventionally accepted Heisenberg scaling with the number of down-converted photons inside the interferometer.

In Chapters 4 and 5 we focus on the experimental implementation of the OPA with a dynamical pump field based on parametric down-conversion. In particular, we demonstrate

in Chapter 4 the experimental conditions to observe pump depletion in a simple free-space nonlinear crystal configuration and provide experimental evidence of the interplay between the pump and down-converted fields in terms of the photon number statistics [FLC20]. Furthermore, in Chapter 5 we contrast the experimental Wigner function of the pump field in the presence and absence of pump depletion. Finally, in Chapter 6 we discuss the suitability of the OPA in the context of the black hole information paradox and provide general conclusions on the results presented in this thesis.

In Appendix C we present the design proposals, theoretical models, and experimental demonstration of an optical device unrelated to the main topic of this thesis [Fl18a]. Such a device, which we call variable partially polarizing beam splitter, is an extension of the ubiquitous polarizing beam splitter, with applications in a wide range of very active quantum optics subfields. The other appendices are extensions to some topics in this thesis, as specified in the main text.

Chapter 2

Classical nonlinear interaction of three evolving optical fields

The wave character of light that we discuss in this chapter arises from the classical electromagnetic theory established by J.C. Maxwell in the 19th century. Such a wave character is explicit through a homogeneous wave equation for the optical field in vacuum. In materials, an inhomogeneous wave equation is obtained from Maxwell's equations, where the material response to the optical field acts as a source term. In Sec. 2.1, we review such an optical wave equation in the case where the material response can be decomposed into a linear and nonlinear contribution in the optical field. As we shall discuss later, the nonlinear contribution is responsible for light generation at new frequencies, leading to nonlinear optical phenomena like second harmonic generation, sum- and difference-frequency generation, and third-harmonic generation.

In particular, we focus our attention on the process of difference-frequency generation to provide the most classical approach to the OPA with an evolving pump, i.e. beyond the parametric approximation. We start by obtaining the set of differential equations that couple all the fields involved in difference-frequency generation, including an evolving pump, in Sec. 2.2. Then, we derive in Sec. 2.3 the solution for the field intensities reported by J.A. Armstrong et al. [Arm+62], and compare them side-by-side in Sec. 2.4 with the number of photons predicted by the trilinear Hamiltonian from Chapter 1. Finally, we analyze the similarities and discrepancies between the two approaches and establish the conditions to obtain the OPA number of photons in the spontaneous case from its classical approach.

2.1 The nonlinear optical wave equation

We start with Maxwell's equations describing a frequency component of the optical field in a lossless dielectric material,

$$\nabla \cdot \tilde{\mathbf{D}} = \tilde{\rho},$$

$$\nabla \cdot \tilde{\mathbf{B}} = 0,$$

$$\nabla \times \tilde{\mathbf{E}} = -\frac{\partial \tilde{\mathbf{B}}}{\partial t}, \tag{2.1}$$

$$\nabla \times \tilde{\mathbf{H}} = \frac{\partial \tilde{\mathbf{D}}}{\partial t} + \tilde{\mathbf{J}}, \tag{2.2}$$

with $\tilde{\mathbf{D}} = \epsilon_0 \tilde{\mathbf{E}} + \tilde{\mathbf{P}}$ the macroscopic displacement vector, and $\tilde{\mathbf{P}}$ the material electric polarization due to the optical field. The treatment in this section parallels that of Ref. [Boy08], Sec. 2.1, where a tilde ($\tilde{}$) denotes a field that oscillates at an optical frequency. We consider in this thesis materials with negligible magnetization, thus the magnetic induction is directly proportional to the magnetic field, $\tilde{\mathbf{B}} = \mu_0 \tilde{\mathbf{H}}$. We also consider materials with no free charges nor free currents, i.e. $\tilde{\rho} = 0$ and $\tilde{\mathbf{J}} = 0$.

By taking the curl in Eq. (2.1), switching the temporal and spatial derivatives on the right-hand side, using $\tilde{\mathbf{B}} = \mu_0 \tilde{\mathbf{H}}$ to rewrite the resulting curl of $\tilde{\mathbf{B}}$ in terms of the temporal derivative of $\tilde{\mathbf{D}}$ via Eq. (2.2), replacing $\tilde{\mathbf{D}}$ by $\epsilon_0 \tilde{\mathbf{E}} + \tilde{\mathbf{P}}$, and reordering, we get

$$\nabla \times \nabla \times \tilde{\mathbf{E}} + \epsilon_0 \mu_0 \frac{\partial^2 \tilde{\mathbf{E}}}{\partial t^2} = -\mu_0 \frac{\partial^2 \tilde{\mathbf{P}}}{\partial t^2}. \tag{2.3}$$

On the left-hand side of Eq. (2.3) we have contributions of spatial and temporal second-order derivatives that defines the most general wave equation for the electric field with propagation speed in vacuum $c = 1/\sqrt{\epsilon_0 \mu_0}$, the speed of light. However, we can simplify the spatial derivatives for the purposes of this thesis by using the vector identity

$$\nabla \times \nabla \times \tilde{\mathbf{E}} = \nabla(\nabla \cdot \tilde{\mathbf{E}}) - \nabla^2 \tilde{\mathbf{E}}. \tag{2.4}$$

In the case of an optical field in the form of a transverse, infinite plane wave the divergence of the corresponding electric field is identically zero. Even when the optical field deviates from a plane wave, e.g. when it is a Gaussian beam, the gradient of the electric field divergence is small compared to the electric field Laplacian. Therefore, we neglect the first term on the right-hand side of Eq. (2.4) and rewrite Eq. (2.3) as

$$\nabla^2 \tilde{\mathbf{E}} - \frac{1}{c^2} \frac{\partial^2 \tilde{\mathbf{E}}}{\partial t^2} = \frac{1}{\epsilon_0 c^2} \frac{\partial^2 \tilde{\mathbf{P}}}{\partial t^2}. \tag{2.5}$$

Similar to the power series expansion of the material polarization that led to the trilinear Hamiltonian in Chapter 1, we can decomposed $\tilde{\mathbf{P}}$ into a linear and nonlinear term in the electric field,

$$\tilde{\mathbf{P}} = \tilde{\mathbf{P}}^{(1)} + \tilde{\mathbf{P}}^{(\mathrm{NL})}. \tag{2.6}$$

When replacing this polarization decomposition into the wave equation (2.5), and taking the linear polarization term from the right- to the left-hand side of the equation, we get

$$\nabla^2 \tilde{\mathbf{E}} - \frac{1}{\epsilon_0 c^2} \frac{\partial^2 \tilde{\mathbf{D}}^{(1)}}{\partial t^2} = \frac{1}{\epsilon_0 c^2} \frac{\partial^2 \tilde{\mathbf{P}}^{(\mathrm{NL})}}{\partial t^2}, \tag{2.7}$$

where we have introduced the linear displacement vector $\tilde{\mathbf{D}}^{(1)} = \epsilon_0\tilde{\mathbf{E}} + \tilde{\mathbf{P}}^{(1)}$. In the case of a dispersive material we must write the electric, linear displacement and nonlinear polarization fields in terms of their positive frequency components as

$$\tilde{\mathbf{E}}(\mathbf{r},t) = \sum_n \tilde{\mathbf{E}}_n(\mathbf{r},t), \tag{2.8}$$

$$\tilde{\mathbf{D}}^{(1)}(\mathbf{r},t) = \sum_n \tilde{\mathbf{D}}_n^{(1)}(\mathbf{r},t), \tag{2.9}$$

$$\tilde{\mathbf{P}}^{(\mathrm{NL})}(\mathbf{r},t) = \sum_n \tilde{\mathbf{P}}_n^{(\mathrm{NL})}(\mathbf{r},t), \tag{2.10}$$

where each of these components has the complex form

$$\begin{aligned}
\tilde{\mathbf{E}}_n(\mathbf{r},t) &= \mathbf{E}_n(\mathbf{r})e^{-i\omega_n t} + \text{c.c.},\\
\tilde{\mathbf{D}}_n^{(1)}(\mathbf{r},t) &= \mathbf{D}_n^{(1)}(\mathbf{r})e^{-i\omega_n t} + \text{c.c.},\\
\tilde{\mathbf{P}}_n^{(\mathrm{NL})}(\mathbf{r},t) &= \mathbf{P}_n^{(\mathrm{NL})}(\mathbf{r})e^{-i\omega_n t} + \text{c.c.},
\end{aligned}$$

and n is such that $\omega_n > 0$. Furthermore, the linear displacement and electric field are related by a real, frequency-dependent, dielectric tensor $\boldsymbol{\epsilon}^{(1)}(\omega_n)$,

$$\tilde{\mathbf{D}}_n^{(1)}(\mathbf{r},t) = \epsilon_0\boldsymbol{\epsilon}^{(1)}(\omega_n)\tilde{\mathbf{E}}_n(\mathbf{r},t). \tag{2.11}$$

By replacing Eqs. (2.8) through (2.11) into Eq. (2.7) we get for each frequency component the nonlinear optical wave equation

$$\nabla^2\tilde{\mathbf{E}}_n - \frac{\boldsymbol{\epsilon}^{(1)}(\omega_n)}{c^2}\frac{\partial^2\tilde{\mathbf{E}}_n}{\partial t^2} = \frac{1}{\epsilon_0 c^2}\frac{\partial^2\tilde{\mathbf{P}}_n^{(\mathrm{NL})}}{\partial t^2}. \tag{2.12}$$

Equation (2.12) is an inhomogeneous differential equation where the nonlinear response of the material acts as a source term. More specifically, $\tilde{\mathbf{P}}_n^{(\mathrm{NL})}$ couples the different frequencies involved in a nonlinear optical interaction. For instance, in a second-order process, this term leads to a coupled set of three differential equations for the pump, signal and idler frequencies, respectively. We shall explicitly write and solve this set of differential equations in Sec. 2.2.

2.2 Difference-frequency generation with an evolving pump field

In the classical realm, generating radiation from vacuum is impossible, so we need at least two initial fields interacting in a nonlinear material to generate a third field. Let us assume that the two initial interacting fields have frequencies ω_1 (signal) and ω_3 (pump), and that the generated field has frequency $\omega_2 = \omega_3 - \omega_1$ (idler), with $\omega_3 > \omega_1$. We also assume that the pump and signal fields are collimated, monochromatic, and continuous-wave beams impinging perpendicularly in a lossless second-order nonlinear material and that there is no initial idler

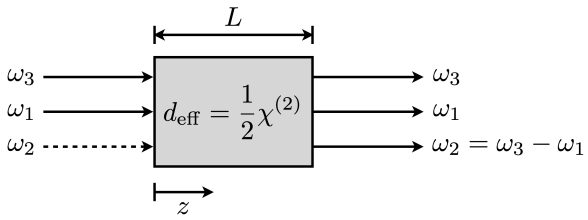

FIGURE 2.1: Schematic of difference-frequency generation. The dashed line for the frequency ω_2 at the material input indicates no initial field at this frequency.

field, as shown in Fig. 2.1. In nonlinear optics, this process is known as difference-frequency generation and is discussed in e.g. Ref. [Boy08] in the case of an undepleted pump field. A more general approach with an evolving pump field can be found in Ref. [Arm+62], which we follow here in order to compare with the trilinear Hamiltonian results for the OPA in Chapter 1.

We suppose that each frequency component of the electric field is linearly polarized and satisfies the wave equation (2.12). In the particular case of the pump field, and for a material with a vanishing nonlinear response, we expect a plane wave propagating in the $+z$ direction at frequency ω_3 with electric field magnitude given by

$$\tilde{E}_3(z,t) = A_3 e^{i(k_3 z - \omega_3 t)} + \text{c.c.} = E_3(z) e^{-i\omega_3 t} + \text{c.c.}, \tag{2.13}$$

where $k_3 = n_3\omega_3/c$ is the the wave number, $n_3 = [\epsilon^{(1)}(\omega_3)]^{1/2}$ is the refractive index, $E_3(z) = A_3 e^{ik_3 z}$ is the pump spatial component, and A_3 is the field amplitude. For a second-order nonlinear material, where the nonlinear source term enters as

$$\tilde{P}_3(z,t) = P_3(z) e^{-i\omega_3 t} + \text{c.c.}, \tag{2.14}$$

we take Eq. (2.13) as a trial solution for the inhomogeneous wave equation (2.12), with A_3 as a function of z. For fixed propagation and polarization directions, it can be shown that the spatial component $P_3(z)$ of the nonlinear polarization reduces to the scalar expression [Boy08]

$$P_3(z) = 4\epsilon_0 d_{\text{eff}} E_1(z) E_2(z), \tag{2.15}$$

with $\chi^{(2)}/2 \equiv d_{\text{eff}}$ the effective second-order electric susceptibility, and $E_1(z) = A_1 e^{ik_1 z}$ and $E_2(z) = A_2 e^{ik_2 z}$ the signal and idler electric field spatial components, respectively. From Eq. (2.15) it is evident that $P_3(z)$ is responsible for the coupling between the pump and the signal and idler fields via the nonlinear material.

We now introduce Eqs. (2.13) through (2.15) into Eq. (2.12) to get a differential equation for A_3 in the form

$$\left[\frac{d^2A_3}{dz^2} + 2ik_3\frac{dA_3}{dz} - k_3^2A_3 + \frac{\epsilon^{(1)}(\omega_3)\omega_3^2}{c^2}A_3\right]e^{i(k_3z-\omega_3t)} + \text{c.c.} \\ = -\frac{4d_{\text{eff}}\omega_3^2}{c^2}A_1A_2e^{i[(k_1+k_2)z-\omega_3t]} + \text{c.c.} \tag{2.16}$$

The third and fourth terms on the left-hand side cancel out to each other because $k_3^2 = n_3^2\omega_3^2/c^2 = \epsilon^{(1)}(\omega_3)\omega_3^2/c^2$. Moreover, if we match the terms proportional to $e^{-i\omega_3t}$ on the left- and right-hand side in Eq. (2.16), we arrive to

$$\frac{d^2A_3}{dz^2} + 2ik_3\frac{dA_3}{dz} = -\frac{4d_{\text{eff}}\omega_3^2}{c^2}A_1A_2e^{-i(k_3-k_1-k_2)z}. \tag{2.17}$$

In practice, the change of A_3 over distances within an optical wavelengths is small because the linear response of the material still dominates over the nonlinear one. Hence,

$$\left|\frac{d^2A_3}{dz^2}\right| \ll \left|2k_3\frac{dA_3}{dz}\right| \ll \left|k_3^2A_3\right|,$$

and the first term on the left-hand side in Eq. (2.17) can be neglected. After applying this approximation, also known as slowly varying amplitude approximation, we arrive at a first-order differential equation for the pump field amplitude,

$$\frac{dA_3}{dz} = \frac{2id_{\text{eff}}\omega_3^2}{k_3c^2}A_1A_2e^{-i\Delta kz}, \tag{2.18}$$

with $\Delta k = k_3 - k_1 - k_2$ the wave-vector mismatch. Following a similar procedure for the signal and idler fields it is possible to show that A_1 and A_2 satisfy similar differential equations,

$$\frac{dA_1}{dz} = \frac{2id_{\text{eff}}\omega_1^2}{k_1c^2}A_3A_2^*e^{i\Delta kz}, \tag{2.19}$$

$$\frac{dA_2}{dz} = \frac{2id_{\text{eff}}\omega_2^2}{k_2c^2}A_3A_1^*e^{i\Delta kz}. \tag{2.20}$$

The coupled set of differential equations for other second order nonlinear optical processes is the same as in Eqs. (2.18) through (2.20), except for the definition of Δk. For example, in sum frequency generation we have $\Delta k = k_1 + k_2 - k_3$, with subscript 3 indicating the resulting field after adding fields 1 and 2, i.e. $\omega_3 = \omega_1 + \omega_2$.

From Eqs. (2.18) through (2.20), which are valid for a lossless material, it is possible to show that the total intensity $I_1 + I_2 + I_3 \equiv I$ is a conserved quantity, i.e. its spatial variation

vanishes, with I_j defined as [Boy08]

$$I_j = 2n_j\epsilon_0 c A_j A_j^* = 2\frac{k_j}{\omega_j}\epsilon_0 c^2 A_j A_j^*. \tag{2.21}$$

To explicitly demostrate this conservation rule, let us take the derivative of Eq. (2.21) with respect to z,

$$\frac{dI_j}{dz} = 2\frac{k_j}{\omega_j}\epsilon_0 c^2 \left(\frac{dA_j}{dz}A_j^* + A_j\frac{dA_j^*}{dz}\right).$$

For $j = 1$, we arrive to

$$\frac{dI_1}{dz} = 4\epsilon_0 d_{\text{eff}}\omega_1 \left(iA_1^* A_3 A_2^* e^{i\Delta kz} + \text{c.c.}\right) = -8\epsilon_0 d_{\text{eff}}\omega_1 \text{Im}\left(A_1^* A_2^* A_3 e^{i\Delta kz}\right). \tag{2.22}$$

Likewise, for $j = 2$ and 3, we have

$$\frac{dI_2}{dz} = -8\epsilon_0 d_{\text{eff}}\omega_2 \text{Im}\left(A_1^* A_2^* A_3 e^{i\Delta kz}\right), \tag{2.23}$$

$$\frac{dI_3}{dz} = -8\epsilon_0 d_{\text{eff}}\omega_3 \text{Im}\left(A_1 A_2 A_3^* e^{-i\Delta kz}\right) = 8\epsilon_0 d_{\text{eff}}\omega_3 \text{Im}\left(A_1^* A_2^* A_3 e^{i\Delta kz}\right). \tag{2.24}$$

When we add Eqs. (2.22) through (2.24), we find that

$$\frac{dI}{dz} = \frac{dI_1}{dz} + \frac{dI_2}{dz} + \frac{dI_3}{dz} = -8\epsilon_0 d_{\text{eff}}\omega_1(\omega_1 + \omega_2 - \omega_3)\text{Im}\left(A_1^* A_2^* A_3 e^{i\Delta kz}\right),$$

which vanishes if $\omega_3 = \omega_1 + \omega_2$, as in sum- and difference-frequency generation. Therefore, the total intensity I is conserved, resulting in one of the Manley-Rowe relations involving the intensities of the three interacting optical fields [MR56]. We can obtain three additional Manley-Rowe relations by looking at terms in the form $d(I_j/\omega_j)/dz$ and noting that

$$\frac{d}{dz}\left(\frac{I_1}{\omega_1}\right) = \frac{d}{dz}\left(\frac{I_2}{\omega_2}\right) = -\frac{d}{dz}\left(\frac{I_3}{\omega_3}\right).$$

The resulting Manley-Rowe relations are then

$$\frac{d}{dz}\left(\frac{I_2}{\omega_2} + \frac{I_3}{\omega_3}\right) = 0, \tag{2.25}$$

$$\frac{d}{dz}\left(\frac{I_1}{\omega_1} + \frac{I_3}{\omega_3}\right) = 0, \tag{2.26}$$

$$\frac{d}{dz}\left(\frac{I_1}{\omega_1} - \frac{I_2}{\omega_2}\right) = 0. \tag{2.27}$$

The intensities I_j have units of energy per unit time per unit area, and when they are divided by ω_j, we can interpret the resulting ratios as the number of photons per unit time per unit area, recalling that the photon energy is proportional to ω_j. In other words, the Manley-Rowe relations (2.25) through (2.27) are nothing else but relations between the number of photons

of the three fields. For example, Eq. (2.26) indicates that the rate at which signal photons are created plus the rate at which pump photons are destroyed, and vice-versa, is a conserved quantity. Equation (2.26) will be particularly useful in Chapter 4, where we find experimental evidence for an evolving pump field in an OPA implemented via parametric down-conversion. Of course, there is no reference to photons in the classical theory of light whatsoever, which makes the Manley-Rowe relations a surprising result because it agrees with the quantum nature of light. A further discussion on this agreement can be found in Ref. [Boy08].

Coming back to the coupled set of differential equations (2.18) through (2.20), we can solve them by rewriting each of the three field amplitudes A_j, $j = 1, 2, 3$, in terms of their magnitudes ρ_j and phases ϕ_j, so that $A_j = \rho_j e^{i\phi_j}$. The resulting set of differential equations can then be split into real,

$$\frac{d\rho_1}{dz} = -K\frac{\omega_1^2}{k_1}\rho_3\rho_2 \sin\vartheta, \tag{2.28}$$

$$\frac{d\rho_2}{dz} = -K\frac{\omega_2^2}{k_2}\rho_3\rho_1 \sin\vartheta, \tag{2.29}$$

$$\frac{d\rho_3}{dz} = K\frac{\omega_3^2}{k_3}\rho_1\rho_2 \sin\vartheta, \tag{2.30}$$

and imaginary parts,

$$\frac{d\phi_1}{dz} = K\frac{\omega_1^2}{k_1}\frac{\rho_3\rho_2}{\rho_1}\cos\vartheta,$$

$$\frac{d\phi_2}{dz} = K\frac{\omega_2^2}{k_2}\frac{\rho_3\rho_1}{\rho_2}\cos\vartheta,$$

$$\frac{d\phi_3}{dz} = K\frac{\omega_3^2}{k_3}\frac{\rho_1\rho_2}{\rho_3}\cos\vartheta,$$

with $K = 2d_{\text{eff}}/c^2$ and $\vartheta = \Delta k z + \phi_3 - \phi_1 - \phi_2$. Using the definition for ϑ, the imaginary parts can be condensed into the single differential equation

$$\frac{d\vartheta}{dz} = \Delta k + K\left(\frac{\omega_3^2}{k_3}\frac{\rho_1\rho_2}{\rho_3} - \frac{\omega_1^2}{k_1}\frac{\rho_3\rho_2}{\rho_1} - \frac{\omega_2^2}{k_2}\frac{\rho_3\rho_1}{\rho_2}\right)\cos\vartheta. \tag{2.31}$$

Now, we express the field magnitudes ρ_j in terms of a new set of real variables u_j and the total intensity I, which is a constant as we showed above,

$$\rho_j = \left(\frac{\omega_j^2 I}{2k_j\epsilon_0 c^2}\right)^{1/2} u_j. \tag{2.32}$$

The variable z can also be written in terms of I and a new independent variable ζ as

$$z = \frac{1}{K}\left(\frac{2k_1k_2k_3\epsilon_0c^2}{\omega_1^2\omega_2^2\omega_3^2 I}\right)^{1/2}\zeta = \frac{(k_1k_2)^{1/2}}{K\omega_1\omega_2\rho_3(0)}\rho_3(0)\left(\frac{2k_3\epsilon_0c^2}{\omega_3^2 I}\right)^{1/2}\zeta = lu_3(0)\zeta, \tag{2.33}$$

where we have defined the interaction length l for the process as

$$l = \frac{(k_1 k_2)^{1/2}}{K\omega_1\omega_2\rho_3(0)}. \tag{2.34}$$

The set of differential equations (2.28) through (2.31) then reduces to

$$\begin{aligned}
\frac{du_1}{d\zeta} &= -u_3 u_2 \sin\vartheta \\
\frac{du_2}{d\zeta} &= -u_3 u_1 \sin\vartheta \\
\frac{du_3}{d\zeta} &= u_1 u_2 \sin\vartheta, \\
\frac{d\vartheta}{d\zeta} &= \frac{\Delta k z}{\zeta} + \cot\vartheta \frac{d}{d\zeta}\ln(u_1 u_2 u_3).
\end{aligned}$$

As mentioned above, the authors in Ref. [Arm+62] provided an analytical solution to this set of differential equations in terms of Jacobi elliptic functions. In the particular case of perfect phase-matching, i.e. $\Delta k = 0$, and recalling that there is no idler field at $z = 0$, i.e. $u_2^2(0) = 0$, the intensities u_j^2 for the three fields associated with difference-frequency generation are

$$u_1^2(\zeta) = u_1^2(0) + u_2^2(\zeta), \tag{2.35}$$

$$u_2^2(\zeta) = u_3^2(0) - u_3^2(\zeta), \tag{2.36}$$

$$u_3^2(\zeta) = u_3^2(0)\mathrm{sn}^2\left[\left(u_3^2(0) + u_1^2(0)\right)^{1/2}(\zeta - \zeta_0), \gamma^2\right], \tag{2.37}$$

with $\mathrm{sn}(u, m)$ the Jacobi elliptic function, the constant ζ_0 defined as

$$\zeta_0 = \frac{F\left(\pi/2, \gamma^2\right)}{[u_3^2(0) + u_1^2(0)]^{1/2}},$$

$F(\phi, m)$ the elliptic integral of the first kind, and

$$\gamma^2 = \frac{u_3^2(0)}{[u_3^2(0) + u_1^2(0)]}$$

the elliptic parameter. This is the most general solution for difference-frequency generation with an evolving pump as long as there is perfect phase-matching and no idler at $z = 0$. It is possible to rewrite Eqs. (2.35) through (2.37) in terms of $\rho_j(z)$, but we postpone it until Sec. 2.3 where we make some approximations to describe the OPA.

By expanding around $\zeta = 0$ the solution for $u_1^2(\zeta)$ and $u_2^2(\zeta)$ in Eqs. (2.35) and (2.36), respectively, and taking the limit $u_1^2(0)/u_3^2(0) \to 0$, the intensity for the signal and idler fields reduces to

$$u_1^2(\zeta) = u_1^2(0)\cosh^2[u_3(0)\zeta], \tag{2.38}$$

$$u_2^2(\zeta) = u_1^2(0)\sinh^2[u_3(0)\zeta]. \tag{2.39}$$

We recover the field intensities ρ_j^2 by using Eqs. (2.32) and (2.33),

$$\rho_1^2(z) = \rho_1^2(0)\cosh^2\left(\frac{z}{l}\right), \tag{2.40}$$

$$\rho_2^2(z) = \frac{n_1\omega_2}{n_2\omega_1}\rho_1^2(0)\sinh^2\left(\frac{z}{l}\right). \tag{2.41}$$

Equations (2.40) and (2.41) are the typical intensities for the signal and idler fields in the process of difference-frequency generation under the parametric approximation, which is valid whenever the nonlinear coupling between the three fields is weak enough to require a bright, and therefore static, pump field. In Sec. 2.3, we use Eqs. (2.35) through (2.37) to provide a classical approach to the OPA based on difference-frequency generation with an evolving pump field.

2.3 Classical optical parametric amplifier

The intensities u_j^2 for the pump, signal and idler fields in Eqs. (2.35) through (2.37) are valid for arbitrary initial conditions in the pump and signal fields, providing no initial idler field. However, the OPA studied in this thesis only has the pump as an input field, which would mean $u_1^2(0) = 0 = u_2^2(0)$. The latter initial condition leads to a vanishing classical solution under the parametric approximation, Eqs. (2.38) and (2.39), and in general to indeterminate values in Eqs. (2.35) through (2.37) because $\gamma^2 = 1$ and $F(\pi/2, 1) \to \infty$. Therefore, we assume that the signal is initially non zero but much weaker than the pump, i.e. $u_3^2(0) \gg u_1^2(0)$. We can assume that the idler is initially non zero instead, but the result would be the same, with subscripts 1 and 2 switched. We can also assume that both signal and idler are non zero and much weaker than the pump. However, this scenario complicates the notation and does not provide further physical insight.

With the initial condition $u_3^2(0) \gg u_1^2(0)$, Eq. (2.37) reduces to

$$u_3^2(\zeta) = u_3^2(0)\mathrm{sn}^2\left[u_3(0)(\zeta - \zeta_0), 1 - \frac{u_1^2(0)}{u_3^2(0)}\right],$$

where we have made the following approximations,

$$\gamma^2 = \frac{u_3^2(0)}{u_3^2(0) + u_1^2(0)} \approx 1 - \frac{u_1^2(0)}{u_3^2(0)},$$

$$\zeta_0 = \frac{F\left(\pi/2, \gamma^2\right)}{[u_3^2(0) + u_1^2(0)]^{1/2}} \approx \frac{1}{u_3(0)}F\left[\frac{\pi}{2}, 1 - \frac{u_1^2(0)}{u_3^2(0)}\right] \approx \frac{1}{2u_3(0)}\ln\left(16\frac{u_3^2(0)}{u_1^2(0)}\right).$$

We return to the intensity ρ_3^2 by using Eqs. (2.32) and (2.33),

$$\rho_3^2(z) = \rho_3^2(0)\mathrm{sn}^2\left[\frac{z-z_0}{l}, 1 - \frac{n_1\omega_3}{n_3\omega_1}\frac{\rho_1^2(0)}{\rho_3^2(0)}\right], \tag{2.42}$$

with

$$z_0 = u_3(0)l\zeta_0 = \frac{l}{2}\ln\left(16\frac{u_3^2(0)}{u_1^2(0)}\right) = \frac{l}{2}\ln\left(16\frac{n_3\omega_1}{n_1\omega_3}\frac{\rho_3^2(0)}{\rho_1^2(0)}\right), \tag{2.43}$$

and l given in Eq. (2.34). For the signal and idler intensities we get

$$\rho_1^2(z) = \rho_1^2(0) + \frac{n_3\omega_1}{n_1\omega_3}\rho_3^2(0)\left\{1 - \mathrm{sn}^2\left[\frac{z-z_0}{l}, 1 - \frac{n_1\omega_3}{n_3\omega_1}\frac{\rho_1^2(0)}{\rho_3^2(0)}\right]\right\}, \tag{2.44}$$

$$\rho_2^2(z) = \frac{n_3\omega_2}{n_2\omega_3}\rho_3^2(0)\left\{1 - \mathrm{sn}^2\left[\frac{z-z_0}{l}, 1 - \frac{n_1\omega_3}{n_3\omega_1}\frac{\rho_1^2(0)}{\rho_3^2(0)}\right]\right\}. \tag{2.45}$$

The solutions for the pump, signal and idler field intensities in Eqs. (2.42), (2.44) and (2.45), respectively, provide a classical description for the OPA beyond the parametric approximation. In particular, the squared Jacobi elliptic function in Eq. (2.42) is a periodic function with a half period equal to z_0/l, which means that the maximum energy transfer from the pump to the signal and idler fields occurs over a distance z_0 in the nonlinear material, with z_0 given in Eq. (2.43) when $\rho_3^2(0) \gg \rho_1^2(0)$. The initial conditions are recovered after a full energy transfer cycle, which occurs at $2z_0$.

It is interesting to note that we find terms of the form $n_j\rho_j^2/\omega_j$ in the expressions for the field intensities. By recalling the definition of I_j in Eq. (2.21), we observe that these terms have the form, up to some constants, of intensity $(2n_j\epsilon_0 c\rho_j^2)$ over photon energy $(\hbar\omega_j)$, as in the Manley-Rowe relations (2.25) through (2.27). Therefore, we can rewrite the solutions for $\rho_j^2(z)$ to give the number of photons per unit area per unit time instead of electric field magnitude squared. We do so in Sec. 2.4 to illustrate the classical solution for the OPA.

2.4 Classical vs quantum optical parametric amplifier

Predictions made by quantum mechanics can look unexpected, counterintuitive and even promising at first sight. However, despite the novelty that quantum mechanics can provide, one must be open to the possibility that some quantum phenomena could be realized with classical systems. To mention one example, ghost imaging, where an object is illuminated by e.g. the signal photons from a parametric down-conversion process while the idlers are detected with spatial resolution, relies on the non-classical correlations between the signal and idler photons. Therefore it was interpreted as a quantum event [Pit+95]. However, later experiments showed that classical correlations are suitable to accomplish ghost imaging as well [Ben+04; Val+05], starting a discussion on the actual scope of quantum mechanics within this phenomenon [SB12; Shi12].

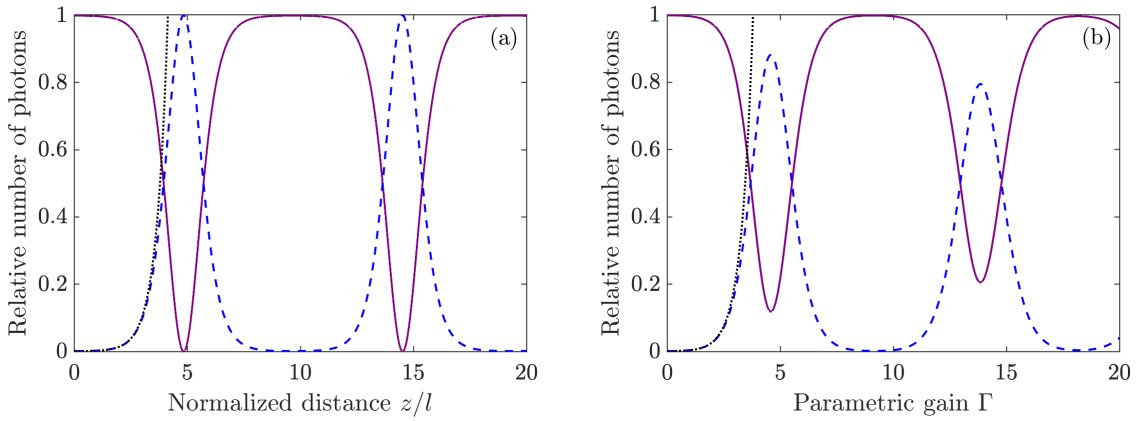

FIGURE 2.2: Classical (a), Eqs. (2.42) and (2.44), vs quantum (b), Eqs. (1.29) and (1.30), number of pump (purple solid) and signal (blue dashed) photons for the optical parametric amplifier with initial conditions $N_p = 10^3$, $N_s = 1$ and $N_i = 0$. We also show the number of signal photons (black dotted) under the parametric approximation in both the classical and quantum models, Eq. (2.40) and (1.5), respectively.

In the specific case of the OPA, we want to investigate the similarities and differences in the photon number predictions made by the classical and quantum models to spot those features that are unique to the quantum realm. For example, in the similar nonlinear optical process of second-harmonic generation, it has been shown that vacuum fluctuations, which have no classical counterpart, play an essential role in the regeneration of the fundamental field [Wal70]. For the OPA, we already pointed out that there is no down-conversion in the spontaneous case according to the classical solution, i.e. when we dismiss the vacuum fluctuations and start with vanishing signal and idler fields. In this section, we will also see that the expected number of photons predicted by both models is similar when the vacuum fluctuations are masked by a large number of initial photons in e.g. the signal field.

We start by comparing the classical field intensities, Eqs. (2.42) and (2.44), with the mean number of photons from the trilinear Hamiltonian, Eqs. (1.29) and (1.30), on an equal basis. To do so, we set the initial conditions $N_p = 10^3$ and $N_s = 1$ on the pump and signal fields, respectively, and vacuum for the idler in both the classical and quantum models. The resulting relative number of photons for the pump and signal fields is presented in Fig. 2.2, while the idler has been omitted for simplicity because it closely follows the signal. As discussed above, we cannot initially set both the signal and idler in vacuum for the following comparison.

The first comment about Fig. 2.2 is the close similarity between the classical and quantum results on the number of photons, including pump depletion, oscillations and the turning point locations. Indeed, it is interesting to note that the independent quantities z/l and Γ have the same qualitative meaning and very similar quantitative values. For example, according to the classical model, the first turning point in the number of photons is located at $z/l = 4.84$,

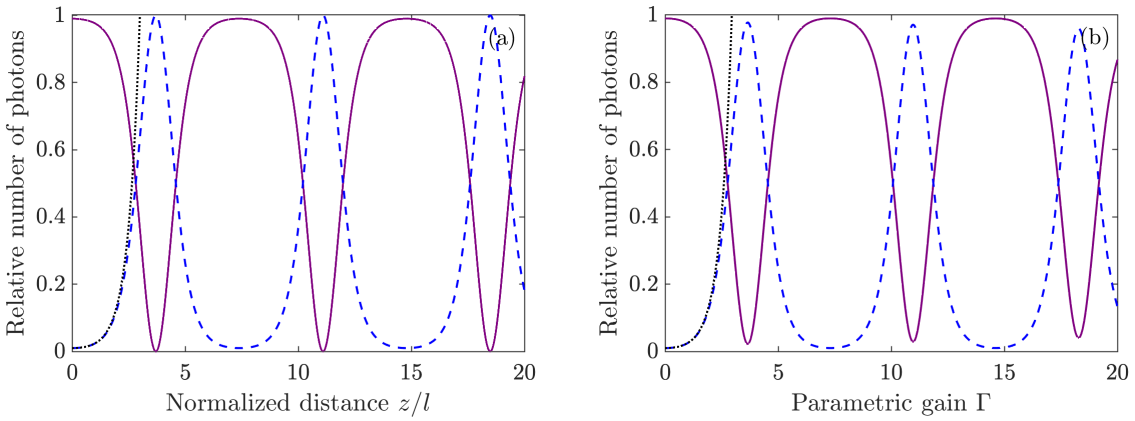

FIGURE 2.3: Classical (a), Eqs. (2.42) and (2.44), vs quantum (b), Eqs. (1.29) and (1.30), number of pump (purple solid) and signal (blue dashed) photons for difference-frequency generation with initial conditions $N_p = 10^3$, $N_s = 10$ and $N_i = 0$. We also show the number of signal photons (black dotted) under the parametric approximation in the classical and quantum models, Eq. (2.40) and (1.5), respectively.

while the quantum model predicts $\Gamma = 4.62$. Another similarity between the two models is the accurate photon number description by their respective parametric approximation solution when $z/l \lesssim 1$ or $\Gamma \lesssim 1$, depending on the model. We can explicitly compare these two parametric approximation solutions for the classical and quantum models, Eq. (2.40) and (1.5), respectively,

$$\rho_1^2(z) = \rho_1(0)^2 \cosh^2\left(\frac{z}{l}\right) \quad \text{vs} \quad \langle \hat{b}^\dagger(t)\hat{b}(t)\rangle = N_s \cosh^2\Gamma + \sinh^2\Gamma.$$

From these expressions, we can observe that the quantum model contains the additional term $\sinh^2\Gamma$ in the number of signal photons, which remains in Eq. (1.5) even in the spontaneous case. Therefore, we conclude that this term in the quantum parametric approximation has no classical counterpart and accounts for the signal field generation from vacuum fluctuations. The same conclusion can be drawn by looking at the parametric approximation solutions for the idler field.

Despite the similarities between the classical and quantum number of photons, as a contribution of this thesis, we find a subtle but meaningful difference in the conversion efficiency from the two models. While in the classical case, shown in Fig. 2.2(a), there is a complete energy transfer from the pump to the down-converted fields and vice versa, the quantum result in panel (b) predicts a maximum conversion efficiency of 88.1% at $\Gamma = 4.62$. Similar conversion efficiency observations have been reported for a degenerate OPA, where less than 2/3 of the pump energy can be transferred to the signal mode in the spontaneous case [DB94]. For the second turning point at $\Gamma = 13.9$, the conversion efficiency is 79.4%. The incomplete energy

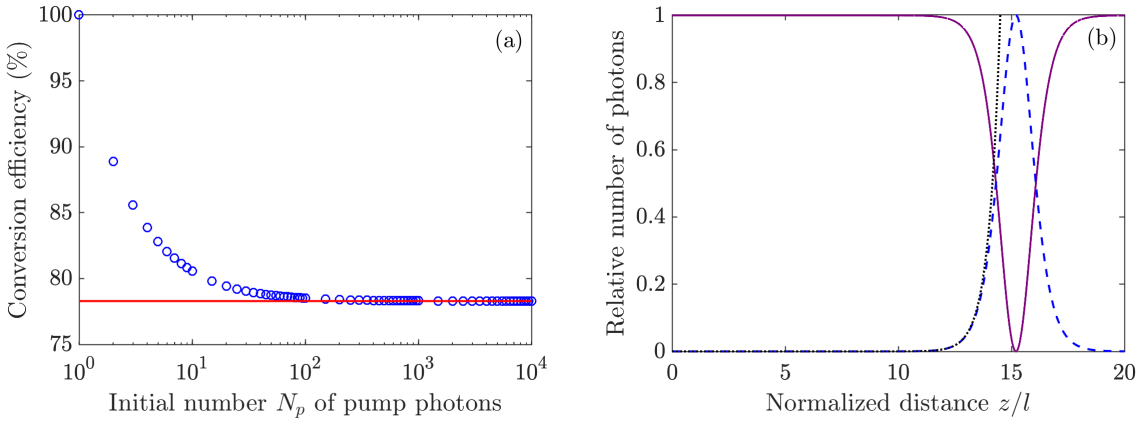

FIGURE 2.4: (a) Conversion efficiency (blue circles) of an optical parametric amplifier at the first turning point in the number of photons according to the quantum model when both signal and idler fields initially vanish. The asymptotic (red solid) line represents a 78.3% conversion efficiency. (b) Classical number of pump (purple solid) and signal (blue dashed) photons, Eqs. (2.42) and (2.44), respectively, in a realistic experimental scenario with $N_p = 10^{12}$, $N_s = 1$ and $N_i = 0$. We also show the number of signal photons (black dotted), Eq. (2.40), under the parametric approximation. The turning point is located at $z/l = 15.2$.

transfer predicted by the quantum model is a consequence of the difficulty to populate the signal and idler modes when their initial number of photons is zero or very small. For example, when the signal and idler are both initially in vacuum, as in Fig. 1.3, the conversion efficiency can be as low as 78.3% at the first turning point, which is lower than the one observed in Fig. 2.2(b). In contrast, if the signal field starts with ten photons, for example, the conversion efficiency can be as high as 97.7%, as depicted in Fig. 2.3 where we observe that the classical and quantum number of photons are very much alike with the initial condition $N_s = 10$. In consequence, the trilinear Hamiltonian predicts high conversion efficiencies, and in general, the same results as the classical model when dealing with an initial number of signal photons $N_s \gg 1$ [BP70].

Another observation for the OPA in the spontaneous case related to the conversion efficiency is that it decreases with the initial number N_p of pump photons, as observed in Fig. 1.3 and further illustrated in Fig. 2.4(a). In particular, there is a 100% pump down-conversion for $N_p = 1$, followed by an asymptotic decrease up to 78.3% as N_p increases. This dependence of the conversion efficiency with N_p is an interesting result for the OPA because no matter how bright the pump field is, the maximum conversion efficiency is 78.3% for $N_p \gg 1$. Moreover, we can combine this conversion efficiency with the classical OPA solution to estimate the number of photons, at least up to the first turning point, in a realistic scenario where $N_p \sim 10^{12}$ and the numerical diagonalization of the trilinear Hamiltonian is intractable in a standard computer. The resulting number of photons for the OPA in the spontaneous case

must look like the classical result in Fig. 2.4(b), where the initial conditions are $N_p = 10^{12}$, $N_s = 1$ and $N_i = 0$, plus a maximum energy transfer from the pump to the down-converted fields extrapolated from panel (a) and equals to 78.3% instead of 100%.

In summary, both the classical and quantum models for the OPA lead to pump depletion and, in general, to oscillations in the number of pump and down-converted photons. These oscillations are not explained by the exponentially-growing parametric approximation results, which only describe the number of signal and idler photons for small normalized distances or parametric gains, depending on the model. For large normalized distances, the classical model predicts periodic oscillations with a complete energy transfer from the pump to the down-converted fields and vice versa. In contrast, for large parametric gains, the quantum model exhibits quasi-periodic oscillations and a fundamental limit in the maximum conversion efficiency, as illustrated in Fig. 1.3 in Chapter 1. Such an energy transfer limitation is pronounced when the signal field is initially in vacuum or with a few photons. However, the classical result approaches the quantum predictions when the vacuum fluctuations are masked by tens of initial photons in the signal field. Finally, we speculate that the classical model accompanied by the asymptotic conversion efficiency of the quantum model could be a satisfactory approximation to the actual quantum photon number dynamics for a large number of initial photons in the pump and initially vanishing signal and idler.

Although the quantum model is the right approach when dealing with the OPA in the spontaneous case, especially if one is interested in e.g. quadrature squeezing and quantum entanglement [DJ92; DJB93; Cas+07], or the von Neumann entropy [NB10] of the pump, signal and idler fields, or any combination of them, the classical OPA provides important physical insight into the interaction of these three evolving optical fields in photon number terms.

Chapter 3

Fully quantum nonlinear interferometer

Optical interferometers have played an essential role in the experimental tests of both the special and general Einstein's theory of relativity. On the one hand, the experimental works by A.A. Michelson and E.W. Morley on the speed of light relative to a hypothetical ether demonstrated that in vacuum, such a speed is the same in all reference frames regardless of the relative motion between the emitting source and the observer. This fact became one of the two pillars in the special theory of relativity formulated by A. Einstein. On the other hand, the same kind of interferometer, the Michelson interferometer, confirmed the existence of gravitational waves [CC16], a phenomenon predicted more than one hundred years ago by the general theory of relativity.

With the development of quantum mechanics in the 20th century, and in particular the advent of quantum optics during the second half of the century, a new type of interferometer made its debut, the nonlinear interferometer [YMK86]. This type of interferometer displays a fundamentally improved phase sensitivity compared to its linear counterparts, like the Michelson or Mach-Zehnder interferometer, as we discuss in Sec. 3.1. As a consequence of the increased sensitivity, a considerable number of nonlinear interferometry applications have been proposed, starting with the detection of gravitational waves with better resolution [Tse+19; Ace+19]. Other applications include infrared spectroscopy with visible light [Kal+16], quantum imaging with undetected photons [BL+14], and spectral engineering of bright squeezed vacuum [Lem+16]. A comprehensive and updated review of nonlinear interferometry and its applications can be found in Refs. [CO16; OL20].

The basis of nonlinear interferometers is a nonlinear optical process, e.g. parametric down-conversion or four-wave mixing, that is usually in a regime where the phase sensitivity can be predicted using the parametric approximation [YMK86]. We refer to this regime as the *low-gain* regime, which is satisfied whenever the parametric gain satisfies $\Gamma < 1$. However, we show in Sec. 3.2 that the resulting sensitivity is overestimated when the nonlinear process is operating in the so-called *high-gain* regime, which takes place whenever $\Gamma > 1$. Hence, we propose in Sec. 3.3 a three-mode nonlinear interferometer based on the trilinear Hamiltonian,

Eq. (1.21), to correctly estimate the phase sensitivity of such an interferometer in both the low- and high-gain regimes, including the quantum nature of the pump field and its resulting dynamics. We present our findings on the phase sensitivity in Sec. 3.4, with an accompanying discussion on the photon number statistics inside the interferometer in Sec. 3.5. The numerical results in this chapter have been reported in Ref. [Fl18b].

3.1 Linear vs nonlinear interferometers

In general, interferometers are phase measurement devices whose sensitivity is in part limited by the quantum fluctuations in the number of output photons. We can calculate the phase sensitivity $\Delta\phi$ from the photon number fluctuation ΔN_{out} via the error propagation formula,

$$\Delta\phi = \frac{\Delta N_{\text{out}}}{|\partial N_{\text{out}}/\partial\phi|_{\phi=\phi_0}}, \tag{3.1}$$

where N_{out} is the output number of photons in the interferometer, $\Delta N_{\text{out}} = \sqrt{\text{Var}(N_{\text{out}})}$, with $\text{Var}(N_{\text{out}})$ the variance of N_{out}, and ϕ_0 is a particular phase where the phase sensitivity is evaluated. Other methods to calculate $\Delta\phi$ include any function of N_{out}, or even the Fisher information, which provides the best sensitivity in a phase estimation problem [Cra46]. However, we use Eq. (3.1) instead because it is the standard method to characterize the interferometer's phase sensitivity [YMK86], and therefore it is convenient for comparison reasons.

In the particular case of the linear interferometer in Fig. 3.1(a), if one of the interferometer inputs is illuminated by a coherent state while the other is in vacuum, the phase sensitivity $\Delta\phi$ is proportional to $N^{-1/2}$, where N is the number of photons that have passed through the interferometer during the detection time. This sensitivity dependence is known as the *shot-noise limit* in photon-counting statistics. In contrast, if non-classical light is used instead of vacuum, like a squeezed state, the phase sensitivity scales now with the inverse number of photons in the interferometer, i.e. $\Delta\phi \sim N^{-1}$ [Cav81]. Such a phase sensitivity is called the *Heisenberg limit*.

Squeezed states of light can be generated by several nonlinear optical processes, including four-wave mixing and parametric down-conversion [Slu+85; Wu+86]. In particular, we reviewed in Chapter 1 the properties of a two-mode squeezed state produced by an OPA. So, the use of active nonlinear media directly in the interferometer paved the way to nonlinear interferometers, like the one shown in Fig. 3.1(b) and that we shall describe below. After incorporating the nonlinear process in the interferometer itself, the resulting phase sensitivity scales with N^{-1}, i.e. the Heisenberg limit is achieved, but with fewer optical elements than linear interferometers [YMK86]. Indeed, sub-shot-noise phase sensitivity has already been demonstrated in optical [Hud+14] and atomic [Lin+16] nonlinear interferometry implementations, even in the presence of internal [XWJ16] and detection [Man+17] losses, which has

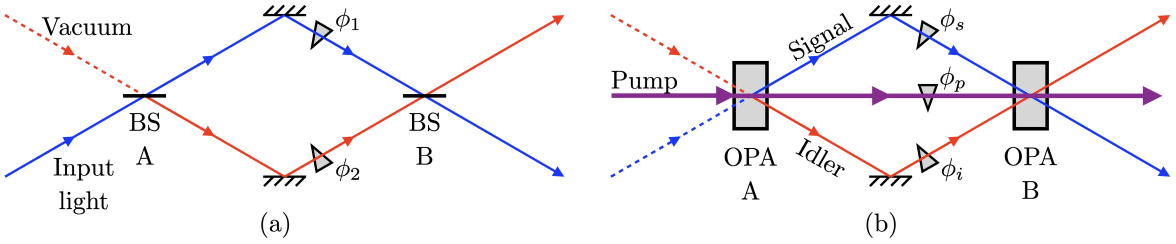

FIGURE 3.1: Linear (a) and nonlinear (b) interferometer in a Mach-Zehnder configuration. BS: beam splitter, OPA: optical parametric amplifier. The dashed lines in both panels represent an input mode in vacuum state.

raised the interest on the field in recent years. Nonlinear interference has even been observed in an integrated silicon photonic chip [Ono+19].

In practice, linear interferometers, like the Mach-Zehnder shown in Fig. 3.1(a), use a beam splitter (BS), labelled BS A in the figure, to divide the incoming light into two beams that travel through independent optical paths. The two beams undergo phase shifts ϕ_1 and ϕ_2, respectively, before overlapping at BS B. The relative phase ϕ between the two paths is then given by $\phi_1 - \phi_2$. If the interferometer is perfectly aligned and the BSs are perfectly balanced, there is no way to tell which path the light in one of the interferometer outputs travelled through, resulting in an interference pattern with perfect visibility. From a mathematical point of view, the overall effect of the BSs and phase shifters on the interferometer two input modes can be characterized by the SU(2) group, which is the reason why linear interferometers are also known as SU(2) interferometers [YMK86]. SU(2) is the group of unitary 2×2 matrices with unit determinants and matrix multiplication as the group operation.

The layout of the nonlinear interferometer shown in Fig. 3.1(b) is very similar to its linear counterpart, but the interference arises differently. In a nonlinear interferometer, the BSs are replaced by nonlinear media where a phase-sensitive nonlinear optical process occurs. If this process is e.g. parametric down-conversion, as illustrated in Fig. 3.1(b), a pump field illuminates OPA A, producing signal and idler photons. These down-converted photons then propagate towards OPA B, undergoing phase shifts ϕ_s and ϕ_i while propagating in their respective paths. The two OPAs must be pumped coherently, so we can use the pump field resulting from OPA A to illuminate OPA B after a phase shift ϕ_p, producing additional signal and idler photons at the interferometer outputs. Then, if the nonlinear interferometer is perfectly aligned and the OPAs properties are the same, it is not possible to tell which of the two OPAs generates the down-converted photons exiting the interferometer, leading to an interference pattern as a function of the relative phase

$$\phi = \phi_p - \phi_s - \phi_i. \tag{3.2}$$

Therefore, the nonlinear interference arises from the indistinguishability between the two places

where the down-converted photons can be generated, as opposed to the indistinguishability between the two optical paths that light can travel through in a linear interferometer.

Although we have limited our discussion to interferometers arranged in a Mach-Zehnder configuration, i.e. with two OPAs one after the other, a similar analysis apply to nonlinear interferometers in Michelson, Sagnac, Young or Fabry-Pérot configurations, as in the linear case. Likewise, a mathematical group, the SU(1,1), characterizes the overall operation of the OPAs and phase shifters on the signal and idler input modes in the parametric approximation. Therefore, nonlinear interferometers are also known as SU(1,1) interferometers. SU(1,1) is the group of complex 2×2 matrices $\mathbf{A}$ with matrix multiplication as the group operation and unit determinant that satisfy the relation $\mathbf{A}^\dagger \mathbf{B} \mathbf{A} = \mathbf{B}$, where [Cor97]

$$\mathbf{B} = \begin{bmatrix} 1 & 0 \\ 0 & -1 \end{bmatrix}.$$

The Bogoliubov transformation in Eq. (1.3) is an example of such a $\mathbf{A}$ matrices. However, it is worth mentioning that the fully quantum nonlinear interferometer that we investigate in this chapter cannot be described by the group SU(1,1) because we are dealing with three modes, the pump, signal and idler, instead of only two, the signal and idler, as it is done everywhere else. Therefore, we refrain from using the term "SU(1,1) interferometer" in our work.

In Sec. 3.2, we explain how the phase sensitivity of a three-mode nonlinear interferometer is overestimated for high parametric gains in the OPAs.

3.2 Overestimation of the phase sensitivity

The nonlinear interferometer described in Sec. 3.1 displays a Heisenberg scaling with respect to the number of photons passing through the interferometer. In the calculation by B. Yurke et al., this number turns out to be the number $N_{\text{in}}^{(\text{PA})}$ of down-converted photons inside the interferometer [YMK86], i.e. produced by OPA A in Fig. 3.1(b),

$$\Delta\phi^{(\text{PA})} = \frac{1}{\left[4N_{\text{in}}^{(\text{PA})}\left(N_{\text{in}}^{(\text{PA})}+1\right)\right]^{1/2}} \sim \frac{1}{N_{\text{in}}^{(\text{PA})}}, \tag{3.3}$$

with $N_{\text{in}}^{(\text{PA})} = \sinh^2\Gamma$ according to Eq. (1.4), $\Gamma = \sqrt{N_p}\kappa t$ the parametric gain of OPA A, and the superscript (PA) indicating that this result has been obtained under the parametric approximation. In other words, the contribution of the pump dynamics has been ignored in Eq. (3.3). However, the pump field resulting from OPA A can also be involved in the interferometer phase sensing via ϕ_p in Eq. (3.2), meaning that it must be taken into account within the number of photons passing through the interferometer. Moreover, the input pump field is the energy source of the interferometer, given that the signal and idler fields start in vacuum. Therefore, for a particular OPA conversion efficiency, it is reasonable to express

the phase sensitivity of a nonlinear interferometer in terms of the pump field, i.e. the initial number N_p of pump photons [GLM11].

We start our contribution to the subject by expressing the phase sensitivity in Eq. (3.3) in terms of N_p. Interferometers where the OPAs are illuminated by two independent pump beams, or where there are non-vanishing signal and idler fields entering the interferometer [PDA10; Li+14], can be considered as well, but we restrict ourselves to the nonlinear interferometer described above as the first case study. In the particular case of $\Gamma \ll 1$, $N_{\text{in}}^{(\text{PA})}$ can be approximated by the lowest term in the Taylor expansion of $\sinh^2\Gamma$ around $\Gamma = 0$, i.e. $\sinh^2\Gamma \approx \Gamma^2 + O(\Gamma^4)$. Thus, $\Delta\phi^{(\text{PA})}$ scales as

$$\Delta\phi^{(\text{PA})} \sim \frac{1}{N_p\kappa^2 t^2} \quad \text{if } \Gamma \ll 1. \tag{3.4}$$

Equation (3.4) is valid in the low-gain regime, and leads to a Heisenberg scaling with respect to N_p. In contrast, when $\Gamma \gg 1$, the number of down-converted photons can be approximated by $\sinh^2\Gamma \approx \exp(2\Gamma)$, which yields to a phase sensitivity that scales as

$$\Delta\phi^{(\text{PA})} \sim \frac{1}{\exp\left(2\sqrt{N_p}\kappa t\right)} \quad \text{if } \Gamma \gg 1. \tag{3.5}$$

This phase sensitivity exceeds the Heisenberg limit, which is the maximum limit allowed by quantum mechanics [Ou96]. Therefore, we need to go beyond the parametric approximation to find the actual $\Delta\phi$ in terms of N_p when the parametric gain increases and avoid the phase sensitivity overestimation in the high-gain regime.

One way to understand why the parametric approximation fails to describe the phase sensitivity in the high-gain regime is by energy conservation arguments. If we look at the number of down-converted photons generated by OPA A, $\sinh^2(\sqrt{N_p}\kappa t)$, we observe that this number grows exponentially with $\sqrt{N_p}$. To put a numerical example, let us assume $\kappa t = 1$ and $N_p = 9$. Then, the number of down-converted photons is $\sinh^2(3) \approx 100$. However, it is impossible to produce 100 signal and idler photon pairs out of 9 pump photons because the pump energy would not be conserved in the down-conversion process, as dictated by the Manley-Rowe relations [MR56]. As discussed in Chapter 2, these relations establish, for example, that the rate at which signal photons are created is equal to the rate at which pump photons are destroyed. In Sec. 3.3, we propose a model based on the trilinear Hamiltonian to correctly estimate the phase sensitivity of a nonlinear interferometer in the high-gain regime, including the quantum nature of the pump field and its evolution.

3.3 Three-mode nonlinear interferometer

The theoretical models for nonlinear interferometers proposed so far approximate the pump as a classical and undepleted field, restricting its contribution to interferometer phase sensing.

Furthermore, these models also overestimate the phase sensitivity when expressed in terms of the initial number of pump photons. Hence, to solve these issues and correctly estimate the phase sensitivity of a nonlinear interferometer in the high-gain regime, we introduce a model in which each of the OPAs in Fig. 3.1(b) interacts with the light fields via the trilinear Hamiltonian in Eq. (1.21). Thus, the pump, signal and idler fields are treated equally, and their corresponding quantum features are fully considered within the interferometer dynamics. We call such an interferometer a fully quantum, or more specifically, a *three-mode* nonlinear interferometer. A related theoretical model was proposed for a nonlinear interferometer based on a four-wave mixing process between atoms in Bose-Einstein condensates [GPS15]. However, our three-wave mixing process and the studied initial conditions and photon number analysis that we accomplish with our model are fundamentally different from those studied by M. Gabrielli et al.

We start by considering the initial state $|\psi(0)\rangle$ for the total system composed by the pump, signal and idler fields at the interferometer entrance. This state corresponds to the tensor product of the pump state $|\chi\rangle_a$ and the signal and idler vacuum states, i.e.

$$|\psi(0)\rangle = |\chi\rangle_a|0\rangle_b|0\rangle_c.$$

We study two cases for $|\chi\rangle_a$, the Fock and coherent state. First, let us consider the Fock state $|N_p\rangle_a$. According to the trilinear Hamiltonian solution by D.F. Walls et al. [WB70], which we summarized in Chapter 1, the total state after OPA A is characterized by the probability amplitudes

$$\mathbf{c}^{(A)}(t) = \exp\left[-i\mathbf{M}(0)\kappa t\right]\mathbf{c}(0), \tag{3.6}$$

where the coupling constant argument θ has been set to zero as the reference phase, and $\mathbf{c}(0)$ is a N_p+1-dimensional column vector whose first entry is one and zero otherwise, as in Eq. (1.27). Likewise, the probability amplitudes for the total state after OPA B reads

$$\mathbf{c}^{(B)}(t) = \exp\left[-i\mathbf{M}(\phi)\kappa t\right]\mathbf{c}^{(A)}(t), \tag{3.7}$$

with ϕ the interferometer relative phase defined in Eq. (3.2). Using Eq. (3.7) we calculate the mean number N_{out} of signal, or idler, photons at the interferometer output as

$$N_{\text{out}} = \sum_{n=0}^{N_p} n|c_n^{(B)}(t)|^2,$$

and the corresponding photon number fluctuation ΔN_{out}. From these two quantities, we obtain the interference patterns and phase sensitivities that we shall describe later.

In Eqs. (3.6) and (3.7) we simplified our notation by taking the same coupling constants κ and interaction times t for both OPAs. An unbalanced scenario can also be considered, especially when dealing with internal and detection losses [Man+17; Gie+17]. However, since

we investigate a lossless nonlinear interferometer, our study would have no advantage in unbalancing these parameters.

The second initial pump state that we consider is the coherent state [GK04]

$$|\alpha\rangle_a = e^{-|\alpha|^2/2} \sum_{n=0}^{\infty} \frac{\alpha^n}{\sqrt{n!}} |n\rangle_a, \tag{3.8}$$

which is critical in our analysis for two reasons. On the one hand, it is the most classical pure quantum state that can probe a nonlinear interferometer, approximately reproducing the effect of a laser beam in a realistic experimental setup. On the other hand, it is ideal for comparing with a linear interferometer illuminated only by a coherent field, where we already know that the phase sensitivity is shot-noise limited. Thus, by having the same input in both types of interferometers, we can investigate the effect of the interferometer itself on the phase sensitivity.

In the case of $|\alpha\rangle_a$, we solve the trilinear Hamiltonian by using the linearity of the Schrödinger equation and solving for each $|n\rangle_a$ in Eq. (3.8) individually [DJ92]. For a specific α we truncate the summation over n up to n' such that

$$\frac{P_{n'+1}}{P_{|\alpha|^2}} < \delta,$$

where P_n is the Poisson distribution [GK04]

$$P_n = |{}_a\langle n|\alpha\rangle_a|^2 = e^{-|\alpha|^2} \frac{|\alpha|^{2n}}{n!}.$$

We pick $\delta = 10^{-5}$ as a balance between numerical accuracy and computational time.

We present in Fig. 3.2 the interference patterns, i.e. N_{out} as a function of the relative phase ϕ, calculated for the two initial pump states discussed above with $N_p = 10$. For the initial coherent state, the mean number of pump photons is given by $|\alpha|^2$, but we shall use the symbol N_p to denote the initial number of pump photons for both the Fock and coherent states to simplify our notation. We also present the accompanying photon number fluctuation ΔN_{out} as a function of ϕ. In each panel of Fig. 3.2, we analyze three parametric gains, $\Gamma = 1.3$, 2.7 and 4.0, that lead to distinctive interference patterns.

In Fig. 3.2 we observe several minima and maxima at different ϕ values, meaning destructive and constructive interference in the number of down-converted photons due to the nonlinear interference. For example, all parametric gains and initial pump states display a vanishing N_{out} at $\phi = \pi$. This complete destructive interference occurs because OPA B reverses the unitary transformation performed by OPA A on $|\psi(0)\rangle$ so that the down-converted fields return to vacuum at the interferometer output. This ϕ value plays an important role in the phase sensitivity that we investigate in Sec. 3.4. Likewise, we have destructive interference at $\phi = 0$ for $\Gamma = 2.7$, and constructive interference for $\Gamma = 1.3$ and 4.0. These features

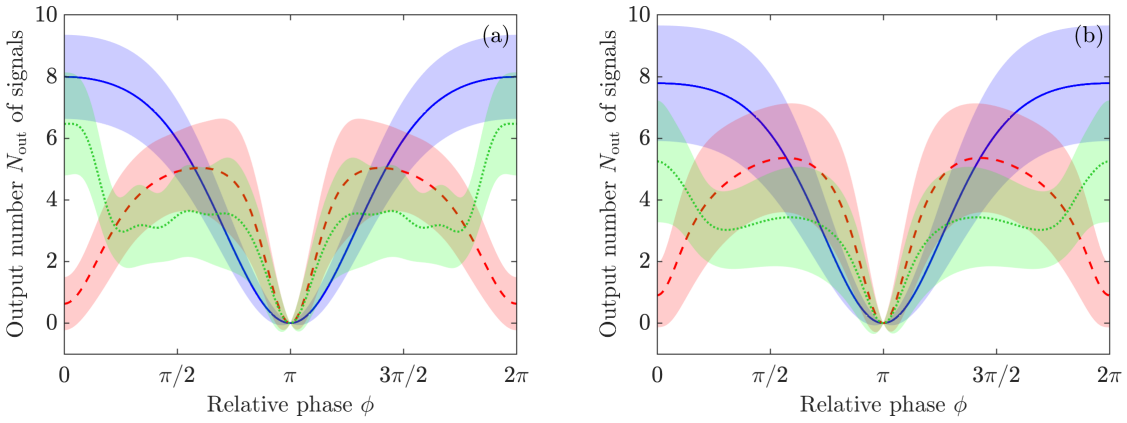

FIGURE 3.2: Interference pattern of a three-mode nonlinear interferometer. The pump field is initially in either a Fock (a) or a coherent (b) state, with $N_p = 10$ initial pump photons, and vacuum for the signal and idler. In each panel, we study three parametric gains, $\Gamma = 1.3$ (solid blue), 2.7 (red dashed), and 4.0 (green dotted). The shadow region for each parametric gain corresponds to the photon number fluctuation ΔN_{out}.

occur because, for twice the mentioned Γ values, we get a minimum and two maxima points, respectively, in the number of signal photons according to Fig. 1.3(b). In other words, the constructive and destructive interference observed in Fig. 3.2 at $\phi = 0$ is a consequence of the two OPAs in the nonlinear interferometer behaving like a single OPA, but with twice parametric gain. Similar analyses can be done for other ϕ values.

Regarding the initial Fock and coherent states for the pump, we observe in Fig. 3.2 that both of them lead to similar interference patterns, with a broader ΔN_{out} in the coherent case due to the non-vanishing photon number fluctuation in the initial pump field. In particular, the photon number fluctuations for a coherent state $|\alpha\rangle$ are given by $|\alpha|$, while for a Fock state, they are identically zero. For the highest parametric gain, $\Gamma = 4.0$, we also observe that N_{out} is smoother around $\phi = \pi/2$ and $3\pi/2$ in panel (b) compared to panel (a). This feature comes from a more stable behaviour in the number of down-converted photons from a single OPA for high parametric gains when the pump is initially in a coherent instead of a Fock state [DJ92].

In Sec. 3.4 we study the phase sensitivity of the nonlinear interferometer in detail for all parametric gains and initial pump states analyzed in Fig. 3.2, and find its optimal value as a function of N_p.

3.4 Phase sensitivity of a three-mode nonlinear interferometer

In Sec. 3.3 we showed that in a three-mode nonlinear interferometer the output number N_{out} of down-converted photons is phase sensitive, i.e. it changes with the relative phase ϕ. This dependence of N_{out} on ϕ can be used in turn to estimate ϕ from N_{out} by inverting the plot

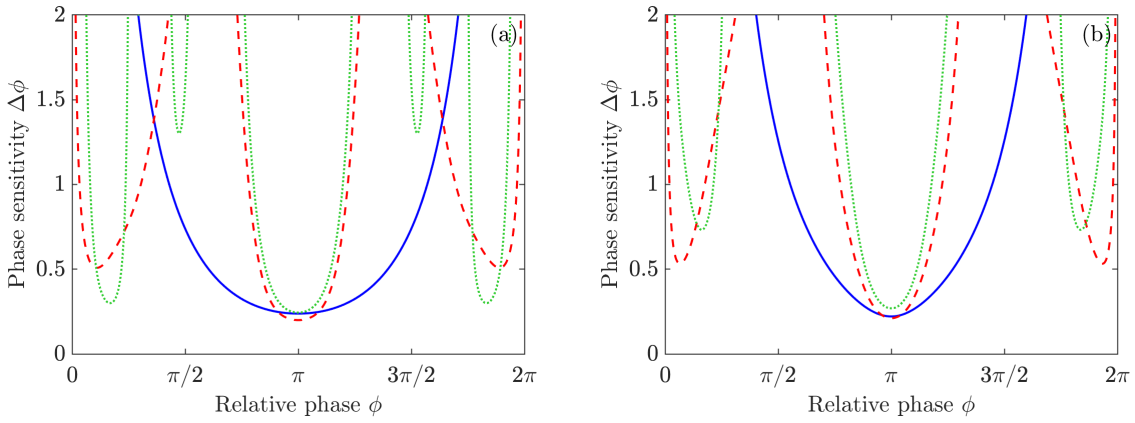

FIGURE 3.3: Phase sensitivity of a three-mode nonlinear interferometer as a function of the relative phase. As in Fig. 3.2, the pump field is initially in either a Fock (a) or a coherent (b) state, with $N_p = 10$ initial pump photons, and vacuum for the signal and idler. In each panel, we study three parametric gains, $\Gamma = 1.3$ (blue solid), 2.7 (red dashed), and 4.0 (green dotted).

axes in Fig. 3.2. Moreover, we can calculate the phase sensitivity $\Delta\phi$ using Eq. (3.1). The resulting $\Delta\phi$ for the cases investigated in Fig. 3.2 is presented in Fig. 3.3 as a function of ϕ.

We observe different points of high phase sensitivity, i.e. low phase uncertainty, in both panels of Fig. 3.3 depending on the parametric gain. For example, for $\Gamma = 1.3$, we get only one of those points, while we observe three or more for $\Gamma = 2.7$ and 4.0. A $\Delta\phi$ extreme point is observed whenever there is destructive interference in the interference patterns of Fig. 3.2. In the case of $\Gamma = 2.7$, for example, we have destructive interference around $\phi = 0$, π and 2π, which are the locations of the $\Delta\phi$ extreme points in Fig. 3.3. However, the best phase sensitivity is achieved at $\phi = \pi$ for any parametric gain or initial pump state considered here. The reason is the low photon number fluctuations exhibited in Fig. 3.2 at complete destructive interference, which leads to a minimum in the ratio of Eq. (3.1). Therefore, we focus our upcoming analysis around this particular relative phase.

In Fig. 3.3 we also observe that $\Delta\phi$ changes with Γ for a fixed relative phase. Hence, we decide to investigate the phase sensitivity as a function of the parametric gain in Fig. 3.4. We consider again two initial pump states, the Fock and coherent states, and two initial numbers of pump photons, $N_p = 10$ and 10^2. Likewise, we cover a wide range of Γ values for $N_p = 10$ that includes both the low- and high-gain regimes, i.e. $\Gamma < 1$ and $\Gamma > 1$, respectively. For $N_p = 10^2$, we only pay attention to the high-gain regime.

In Fig. 3.4, panels (a) and (b), there is an overlap between the phase sensitivities resulting from our three-mode nonlinear interferometer model and the parametric approximation result in Eq. (3.3) for $\Gamma < 1$. This overlap validates our numerical calculations because we build on the already accepted phase sensitivity in the low-gain regime. However, despite the exponentially

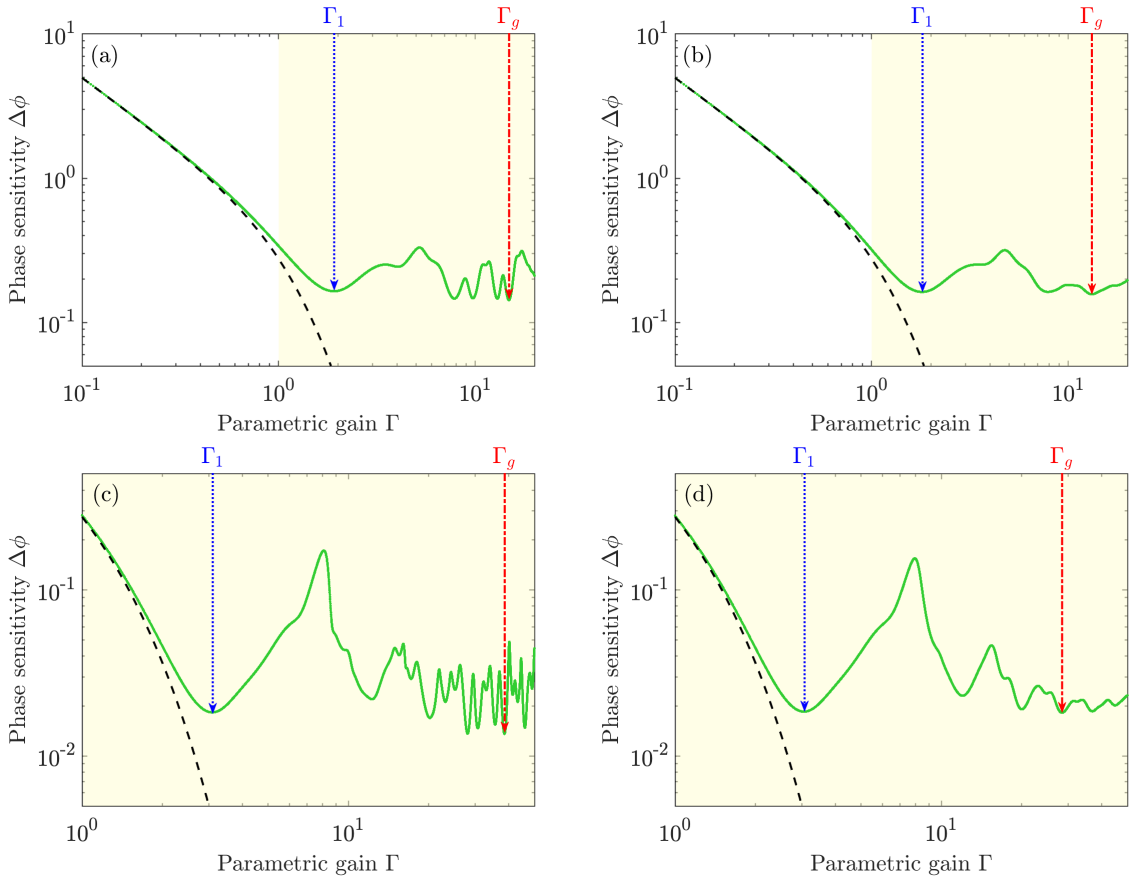

FIGURE 3.4: Phase sensitivity of a three-mode nonlinear interferometer as a function of the parametric gain in the interferometer OPAs. The pump field is initially in either a Fock, panels (a) and (c), or a coherent state, panels (b) and (d). In panels (a) and (b), we have $N_p = 10$, while in (c) and (d), $N_p = 10^2$. In each panel we contrast the results from our nonlinear interferometer model (green solid) with the one from the parametric approximation (black dashed). The locations of the first (blue dotted) and global (red dashed-dotted) optimal phase sensitivities are labeled as Γ_1 and Γ_g, respectively. To distinguish between the low- and high-gain regimes, we shadow (beige) the region defined by $\Gamma > 1$ in all panels.

increasing phase sensitivity in the low-gain regime, $\Delta\phi$ has not taken advantage of the high-gain regime to reach its optimal values. Indeed, in this particular regime, our model predicts a $\Delta\phi$ that oscillates around a saturation level, in contrast to the unphysical exponentially increasing $\Delta\phi^{(\mathrm{PA})}$ discussed in Sec. 3.2 and visualized in all panels of Fig. 3.4.

Within the oscillatory behaviour of $\Delta\phi$ in Fig. 3.4, which is more noticeable for an initial pump field in a Fock compared to a coherent state, we observe several Γ values where the phase sensitivity reaches an optimal point. We identify two of such points, the first and global optimal phase sensitivities, $\Delta\phi_1$ and $\Delta\phi_g$ respectively, and label the corresponding parametric gains as Γ_1 and Γ_g using vertical lines in Fig. 3.4. We then plot these optimal

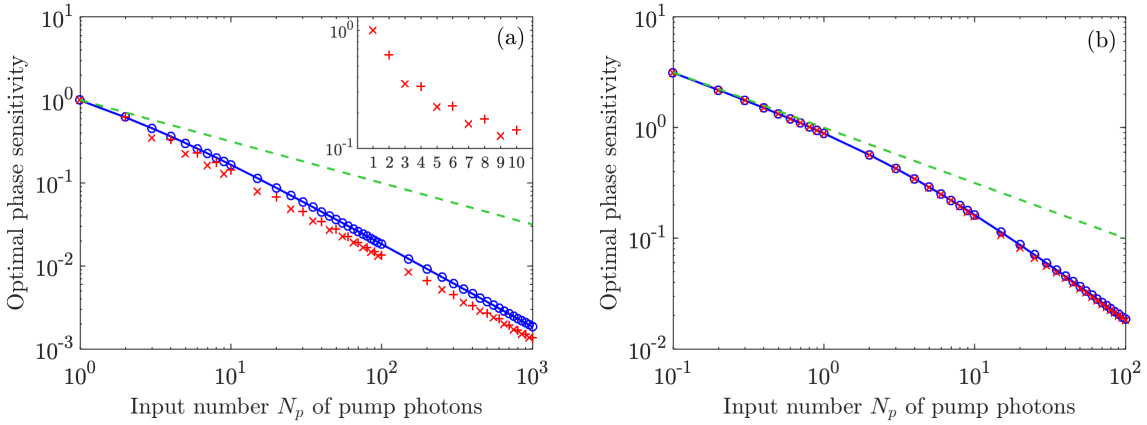

FIGURE 3.5: Optimal phase sensitivities as a function of the initial number of pump photons. The pump field is initially in either a Fock (a) or a coherent (b) state. In each panel, we depict the first (blue circles) and global (red crosses and plus signs) optimal phase sensitivities, $\Delta\phi_1$ and $\Delta\phi_g$ respectively. We also fit $\Delta\phi_1$ to Eq. (3.9) (blue solid), and display the shot-noise limit $N_p^{-1/2}$ (green dashed). Finally, in the inset of panel (a), we zoom $\Delta\phi_g$ for odd (crosses) and even (plus signs) N_p values up to 10.

values as a function of the initial number of pump photons in Fig. 3.5 to finally reveal the actual dependence of $\Delta\phi$ on N_p in the high-gain regime.

The optimal phase sensitivities in Fig. 3.5 are below the shot-noise limit, as expected from a nonlinear interferometer, even in the case when the interferometer is initially illuminated by the most classical pure quantum state, the coherent state in panel (b). Only when N_p approaches unity for the initial Fock state in panel (a), or when $N_p < 1$ for the coherent case in panel (b), the optimal phase sensitivities asymptotically tend to the shot-noise limit. It is worth mentioning that when the pump field is initially in a Fock state, we are restricted to positive integer N_p values, and therefore $N_p \geq 1$, but this is not the case for the coherent case where N_p can take any positive real number. However, values of N_p close to unity are not recommended for phase sensing because they display the poorest phase sensitivities compared to larger numbers of pump photons, as can be seen in Fig. 3.5.

More importantly, $\Delta\phi_1$ displays a Heisenberg scaling with respect to N_p, i.e. it scales as N_p^{-1}. We observe such a Heisenberg scaling in Fig. 3.5 by comparing $\Delta\phi_1$ to an expression analogous to Eq. (3.3), but with N_p instead of the internal number of down-converted photons. The exact expression reads

$$\Delta\phi_1 = \frac{u}{[N_p(N_p+v)]^{1/2}}, \tag{3.9}$$

where u and v are fitting parameters given in Table 3.1. This ad-hoc model provides an accurate description of $\Delta\phi_1$, as seen in Fig. 3.5. Furthermore, this result is in contrast to the super-Heisenberg scaling in the high-gain regime predicted by Eq.(3.5), which is the main

TABLE 3.1: Fitting parameters for the first optimal phase sensitivity in Fig. 3.5 according to Eq. (3.9).

Parameter	**Fock state**	**Coherent state**
u	1.853	1.890
v	2.49	3.53
R^2	0.999997	0.999999

contribution of our work.

In the Fock case, $\Delta\phi_g$ displays slightly better results than $\Delta\phi_1$, although both exhibit a Heisenberg scaling. Moreover, $\Delta\phi_g$ exhibits distinctive values depending on whether N_p is odd or even. We emphasize this feature in the inset of Fig. 3.5(a), where odd numbers of pump photons appear to give better phase sensitivities. We present an explanation for this interesting feature in Sec. 3.5 in terms of the photon number statistics inside the interferometer. In the coherent case, $\Delta\phi_1$ and $\Delta\phi_g$ are almost indistinguishable, which means we reach the optimal phase sensitivity in the nonlinear interferometer by adjusting the parametric gain at Γ_1 in both OPAs.

As a general remark, we demonstrate that the pump-field dynamics cannot be ignored when dealing with a nonlinear interferometer in the high-gain regime, where the phase sensitivity reaches its optimal values allowed by quantum mechanics. Within the factors that may affect the phase sensitivity in this regime are the depletion and quantum features of the pump, like single-mode squeezing [DJB93], and the entanglement between the pump and down-converted fields [Cas+07]. An exciting direction of study would be to investigate a nonlinear interferometer with the classical tools that we presented in Chapter 2. In such a way, one could determine what quantum mechanics actually dictates about the nonlinear interferometer features.

3.5 Photon number statistics inside the interferometer

As we discussed in Sec. 3.1, squeezed states of light can improve the sensitivity of a linear interferometer up to reaching the Heisenberg limit [Cav81]. This sensitivity improvement is an active research field nowadays in the detection of gravitational waves, as reviewed in Ref. [BHS18]. In the case of a nonlinear interferometer, squeezed states are generated by active nonlinear media composing the interferometer, like OPA A in Fig. 3.1(b). Motivated by such non-classical states, we decide to investigate the source of the optimal phase sensitivities that we found in Sec. 3.4. In particular, we look at the photon number probability distribution after OPA A, i.e. the probability distribution $|c_\nu^{(A)}|^2$ from Eq. (3.6), in the simplest case of an initial Fock state for the pump field, and parametric gain equals to Γ_g. This analysis allow us to explain why odd N_p numbers lead to better $\Delta\phi_g$ values in Fig. 3.5(a) than even N_p ones.

First of all, let us recall from Sec. 1.4, Eqs. (1.22) and (1.23), that $c_\nu^{(A)}$ is the probability amplitude of finding the total system in the state $|\nu\rangle^{(N_p,0)} = |N_p - \nu\rangle_a|\nu\rangle_b|\nu\rangle_c$ after OPA A,

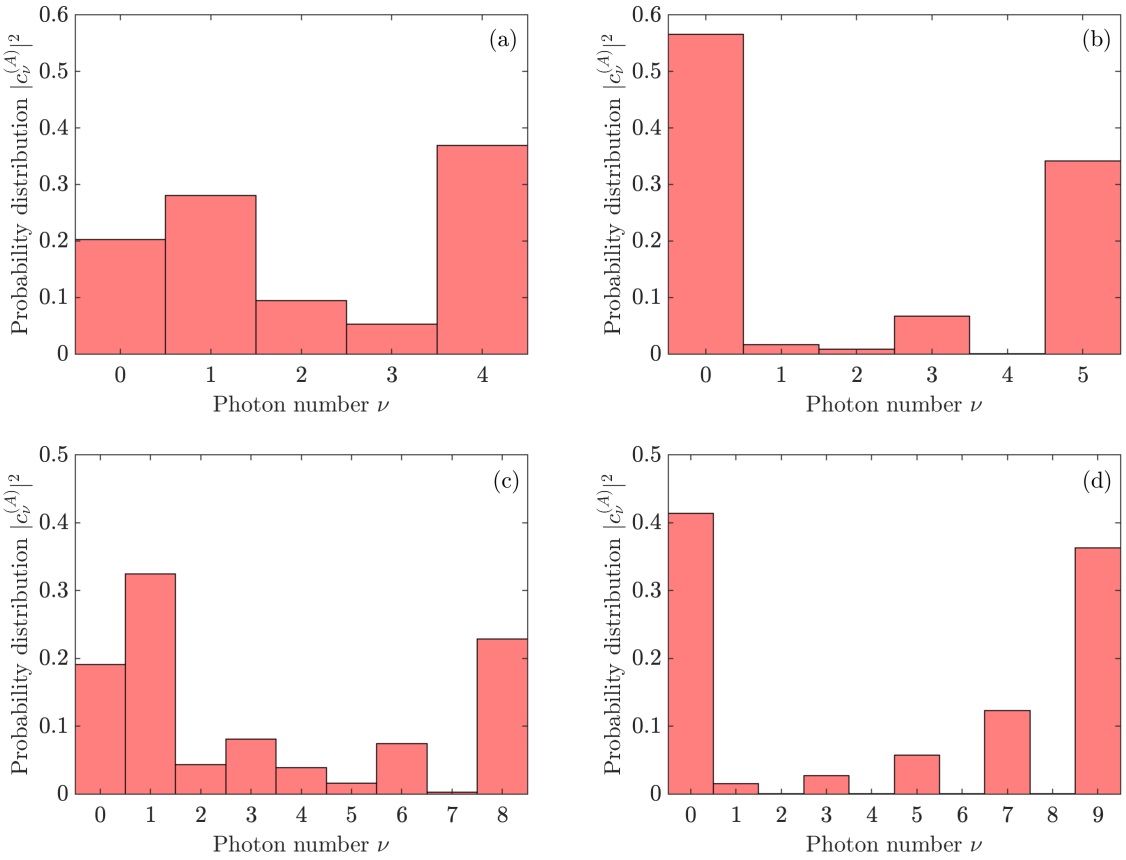

FIGURE 3.6: Photon number probability distribution associated with the quantum state $|\nu\rangle^{(N_p,0)} = |N_p - \nu\rangle_a |\nu\rangle_b |\nu\rangle_c$, $\nu = 0, 1, \ldots, N_p$, after optical parametric amplifier A and parametric gain Γ_g. The initial number N_p of pump photons is 4 (a), 5 (b), 8 (c), and 9 (d), and vacuum for the signal and idler fields.

with $\nu = 0, 1, \ldots, N_p$. For example, $c_0^{(A)}$ is the probability amplitude of finding N_p photons in the pump and vacuum in the signal and idler fields, while $c_{N_P}^{(A)}$ represents the opposite case, i.e. the probability amplitude of finding the pump in vacuum and the signal and idler with N_p photons each. We present in Fig. 3.6 the probability distributions $|c_\nu^{(A)}|^2$ for two different sets of consecutive N_p values, $N_p = 4$ and 5, panels (a) and (b), and $N_p = 8$ and 9, panels (c) and (d), although the photon number features that we shall describe below well apply to any two consecutive N_p values in Fig. 3.5(a).

According to Fig. 3.6, panels (a) and (c), we observe a photon number distribution mainly dominated by three photon numbers, $\nu = 0$, 1 and N_p when N_p is an even number. In contrast, for odd N_p values, panels (b) and (d), the main contributions come only from two photon numbers, $\nu = 0$ and N_p. Since the probability amplitudes in the latter case are associated with the states $|0\rangle^{(N_p,0)}$ and $|N_p\rangle^{(N_p,0)}$, we can approximate the total state after

OPA A by

$$|0\rangle^{(N_p,0)} + |N_p\rangle^{(N_p,0)} = |N_p\rangle_a|0\rangle_b|0\rangle_c + |0\rangle_a|N_p\rangle_b|N_p\rangle_c \quad \text{for odd } N_p. \tag{3.10}$$

The superposition in Eq. (3.10) resembles the so-called N00N state $|N\rangle_{a'}|0\rangle_{b'}+|0\rangle_{a'}|N\rangle_{b'}$, which is a non-classical quantum state where all quanta N appear in either the first or the second mode, a' and b' respectively, of a two-mode quantum entangled state [LKD02]. In our case, these two modes are the pump on the one hand and the down-converted fields on the other. Entangled states are known to reach the Heisenberg limit $\Delta\phi = N^{-1}$ in photonic [Slu+17] and atomic [Mey+01] linear interferometers. Therefore, we attribute the advantage of odd over even N_p values in $\Delta\phi_g$ to the generation of N00N-like quantum states inside the interferometer.

Unfortunately, the photon number distributions inside the interferometer are relatively uniform for a parametric gain equal to Γ_1, so none of the N00N features described above for Γ_g apply to Γ_1. Hence, $\Delta\phi_1$ seems to be of different physical nature. We can look at the amount of single- and two-mode squeezing for the pump and down-converted fields, respectively [DJB93], and the number of down-converted photons inside the interferometer as a function of Γ, but none of the extreme points in these quantities is found precisely at Γ_1. Thus, $\Delta\phi_1$ may come from a combination of squeezing, number of down-converted photons, and even quantum entanglement between the three fields.

If the pump is initially in a coherent state, the previous analysis can be generalized, and it is still possible to observe an N00N-like character in the joint photon number distribution of the pump and down-converted photons inside the interferometer. However, in contrast to the Fock state, the distinction between odd and even N_p is absent since the coherent state is a superposition of Fock states running over all positive integers, and thus the particular features vanish. Indeed, we see that $\Delta\phi_1$ and $\Delta\phi_g$ are almost identical in Fig. 3.5(b), meaning that both optimal values may share the same physical origin.

Chapter 4

Experimental quantum pump field

So far, we have theoretically investigated the OPA using the trilinear Hamiltonian. The resulting pump-field dynamics has been helpful to describe the black hole information paradox in Chapter 1, and the phase sensitivity of a nonlinear interferometer in Chapter 3. In this chapter and Chapter 5, we take a step further in the study of the pump dynamics by experimentally implementing an OPA and observing phenomena like pump depletion and novel photon number properties. Our ultimate goal is to find any feature in either the pump or the down-converted fields that resembles the black hole evaporation described in Chapter 1. If so, we would have experimental evidence to support the HR-OPA parallel and get some insight into the black hole information paradox.

In Sec. 4.1 we present a brief description of parametric down-conversion (PDC), the process used to implement the OPA in the laboratory. We describe our experimental setup in detail in Sec. 4.2 and discuss the measured number of pump and down-converted photons as a function of the input pump energy in Sec. 4.3. In Sec. 4.4, we complement our experimental study of the PDC process by analyzing the photon number statistics in terms of the photon number probability distribution and the second-order correlation function. The experimental results in Secs. 4.3 and 4.4 shine some similarities and discrepancies concerning the black hole evolution that we describe in Sec. 4.5. The experimental results in this chapter have been reported in Ref. [FLC20].

4.1 Parametric down-conversion

Parametric down-conversion is a process where photon pairs, signal and idler, are created due to the interaction of a laser beam, the pump field, with a second-order nonlinear dielectric material. This process, also known as parametric fluorescence in the literature, was first observed by R.L. Byer and S.E. Harris in the late 1960s [HOB67; BH68]. The origin of the term "parametric" is unclear, but in the case of PDC, it may refer to a process in which the initial and final quantum states of the material are identical [Boy08]. The same term, but now in the "parametric approximation", refers to the pump field's vanishing dynamics.

Following the notation in Chapter 2, the optical angular frequencies of the involved fields satisfy the relation $\omega_1 + \omega_2 = \omega_3$, where ω_1, ω_2 and ω_3 are the signal, idler and pump angular frequencies, respectively. When multiplied by $\hbar$, this relation indicates that the energy of a single pump photon is completely transferred to the down-converted photons during the nonlinear process, i.e. the photon energy is preserved as already discussed in connection with the Manley-Rowe relations in Chapter 2. A similar conservation relation is satisfied in terms of the momentum or wave vectors $\mathbf{k}_1$, $\mathbf{k}_2$ and $\mathbf{k}_3$ for the signal, idler and pump fields, respectively, namely $\mathbf{k}_1 + \mathbf{k}_2 = \mathbf{k}_3$. The energy and momentum conservation relations together are known as the phase-matching conditions.

A large number of theoretical and experimental works have been devoted to PDC, mainly because it is a practical way to create an Einstein-Podolski-Rosen state [EPR35], where the correlations between the signal and idler photons are stronger than the ones allowed by classical physics. These non-classical correlations occur in all degrees of freedom of the generated photon pair, including time-frequency, position-momentum, and polarization. The potential applications of such correlations cover a wide range of applications in quantum technologies and theory foundations, as briefly commented in Chapter 1. However, we focus on the high-gain regime, where more than one photon pair can be generated at once in the nonlinear material, and the pump dynamics may play a central role. In this regime, PDC has proven to be a mesoscopic source of polarization-entangled photons [Isk+12a], a platform for sub-shot-noise quantum imaging [BGRB10], and a standard radiation source for instrument calibration [Lem+19], to mention a few applications.

Within high-gain PDC, pump depletion has been a seldom studied phenomenon, with only a few works on the experimental side [All+14; AB14; PJ+16]. Besides the theoretical advantages of having an evolving pump field in the contexts discussed so far in this thesis, the OPA is indeed an example of a tripartite quantum entangled state susceptible of being studied experimentally [Cas+07]. It can even serve as a source of non-classical states of light, like the N00N states described in Chapter 3. Furthermore, the description of multimode high-gain PDC with pump depletion in a fully quantum mechanical fashion remains a theoretical challenge.

An evolving pump field is readily observed in an analogous system to the OPA, known as the optical parametric oscillator [Bos+96]. In this system, the down-conversion process can be enhanced by resonantly coupling the down-converted fields, and sometimes even the pump, to the normal modes of an optical cavity. Depending on the cavity properties, the nonlinear material placed inside, and the pump field, the optical parametric oscillator may become a tunable and commercially available coherent light source. Nevertheless, we observed a dynamic pump field in a more straightforward experimental configuration where the nonlinear material is located in free-space, as described in Sec. 4.2. Interestingly, we shall discuss in Sec. 4.5 that our OPA behaves like an optical parametric oscillator when reaching the high-gain regime with pump depletion, despite the absence of the optical cavity in our setup.

4.2 Experimental setup

To optimize the PDC process and observe a dynamic pump in the simple experimental configuration shown in Fig. 4.1, we followed three steps. First, we pumped the nonlinear material with many photons delivered periodically in short time intervals. We implemented this step via a pulsed laser, a neodymium-doped yttrium aluminium garnet (Nd:YAG) laser (EKSPLA PL2210A-1k), with a 1 kHz repetition rate and 18 ps pulse duration. As we shall see in Sec. 4.3, a photon number equivalent to an energy of 0.1 μJ per pulse is enough to observe pump depletion in our experiment. We used the second harmonic of the Nd:YAG laser, centred at 532 nm and controlled the input pump energy in the nonlinear material using a half-wave plate (HWP) and a linear polarizer, a Glan-Thompson (G-T) prism. We calibrated the HWP by measuring the transmitted light after the G-T prism as a function of the HWP optic axis angle.

The second step to maximize the coupling between the pump, signal and idler fields was to pick a nonlinear material with a pronounced second-order optical nonlinearity. A potential

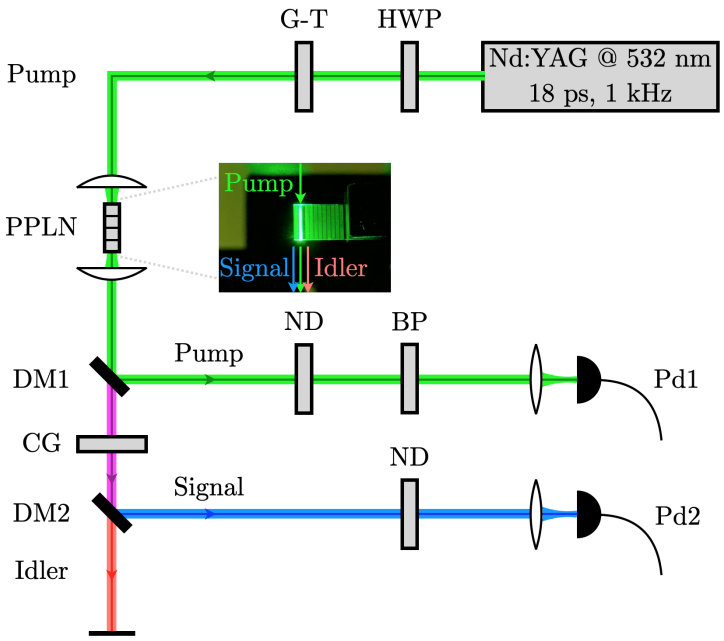

FIGURE 4.1: Experimental setup to observe type-0 high-gain parametric down-conversion with a dynamic pump field. Nd:YAG: neodymium-doped yttrium aluminium garnet (laser), HWP: half-wave plate, G-T: Glan-Thompson (prism), PPLN: periodically-poled lithium niobate (crystal), DM: dichroic mirror, ND: neutral density (filter), BP: band-pass (filter), CG: color glass (filter), Pd: photodetector. Inset: picture of the PPLN crystal, where the vertical stripes correspond to regions in the crystal with different grating periods. As highlighted by the scattered 532 nm laser beam, we illuminated the second region of the crystal, where the grating period is 8.12 μm.

candidate is lithium niobate, a human-made dielectric crystal that is usually 5% MgO doped to avoid optical damage [BGT84]. This crystal has one of the highest second-order nonlinear susceptibilities compared to other commercially available nonlinear materials, like potassium titanyl phosphate (KTP) or β-barium borate (BBO) [RGN03], and therefore is suitable for our purposes. In order to access this high nonlinearity, all the three fields must be extraordinarily polarized, i.e. they must be polarized along the crystal optic axis. This condition on the three fields polarization is known as type-0 phase matching, in contrast to type I or type II where at least one of the down-converted fields is orthogonally polarized to the pump. However, this requirement on the field's polarization is not enough to fulfil the phase matching conditions unless the crystal is periodically poled [Arm+62]. This technique consists in creating domains in the crystal with alternating antiparallel optic axes, as illustrated in Fig. 4.2(a). Thus, depending on the domain length and the pump wavelength, we say that the phase-matching conditions are satisfied in the periodically-poled lithium niobate (PPLN) crystal by *quasi-phase-matching* [Boy08].

The total length of two consecutive domains is defined as the grating period Λ, which ranges from a few to tens of microns for lithium niobate applications in the visible and near/mid infrared regions. Our 8.12 μm grating period, 5 mm length PPLN crystal, manufactured by G&H [G&21], was cut for type-0 phase-matching and designed to operate at room temperature. Using the extraordinary refractive index $n_e(\lambda, T)$ reported by O. Gayer et al. for 5% MgO doped lithium niobate [Gay+08], with λ the wavelength of the extraordinarily polarized field, and T the crystal temperature, we can predict the signal wavelength from the phase-matching condition $\mathbf{k}_1 + \mathbf{k}_2 + \mathbf{K} = \mathbf{k}_3$ as follows. The grating vector $\mathbf{K}$, with magnitude $2\pi/\Lambda$ and oriented perpendicular to the optic axes, accounts for the periodic poling in the lithium niobate crystal [Arm+62]. Assuming perfect phase-matching, and that both the pump and down-converted fields propagate perpendicular to the PPLN optic axes, as shown in Fig. 4.2(a), the component of the wave vector mismatch $\mathbf{k}_1 + \mathbf{k}_2 - \mathbf{k}_3 + \mathbf{K} \equiv \Delta\mathbf{k}$ along the pump propagation direction reads

$$\frac{n_e(\lambda_1, T)}{\lambda_1} + \frac{n_e(\lambda_2, T)}{\lambda_2} - \frac{n_e(\lambda_3, T)}{\lambda_3} + \frac{1}{\Lambda} = 0, \tag{4.1}$$

where we have used $k_j = 2\pi n_e(\lambda_j, T)/\lambda_j$, with $j = 1, 2, 3$. Expressing λ_2 in terms of λ_1 via the condition $\omega_1 + \omega_2 = \omega_3$, and the relation $\omega_j = 2\pi c/\lambda_j$,

$$\lambda_2 = \left(\lambda_3^{-1} - \lambda_1^{-1}\right)^{-1}, \tag{4.2}$$

we numerically solve Eq. (4.1) for λ_1 with $\lambda_3 = 532$ nm and $T = 22.0$ °C. The result is $\lambda_1 = 751$ nm, which yields an idler wavelength $\lambda_2 = 1.83$ μm according to Eq. (4.2). The signal and idler wavelengths as a function of the crystal temperature, also known as tuning curves, are presented in Fig. 4.2(b) for $0\ °\text{C} \leq T \leq 40\ °\text{C}$. These tuning curves suggest that the down-converted wavelengths are more or less constant within the studied temperature range. In Appendix D we investigate the more general scenario of imperfect phase-matching in the

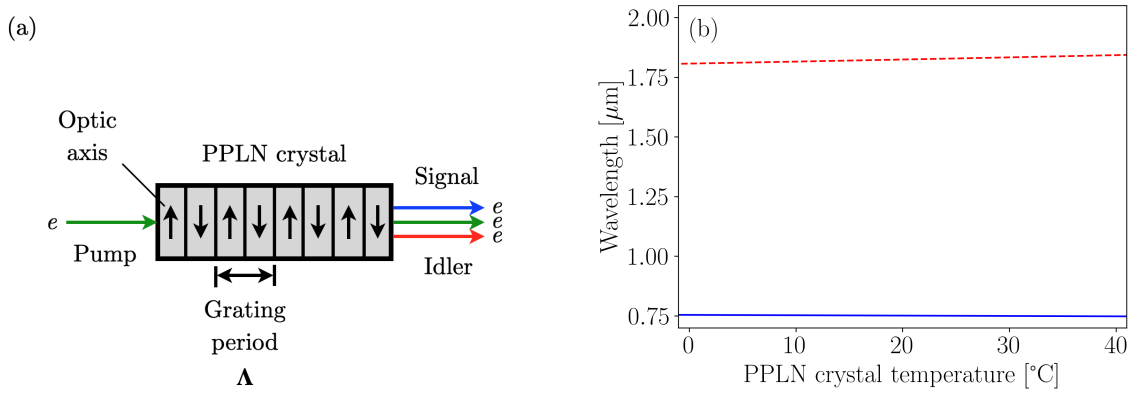

FIGURE 4.2: Periodically-poled lithium niobate crystal (a), and the resulting tuning curves (b) for $\Lambda = 8.12$ μm and pump wavelength $\lambda_3 = 532$ nm. The letter "e" in panel (a) indicates that the corresponding fields are extraordinarily polarized. In panel (b), the signal wavelengths are represented by a (blue) solid line, while the idler ones by a (red) dashed line.

component of $\mathbf{\Delta k}$ parallel to the pump propagation direction. This imperfect phase-matching leads to signal and idler photons emitted in different directions depending on their wavelengths. Nevertheless, most of the down-converted light is produced in the pump propagation direction, also known as the longitudinal or *collinear* direction, with wavelengths λ_1 and λ_2 found via Eqs. (4.1) and (4.2).

The third step to optimize the PDC process in our experimental setup was to increase the pump energy density inside the PPLN crystal. To this end, we focused the pump beam to a waist radius (equivalent to a $1/e^2$ intensity half-width) of 17 μm using a plano-convex lens of 10 cm focal length. After the PPLN crystal, we collimated the pump beam using a similar plano-convex lens, which also serves to collimate the down-converted light. The PPLN crystal was located at the beam waist, fitting within the confocal parameter of the pump beam. Given the tight focusing and the pulsed character of the pump field leading to high intensities, one may be concerned about the crystal's temperature fluctuations. These temperature fluctuations can change the extraordinary refractive index $n_e(\lambda_j, T)$ [Gay+08] and, as a result, the phase-matching conditions of the PDC process. However, a pump repetition rate of 1 kHz for a lithium niobate crystal is low enough to let the material release heat between two consecutive laser pulses [MD04].

Once the PDC process was optimized, we separated the pump from the down-converted fields along their collinear propagation using a dichroic mirror (DM1, EKSMA FS mirror, high reflectivity >99% for p-polarized light at 532 nm, angle of incidence 45°), as shown in Fig. 4.1. After being reflected, the pump beam was attenuated via an absorptive neutral density (ND) filter (Thorlabs NE50A) to avoid detector saturation, further filtered using a band-pass (BP) filter (Thorlabs FL532-10) to remove any leak from the down-converted fields, and finally

focused onto photodetector Pd1. A similar set of optical elements were applied to the signal beam, which was first filtered out from pump leaks using a long-pass coloured glass (CG) filter (Thorlabs FGL570), then separated from the idler beam using a second dichroic mirror (DM2, Semrock FF980), and finally focused onto photodetector Pd2 after an attenuation stage. Given the exponential growth in the number of down-converted photons, we adjusted the attenuation in the signal beam as a function of the input pump energy by choosing from a set of ND filters (Thorlabs NE50A, NE20A, NE10A, NE01A). The idler beam was not measured because we did not have a near-infrared detector available at the experiment.

Regarding the photodetectors Pd1 and Pd2, single-photon detectors typically used in low-gain PDC were not suitable for our purposes due to the large number of pump photons we intended to measure, estimated to be around 10^{11} photons per pulse. Even after attenuating the pump beam five orders of magnitude, we still needed to detect many photons arriving in an 18 ps time interval, equivalent to the pulse duration. Single-photon detectors usually exhibit recovery times on the order of nanoseconds, or hundreds of picoseconds in the best case scenarios to date [Vet+16], and hence did not meet our temporal detection needs. We faced the same challenge when measuring the number of signal photons generated in a similar time interval.

Instead, we used a couple of "homemade" photodetectors inspired by Ref. [Han+01] and further developed in Refs. [ICL09; Man+17] to measure the pump and signal beams. Each photodetector is based on a Si positive-intrinsic-negative photodiode (Hamamatsu S3072), a charge-sensitive preamplifier (Amptek A250) and a couple of pulse shapers (Amptek A275) that transform a detected light pulse into a voltage pulse of a given shape. This photodiode displays the same (up to 0.2%) quantum efficiency (86%) at 532 nm and 750 nm. The area under this voltage pulse is directly proportional to the number of photons in the light pulse, overcoming the issue of detecting a large number of photons in a short time interval. The proportionality constants are $6.65(1) \times 10^{-12}$ and $9.47(3) \times 10^{-12}$ V $\cdot$ s per photon for Pd1 and Pd2, respectively. We include the BP filter at 532 nm in the calibration procedure of Pd1. We used an 8-bit analogue-to-digital converter card (NI USB-5133) to integrate the voltage pulses as a function of time and finally find the number of pump and signal photons per pulse. In Chapter 5, we discuss in more detail this temporal integration for a similar photodetector designed to perform balanced homodyne detection. In Sec. 4.3, we report the measured number of pump and signal photons after averaging 2000 light pulses for each input pump energy considered.

4.3 Mean number of photons

We present in Fig. 4.3 the measured number of pump and signal photons from PDC. We describe the number of signal photons as a function of the input pump power P, although we also provide the energy per pulse when reporting our experimental results for completeness.

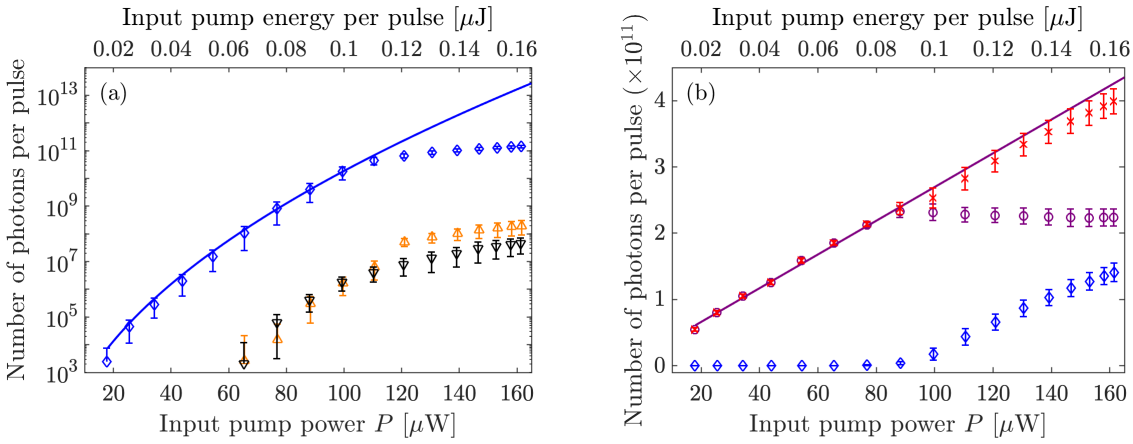

FIGURE 4.3: Experimental number of photons from parametric down-conversion in the high-gain regime with pump depletion. In logarithmic scale (a), we display the number of signal photons (blue diamonds), along with the number of photons from other two second-order nonlinear processes, second-harmonic generation (orange upward-pointing triangles) and sum-frequency generation (black downward-pointing triangles). The (blue solid) line is an exponential model to the number of signal photons for input pump energies up to 0.1 μJ per pulse. In linear scale (b), we display the same number of signal photons as in panel (a), along with the number of pump photons (purple circles) and the sum of these two numbers (red crosses). The (purple solid) line is a linear model to the number of pump photons for input pump energies less than 0.1 μJ per pulse. Both panels show the corresponding input pump power P for comparison reasons. The error bars were multiplied by a factor of 3 for improved visibility.

According to the logarithmic scale in panel (a), this number grows exponentially with P, resembling the parametric approximation result in Eq. (1.4). Such an exponential growth is supported by the close agreement between the experimental data and the exponential model $\propto \sinh^2(b\sqrt{P})$ up to $P \approx 100$ μW $\equiv P'$ (equivalent to 0.1 μJ per pulse), with b a fitting constant. From this constant, we calculate the *gain factor* $G = b\sqrt{P'} = 12.8(2)$, which is a way to quantify the conversion efficiency in PDC [Isk+12b; Cav+16]. However, in contrast to the single-mode theoretical model studied in this thesis, which led to Eq. (1.4), we expect some imperfect phase-matching in our experimental scenario. As mentioned earlier, imperfect phase-matching in the collinear component of $\mathbf{\Delta k}$ allows the generation of down-converted photons in multiple modes or directions depending on their wavelengths, as we discuss in Appendix D. In Sec. 4.4, we quantify the number of modes populated by the down-converted photons using the second-order correlation function. Nevertheless, the exponential growth is still valid in the multimode case, as has been previously observed [Rab+72].

In contrast, the number of signal photons diverges from the exponential model in Fig. 4.3(a) for $P > P'$, meaning that it grows at a different rate. This discrepancy could be a sign of pump depletion, but first, we considered other second-order nonlinear processes that can take

place in the PPLN crystal and would explain this non-exponential growth. One of these processes is second-harmonic generation at 375 nm, originating from the PDC signal field at 750 nm as the fundamental field. Another process is sum-frequency generation at 413 nm due to the pump field at 532 nm plus the idler field at 1840 nm. These processes could reduce the number of detected signal photons by either doubling its frequency or reducing the number of pump photons available for PDC. As shown in Fig. 4.3(a), the resulting number of photons at 375 nm and 413 nm were detected in our experiment starting at $P \approx 60$ μW, but they are three orders of magnitude lower than the number of signal photons. Hence, we regard second-harmonic and sum-frequency generation as parasitic processes that must not affect the number of signal photons. Furthermore, they are not phase-matched, nor are other second-order nonlinear processes that combine the pump, signal or idler fields. Therefore, the non-exponential growth of signal photons for $P > P'$ must have another source.

To get further insight into the PDC process and understand the $P > P'$ regime, we look at the pump field for the same P values in Fig. 4.3(a). As shown in panel (b), the measured number of pump photons also exhibits two distinctive features with respect to P'. On the one hand, this number grows linearly for $P < P'$, as expected from the direct relationship between the field power and the number of photons. Indeed, we obtain a satisfactory agreement when comparing the experimental data with the linear model mP for $P < P'$, where $m = 2.54(7) \times 10^9$ μW^{-1} is a fitting constant. On the other hand, the number of pump photons reaches a plateau for $P \geq P'$, regardless of the increasing number of these photons illuminating the crystal. Moreover, when we plot the number of signal photons again but in the linear scale of Fig. 4.3(b), we have that this number grows linearly starting at the same power P' at which the pump reaches its plateau. This linear growth has also been observed after pumping a similar PPLN crystal at 1064 nm [A.S+20]. We identify these sharp trend changes in the number of pump and signal photons with pump depletion and thus define the regime $P \geq P'$ as the high-gain regime with pump depletion, or simply the *depleted pump regime*.

Given the plateau in the number of photons and the accompanying linear growth of the pump and signal fields, respectively, one may ask if all the initial pump photons are down-converted into signal and idler photon pairs in the depleted pump regime. If this is so, the linear growth rate of the signal field must be the same as the one for the pump before pump depletion. One way to contrast these two rates is by adding the measured number of pump and signal photons, and comparing it with the linear model already discussed for the pump field in the undepleted pump regime, i.e. for $P < P'$. According to the Manley-Rowe relations that we reviewed in Chapter 2, Eq. (2.26) [MR56], the number of pump and signal photons together must be a preserved quantity for a fixed P. We present this photon addition in Fig. 4.3(b) after correcting for some experimental losses for the signal beam, like 9% due to the CG filter, and 8% and 7% due to the ND filters NE10A and NE01A, respectively. The resulting data points closely follow the linear trend of the number of pump photons, suggesting a direct down-conversion of pump photons into signal and idler photon pairs in the depleted

pump regime.

The observed behaviour for the pump and signal fields in Fig. 4.3 has been previously reported by A. Allevi et al. [AB14]. These authors achieved the depleted pump regime via type-I PDC in a BBO crystal with input pump energies per pulse three orders of magnitude higher than those in our experiment. In particular, they observed the transition to the depleted pump regime with an input pump energy of 0.1 mJ per pulse. In contrast, we achieved the same regime with a pump energy as low as 0.1 μJ per pulse by tightly focusing the pump beam into a bulk PPLN crystal. This result refutes the generally accepted idea that pump depletion in a standard PDC process requires very high pump energies. Unfortunately, it is not possible to determine the conversion efficiency in this BBO-based PDC process due to the arbitrary units used by Allevi et al. to report the number of pump photons. In our case, the conversion efficiency at $P = 160$ μW is 33%, which is calculated from the number of signal and pump photons, 1.4×10^{11} and 4.3×10^{11} per pulse, respectively. The latter is obtained by extrapolating the linear behaviour of the number of pump photons into the depleted regime.

In Sec. 4.4 we shall explore the photon number statistics for the pump and signal fields, arriving at different conclusions from those reported by A. Allevi et al. in the depleted pump regime.

4.4 Photon number statistics

To complement our PDC experimental study, we look into the photon number statistics for the pump and signal fields, paying particular attention to any variation in their statistical features during the transition towards the depleted pump regime. Our goal with this study is to look for any quantum signature in the pump field that could experimentally support the HR-OPA parallel, which is the primary purpose of this thesis.

We start by plotting in Fig. 4.4(a) the photon number probability distribution for the pump field at five different input pump powers, two of them in the undepleted pump regime, one during the transition, and two in the depleted regime. The two-photon number distributions in the undepleted regime are located at different photon numbers, where the one associated with the highest input pump power (66 μW) exhibits a larger mean number of photons. This shift is because the number of pump photons depends linearly on the input pump power in this regime, as already seen in Fig. 4.3(b). Qualitatively, these photon number distributions also exhibit a Gaussian shape with narrow widths, which is expected from the coherent nature of the pump field in the undepleted pump regime. This shape is because the Poisson distribution that describes a coherent field has as its limit the Gaussian distribution when the mean number of photons is very large, like in our case. As we increase the input pump powers further, and in particular when we reach the depleted pump regime, the photon number distributions in Fig. 4.4(a) broaden more or less around the same mean number of photons, which corresponds to the plateau in Fig. 4.3(b).

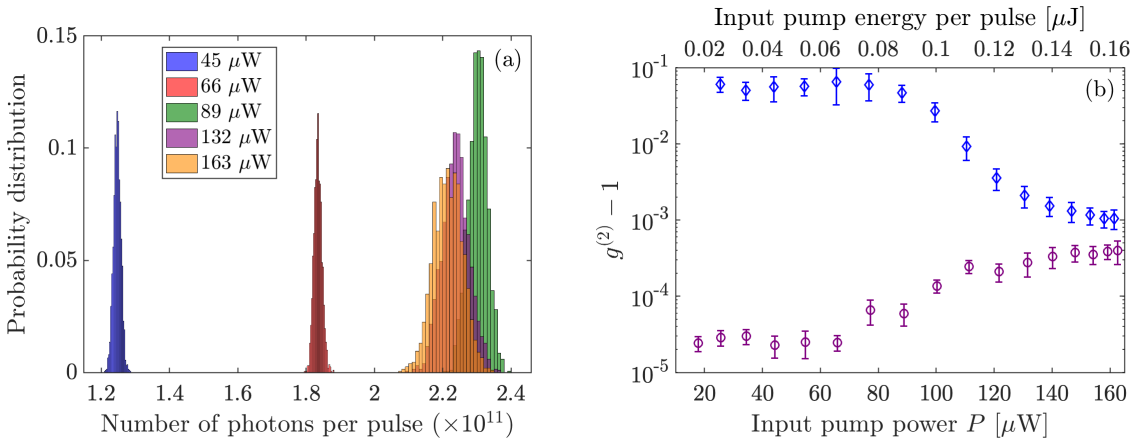

FIGURE 4.4: Photon number probability distribution for the pump field (a), and second-order correlation function at zero time delay for the pump (purple circles) and signal (blue diamonds) fields (b). The error bars were multiplied by a factor of 3 for improved visibility.

To quantitative estimate the widths of the photon number distributions, we calculate the second-order correlation function at zero time delay, $g^{(2)}(0) = \langle : \hat{N}^2 : \rangle / \langle \hat{N} \rangle^2 \equiv g^{(2)}$, also known as the bunching parameter. In this expression, $\hat{N} = \hat{a}^\dagger \hat{a}$ is the photon number operator, and $: \, :$ imposes normal ordering, that is all the annihilation operators $\hat{a}$ are to the right of all the creation operators $\hat{a}^\dagger$ in the product, e.g. $: \hat{N}^2 := (\hat{a}^\dagger)^2 \hat{a}^2$. It is possible to show that $: \hat{N}^2 := \hat{N}^2 - \hat{N}$, leading to the following relation between the photon number variance $\mathrm{Var}(N)$ and $g^{(2)}$ [WM08],

$$\mathrm{Var}(N) = \langle \hat{N} \rangle + [g^{(2)} - 1] \langle \hat{N} \rangle^2. \tag{4.3}$$

In the particular case of a coherent field, $g^{(2)}$ is identically one, which reduces Eq. (4.3) to the characteristic relation $\mathrm{Var}(N) = \langle \hat{N} \rangle$ for a Poisson distribution. This particular result means that the factor $g^{(2)} - 1$ quantifies the divergence of an optical field from a coherent field.

For a large number of photons, as in the pump and signal fields, we can ignore the normal ordering in the definition of $g^{(2)}$ and calculate this quantity as $\langle \hat{N}^2 \rangle / \langle \hat{N} \rangle^2$ from the raw data used in Fig. 4.3(b). We present the resulting $g^{(2)} - 1$ factor for the pump and signal fields in Fig. 4.4(b) as a function of the input pump energy per pulse. In the undepleted pump regime, we observe that $g^{(2)} - 1$ is approximately constant for both the pump and signal fields. In the case of the pump field, we get $g^{(2)} - 1$ of the order of 10^{-5}, which is a small yet nonzero number. In theory, $g^{(2)} - 1$ must identically vanish for light emitted by a laser, like the pump field, but in practice, this nonzero quantity varies from laser to laser. In the case of the signal field, $g^{(2)} - 1$ is almost four orders of magnitude greater than for the pump field due to its thermal nature, as discussed in Chapter 1 concerning the HR-OPA parallel. Indeed, the signal is a multimode thermal field that extends across several spatiotemporal modes [Kly88]. The

number M of these modes can be estimated using the expression [Iva+06]

$$g^{(2)} - 1 = \frac{g_1^{(2)} - 1}{M}, \tag{4.4}$$

with $g_1^{(2)} = 2$ the bunching parameter for single-mode thermal light. From Eq. (4.4), and averaging $g^{(2)} - 1$ for the signal field up to $P = 89$ μW, we obtain $M = 18(2)$.

In contrast to the undepleted pump regime, the $g^{(2)} - 1$ factor displays opposite behaviours for the pump and signal fields in the depleted regime. As seen in Fig. 4.4(b), while $g^{(2)} - 1$ decreases around two orders of magnitude for the signal, it increases around one order of magnitude for the pump, which quantifies the broadening in the photon number distributions observed in Fig. 4.4(a) via Eq. (4.3). These results suggest that the signal gets less chaotic in the depleted regime, approaching the statistics of a coherent field, while the pump diverges from its coherent nature towards a more chaotic field. We attribute these complementary behaviours to an interplay between the pump and down-converted fields, where the coherent nature of the former is imprinted into the latter when the PDC process reaches the depleted pump regime.

Surprisingly, our observations disagree with those made by A. Allevi et al. [AB14], where the pump and signal photon number statistics remains the same when transitioning from the undepleted to the depleted pump regime. The source of this discrepancy may be the detection system used by A. Allevi et al., which successfully describes the photon number distribution of a light field, but in terms of a few numbers of photons [Bon+09]. Since the change in the photon number variance associated with the $g^{(2)} - 1$ factor in Eq. (4.3) is proportional to the mean number of photons, the detectors used by A. Allevi et al. might not be suitable to observe statistical variations in light fields with a large number of photons, as the broadening in the photon number distribution for the pump field in Fig. 4.4(a).

In Sec. 4.5 we review the arguments contained in the previous experimental results that lead to pump depletion. Moreover, we compare our down-converted light source with a laser and an optical parametric oscillator and evaluate the closeness of our experimental results to the trilinear Hamiltonian predictions.

4.5 Comparison with the trilinear Hamiltonian

The sharp turns in the photon number trends in Fig. 4.3, and the associated variations in the photon number statistics in Fig. 4.4, reveal that the parametric approximation fails to describe the pump and signal fields starting at a particular input pump power P'. In particular, the parametric approximation assumes that the pump is unaffected by the PDC process, independently of the input pump power, which is not the case in the depleted pump regime $P \geq P'$. Instead, we observed that the pump field could not generate signal and idler photon pairs at an exponential rate in this regime and even showed a broader photon number distribution.

Interestingly, the pump and signal features that we witnessed in our PDC process resemble those in a laser [Lou00] or an optical parametric oscillator [ED01]. In these optical devices, we get coherent light from an active medium when pumped above a specific power, known as the threshold power. In the laser case, the active medium is a collection of two-level energy emitters that lase via stimulated emission. In contrast, in the optical parametric oscillator case, a difference-frequency generation process takes place in a nonlinear crystal that plays the role of the active medium. Starting at the threshold power, the laser and optical parametric oscillator output light grow linearly with the pump power, and its photon number properties are those of a coherent field. This linear growth is what we observed in Figs. 4.3 and 4.4, where the signal is the output light generated thanks to the pump field, with P' the threshold power. However, unlike our experiment, in the laser and optical parametric oscillator cases, there is an optical cavity coupled to one or more of the involved light fields, enhancing the process for a specific optical mode and making the pump pass through the active medium multiple times. This observation means that our high-gain PDC process with pump depletion can be implemented as a practical source of down-converted light with reduced thermal noise and no optical cavity. This kind of light source may be helpful in quantum imaging [BL+14; Gen16; Boy19] and metrology [SJS17] where thermal noise is a source of additional uncertainties, especially in the high-gain regime.

Apart from the potential applications of our PDC light source, let us discuss whether we witness any quantum feature in the pump field by looking at its photon number statistics. We observed in Fig. 4.4 that the pump field transitions to a more chaotic state as the depleted pump regime is reached. This transition cannot be explained by the classical model for three nonlinear-interacting optical fields that we reviewed in Chapter 2. Furthermore, the pump field deviation from a coherent state resembles the growth in the von Neumann entropy described by K. Brádler et al., and that we reproduced in Fig. 1.2, during the first stage of the black hole evolution [BA16]. However, we did not observe a turning point similar to the one in the von Neumann entropy taking place at the Page time. One reason could be that our conversion efficiency did not reach more than 33%, while the Page time occurs when around 50% of the pump field has depleted, as shown in Fig. 1.2.

Nevertheless, the fact that the signal field experienced precisely the opposite effect, i.e. it transitioned from the thermal state described in Chapter 1 under the parametric approximation to a less chaotic state, is an expected feature during the black evaporation. This fact may suggest that information is encoded in the HR at some point of the black hole evolution to preserve it. Although the photon number statistics reported in this chapter is a naive way to describe the nature of the pump and down-converted fields, and that other figures of merit must be considered when quantifying the amount of information in each of these fields, this is the first attempt to experimental investigate the HR-OPA parallel to the best of our knowledge. In Chapter 5 we take a closer look at the pump field by measuring its Wigner function in both the depleted and undepleted regimes to find more evidence about its quantum nature.

We must recall that the HR-OPA parallel is based on the trilinear Hamiltonian, ideally describing the OPA. In this sense, we observed that the trilinear Hamiltonian does not precisely describe the PDC process implemented in the laboratory. For example, we did not observe up-conversion from the signal and idler photon pairs back into the pump field, as predicted by the trilinear Hamiltonian in e.g. Fig. 1.3. Furthermore, we did not observe either a conversion efficiency greater than 33%, as opposed to the 78.3% discussed in Chapter 2. However, this is not an unexpected result, given that the trilinear Hamiltonian does not take into account wave phenomena like diffraction and group-velocity walk-off. In other words, it oversimplifies the actual PDC process, and therefore more sophisticated models are required. Some semi-classical approaches provide a model for the photon number saturation in the pump field [PJ+16], but the inclusion of the pump quantum nature, a requirement in the HR-OPA parallel, is still elusive.

Chapter 5

Wigner function of the pump field

In Chapter 4 we explored the photon number statistics for the pump and signal fields after an optimized PDC process, which allowed us to draw some conclusions about the HR-OPA parallel. Motivated by the observation of pump depletion in the laboratory, an essential element within the mentioned parallel, we decided to explore the pump field further. Recall that this field plays the role of the black hole. Therefore, any insight about its quantum nature that we can get experimentally will be helpful in our study of the black hole information paradox.

An experimental quantum characterization of the pump field, via its density matrix $\hat{\rho}_a$ for example, would be ideal for determining its quantum features, like the von Neumann entropy or the purity. Thus, we could compare its behaviour with the one expected from the HR-OPA parallel, e.g. in Fig. 1.2. However, measuring $\hat{\rho}_a$ is a challenging task, if not impossible, when the light field contains a macroscopic number of photons, like $N_p \sim 10^{11}$ photons per pulse in our case. The challenge arises from the fact that $\hat{\rho}_a$ contains $N_p^2 \sim 10^{22}$ complex parameters when expressed in the basis of Fock states, which is a practically intractable amount of data. Moreover, we would need photon number resolving detectors that go as high as $N_p \sim 10^{11}$ to determine all the matrix elements of $\hat{\rho}_a$ [BW96; Sri+14]. Therefore, any full quantum characterization of the pump field is impossible for us.

Nevertheless, we attempt to describe the pump field in this chapter using a quantity that is formally equivalent to the density matrix, the Wigner function [Wig32]. In Sec. 5.1 we describe this function and the phase space, where it is defined. The Wigner function has been successfully used to characterize any light field at the single-photon level [Lei+96; BSM97; Lvo+01; Ber+02]. However, to the best of our knowledge, it has not been used to describe bright fields, like the pump after a PDC process. Therefore, the main challenge for us is to sample a bright pump field properly, in contrast to the weak fields commonly studied in similar experimental configurations [Smi+93a; Han+01; Zav+02]. Our strategy is to attenuate the pump field strongly, and examine the capabilities of our experimental setup and measurement strategy, which we introduce in Secs. 5.2 and 5.3, respectively, to describe the Wigner function of such a field. Next, we present our experimental results in Sec. 5.4 and summarize our findings of the pump field based on its Wigner function in Sec. 5.5.

5.1 The Wigner function

The state of a classical system, like a mass suspended by a spring, is described at a given time by a single point in phase space, which is spanned by the mass's position and momentum variables. In contrast, the uncertainty principle stops quantum systems from exhibiting a point-like representation in phase space, so they must be described by a real-valued distribution instead. One of these distributions is the Wigner function, introduced by E.P. Wigner in the early days of quantum mechanics as an auxiliary function to facilitate calculations in a classical fashion [Wig32]. For an arbitrary quantum state described by the density matrix $\hat{\rho}$, the Wigner function is defined as

$$W(q,p) = \frac{1}{2\pi\hbar}\int_{-\infty}^{\infty} \langle q + x/2|\hat{\rho}|q - x/2\rangle e^{ipx/\hbar} dx,$$

where q and p are the eigenvalues of the position and momentum operators, respectively, and $|q \pm x/2\rangle$ is an eigenstate of the position operator. It is possible to show that integrating $W(q,p)$ over p leads to the probability distribution for the eigenvalues q [GK04]. Likewise, integrating $W(q,p)$ over q yields to the probability distribution for p. The probability distributions for q and p obtained by integrating their corresponding conjugate variable are examples of marginal distributions of the Wigner function.

As an example, the resulting Wigner function of an energy eigenstate of the quantum harmonic oscillator, also known as Fock state, looks like water ripples after dropping a stone, with positive and negative values at the peaks and troughs of the waves, respectively, and the number of ripples depending on the particular eigenstate [Sch01]. For the first excited Fock state, the Wigner function has been experimentally reconstructed [Lei+96; Lvo+01; Ber+02]. For higher Fock states [FSSMF01; OTBG06], and other related quantum states, the Wigner function has been reconstructed as well [LM02; LB02; Eic+11; Sha+13].

The possibility of displaying negative values prevents the Wigner function from being a probability distribution because negative probabilities have no meaning from a classical point of view. In turn, these potential negativities are associated with the quantumness of the system. However, there are quantum states whose Wigner function is always nonnegative, like coherent and squeezed states. In particular, the Wigner function of any pure state whose wavefunction is the exponential of a quadratic polynomial is always nonnegative, according to Hudson's theorem [Hud74; SC83]. Despite its potential negativity, the Wigner function successfully predicts the quantum mechanical marginal distributions along any axis in phase space [Wig32], like q and p, which leads to the term *quasiprobability* distribution when referring to the Wigner function. As we shall explain in Sec. 5.2, this property plays a key role when reconstructing the Wigner function from a set of marginal distributions that we measure in the laboratory.

There are other quasiprobability distributions formally equivalent to the Wigner function, like the Glauber-Sudarshan P [Gla63; Sud63] and the Husimi Q function [Hus40], but none

of them is strictly a probability distribution either. For example, the Q function is always nonnegative, but it does not yield the correct marginal distributions in contrast to the Wigner function. A comprehensive summary of quantum phase-space distributions and their properties is presented in Ref. [Lee95]. Hence, the choice of one quasiprobability or the other is a matter of convenience when evaluating particular operators' expectation values. For instance, if we are dealing with normally-ordered operators, like $:\hat{N}^2:$ from Chapter 4, the most convenient choice to calculate its expected value is the P function, but for anti-normally-ordered operators, i.e. those with all the annihilation operators to the left of all the creation operators in the product, the best choice is the Q-function.

The Wigner function has proven to be useful in many physics subfields, like statistical physics [Moy49], scattering theory [İ+67], nonlinear physics [Ber77], and classical optics [Bas79]. It has also been widely used for signal analysis of electrical signals, mechanical vibrations, and sound waves. In quantum optics, our field of interest, we use the Wigner function to represent quantum states of light [Sch01]. For a single-mode light field, the phase space is spanned by the eigenvalues X_1 and X_2 of the conjugate quadratures $\hat{X}_1$ and $\hat{X}_2$, respectively, defined as [GK04]

$$\hat{X}_1 = \frac{1}{2}(\hat{a} + \hat{a}^\dagger), \quad \hat{X}_2 = \frac{1}{2i}(\hat{a} - \hat{a}^\dagger),$$

with the commutation relation $[\hat{X}_1, \hat{X}_2] = i/2$. Some authors prefer to express $\hat{X}_1$ and $\hat{X}_2$ in terms of a coherent state representation,

$$\langle\beta|\hat{X}_1|\beta\rangle = \mathrm{Re}(\beta), \quad \langle\beta|\hat{X}_2|\beta\rangle = \mathrm{Im}(\beta),$$

where $|\beta\rangle$ is a coherent state. If this is the case, the phase space is spanned by the real and imaginary components of β, i.e. the phase space is the complex β-plane. Other authors prefer to name the phase-space axes as $q = \sqrt{2\hbar/\omega}X_1$ and $p = \sqrt{2\hbar\omega}X_2$ in relation to the position and momentum variables of a quantum harmonic oscillator of frequency ω, respectively. However, it is worth to mention that these concepts refer to the single-mode field quadratures in quantum optics, and not to the position and momentum of e.g. a single photon. More specifically, one can think of $\hat{q}$ and $\hat{p}$ as the electric and magnetic field operators at a specific point in the propagation direction of the single-mode field [GK04].

In the context of this thesis, we plan to represent the pump field of our PDC process in phase space. Under ideal circumstances, and in the absence of pump depletion, we can model the pump field as a coherent state $|\alpha\rangle$, as we did in Chapter 3 and explicitly defined in Eq. (3.8) when studying the phase sensitivity of a nonlinear interferometer. The Wigner function of this state reads [GK04]

$$W_{|\alpha\rangle}(X_1, X_2) = \frac{2}{\pi}\exp\left[-2\left(X_1 - \mathrm{Re}(\alpha)\right)^2 - 2\left(X_2 - \mathrm{Im}(\alpha)\right)^2\right]. \tag{5.1}$$

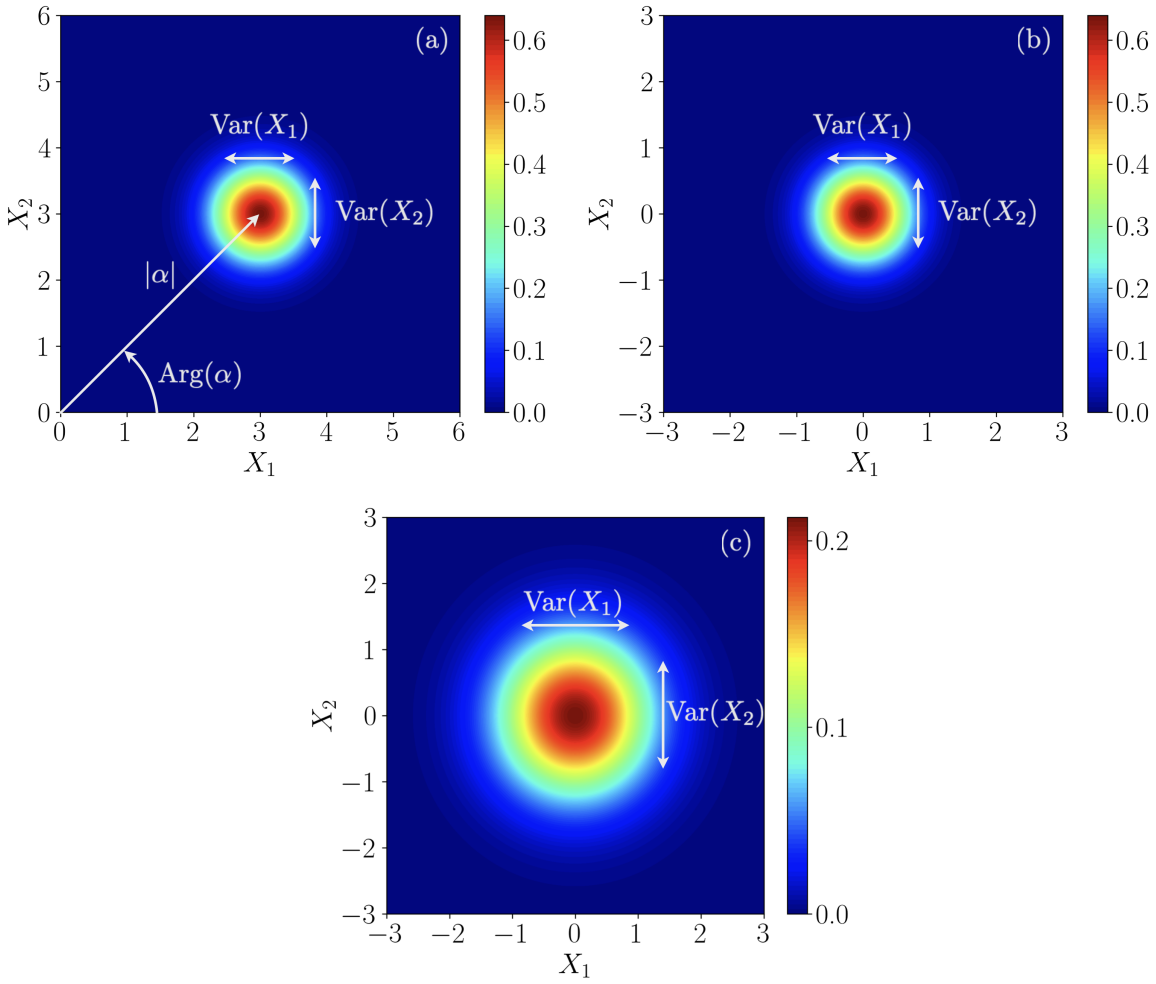

FIGURE 5.1: Wigner function of a coherent (a), vacuum (b), and a thermal state (c). The coherent state corresponds to $|\alpha\rangle = |3 + 3i\rangle$, while for the thermal state, the mean number of photons is $N = 1$. We illustrate the field quadrature variances in all panels by arrows drawn to scale. The length of these arrows corresponds to twice the square root of the quadrature variance. In panel (a), we also depict the distance $|\alpha|$ from the phase-space origin to the Wigner function centre, and the angle $\mathrm{Arg}(\alpha)$ it forms with the X_1 axis.

As shown in Fig. 5.1(a), $W_{|\alpha\rangle}(X_1, X_2)$ is a two-dimesional Gaussian function located at a distance $|\alpha|$ from the origin with variances $\mathrm{Var}(X_1) = 1/4 = \mathrm{Var}(X_2)$, regardless of the value of α. For vacuum, the Wigner function is the same as for a coherent state but located at the phase-space origin, as depicted in Fig. 5.1(b). For thermal light, the Wigner function is also a 2D Gaussian function but with variances

$$\mathrm{Var}(X_1) = \frac{1}{4} + \frac{N}{2} = \mathrm{Var}(X_2), \tag{5.2}$$

as depicted in Fig. 5.1(c) for a mean number of photons $N = 1$. The Wigner function in

Eq. (5.1) has already been reconstructed for weak coherent states with up to a few tens of photons in continuous-wave setups [BSM97; BS97], or up to a few photons per pulse with pulsed sources [Smi+93a; Han+01; Zav+02]. These weak coherent states have been produced by strongly attenuated laser beams.

The density matrix and the Wigner function of a quantum system contain the same information about the system. Indeed, there is a mathematical transformation that maps phase-space functions into Hilbert-space operators in the Schrödinger picture. This transformation is known as the Weyl transformation [Wey27], whereas the inverse mapping is called the Wigner transformation. In particular, the density matrix is the Weyl transform of the Wigner function, and conversely, the Wigner function is the Wigner transform of the density matrix. Therefore, measuring the Wigner function of a quantum system is equivalent to having complete knowledge about the system, or what is the same as having its density matrix. From a practical point of view, the set of marginal distributions used to reconstruct the Wigner function experimentally can also yield the density matrix in the Fock basis [DMP94; Leo+96], as has already been demonstrated for coherent and other quantum states [BSM97; Han+01]. A more direct strategy to obtain the density matrix bypassing the marginal distributions, known as maximum likelihood, has also been proposed [Hra97; Ban+99] and demonstrated [Jam+01; Lvo04; Zam+05].

Despite the equivalence between the density matrix and the Wigner function, we do not expect to fully characterize the pump field in phase space at the quantum level. On the one hand, from a fundamental point of view, the reason is that such a characterization would require an intractable amount of data, as already mentioned in this chapter concerning the density matrix. On the other hand, from a practical point of view, we need to conveniently attenuate the pump field after the PDC process to avoid detector saturation yet allow some of its main features to be observable in phase space. In other words, we are discarding some pump information via attenuation with the hope of observing a distinctive transition between the undepleted and depleted pump regimes in terms of its Wigner function.

In Sec. 5.2 we describe in detail the experimental technique to obtain the mentioned marginal distributions, called balanced homodyne detection (BHD), as well as how we implemented it in the laboratory to measure the Wigner function of the pump field.

5.2 Balanced homodyne detection

Balanced homodyne detection is a standard technique to experimentally reconstruct the Wigner function of a light field. It was first investigated in the context of quantum optics by H.P. Yuen et al., who showed that BHD can be used to measure the quadrature variance of a light field [YC83]. Indeed, BHD was used in the first detection of squeezed states generated by four-wave mixing and PDC [Slu+85; Wu+86]. Then, it was proposed that the marginal

distributions obtained via e.g. BHD can be used to estimate the quantum state of optical fields [VR89]. This proposal by K. Vogel et al. was experimentally demonstrated by D.T. Smithey et al., who were the first to link the marginal distributions to the Wigner function and to coin the term "tomography" to describe the reconstruction process of quantum states [Smi+93b].

Balanced homodyne detection has been applied to perform quantum state reconstruction of number [Lvo+01], coherent [Smi+93a] and different types of squeezed states [BSM97]. As sketched in Fig. 5.2, BHD relies on the overlapping of a relatively strong coherent classical field, the so-called local oscillator (LO), with the field under study, the signal field, on a balanced BS. Please note that the term "signal" here does not refer to one of the down-converted fields in the OPA, as in signal and idler, but to the field characterized via BHD instead. In our case, this field is the pump after PDC. The two outputs of the 50:50 BS are then detected by photodiodes A and B and the resulting photocurrents subtracted from each other, leading to a photocurrent difference I_-. If the LO and the signal perfectly overlap in space and time, it is possible to show that I_- is proportional to the expectation value of the signal field quadrature $\hat{X}_\theta$ [GK04], i.e.

$$I_- \propto |\beta| \langle \hat{X}_\theta \rangle, \tag{5.3}$$

where $|\beta|^2$ is the intensity of the LO, and $\hat{X}_\theta$ is defined as

$$\hat{X}_\theta = \frac{1}{2}\left(\hat{a}e^{-i\theta} + \hat{a}^\dagger e^{i\theta}\right) = \cos\theta \hat{X}_1 + \sin\theta \hat{X}_2. \tag{5.4}$$

We can also prove a linear dependence between the variances of I_- and $\hat{X}_\theta$ [GK04], i.e.

$$\mathrm{Var}(I_-) \propto |\beta|^2 \mathrm{Var}(X_\theta), \tag{5.5}$$

provided that $|\beta|^2 \gg \langle \hat{a}^\dagger \hat{a} \rangle$. This condition is satisfied whenever the mean number of photons in the LO is much greater than the one in the signal field. Equation (5.5) will play a central role when characterizing our balanced detector in Sec. 5.3.

According to Eq. (5.4), θ is the angle between the X_θ and X_1 axes in phase space. In practice, θ corresponds to the relative phase between the LO and the signal field, as depicted in Fig. 5.2. Therefore, sampling I_- many times for a particular θ can build a probability distribution $P_\theta(X_\theta)$ in phase space along the X_θ axis. Formally speaking, $P_\theta(X_\theta)$ is a marginal distribution of the Wigner function. This marginal distribution is defined by rewriting the Wigner function arguments X_1 and X_2 in terms of the rotated variables X_θ and $X_{\theta+\pi/2}$ using the transformation

$$\begin{bmatrix} X_1 \\ X_2 \end{bmatrix} = \begin{bmatrix} \cos\theta & -\sin\theta \\ \sin\theta & \cos\theta \end{bmatrix} \begin{bmatrix} X_\theta \\ X_{\theta+\pi/2} \end{bmatrix},$$

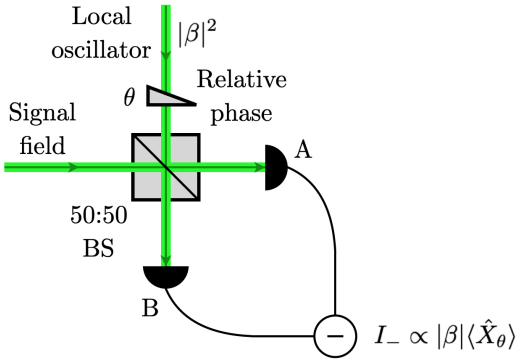

FIGURE 5.2: Balanced homodyne detection scheme. BS: beam splitter.

and then integrating the resulting Wigner function over the conjugate variable $X_{\theta+\pi/2}$ [VR89],

$$P_\theta(X_\theta) = \int_{-\infty}^{\infty} dX_{\theta+\pi/2} W(\cos\theta X_\theta - \sin\theta X_{\theta+\pi/2}, \sin\theta X_\theta + \cos\theta X_{\theta+\pi/2}).$$

Moreover, by tuning $0 \leq \theta < \pi$ in our experiment, we can get a set of marginal distributions across the whole phase space, which are finally used to reconstruct the Wigner function of the signal field, as we will expand later in this chapter. In short, this reconstruction procedure is very similar to the one used in medical computed tomography or X-ray crystallography, where a 3D structure is reconstructed from its shadows or projections along different directions [VR89].

As mentioned above, we implemented the BHD scheme in Fig. 5.2 in the laboratory to reconstruct the Wigner function of the pump field after a PDC process. The resulting experimental setup, shown in Fig. 5.3, was an extension of the one already described in Fig. 4.1 to observe pump depletion. Therefore, the Nd:YAG pulsed laser, the PPLN crystal, the elements to control the input pump power on the crystal, the focusing and collimation lenses for the pump beam, and the dichroic mirror (DM1) to separate the pump from the down-converted fields, are as described in Chapter 4. The LO splits from the laser beam after a combination of HWP (HWP1) and a polarizing beam splitter (PBS1). In the LO path, the beam is directed towards a delay line controlled via a piezoelectric actuator (Thorlabs PK25FA2P2). This actuator controls the relative phase θ between the LO and the signal field. An extra HWP (HWP2) helps balance the LO polarization due to imperfections in the PBSs. We adjusted HWP1 to send up to ~ 210 μW of pump power into the PPLN crystal, enough to observe pump depletion and the rest into the LO path.

Furthermore, we attenuated the pump field two orders of magnitude using ND filters (NE10A×2) before overlapping it with the LO in a second PBS (PBS2). Thanks to these ND filters and the HWP1 setting, we guaranteed that the LO was at least two orders of magnitude brighter than the pump field, a requirement already discussed in connection with Eq. (5.5) to hold valid. We also satisfied the LO and pump field overlap in space and time

by generating them at the same laser source. Hence, the LO can sample the pump field in its rapidly oscillating ($\sim 10^{14}$ Hz) reference frame. This superposition in time means that the LO and pump field share the same optical frequency, justifying the term "homodyne" in the BHD technique name. Indeed, if the same laser source generates the LO and pump field, their frequencies are the same, and their initial relative phase is fixed.

After PBS2, a BP filter (Thorlabs FL532-10) removed any leak from the down-converted fields. Then, an ND filter (Thorlabs NE50A) attenuated the LO and pump field to avoid detector saturation, whereas a positive lens focused both fields at the photodiode locations. At this point, the LO and pump field have polarizations orthogonal to each other, so another HWP (HWP3) was required to make them polarization indistinguishable and able to overlap in this degree of freedom. The resulting combined field was split by a PBS (PBS3), and the transmitted and reflected outputs were finally redirected towards photodiodes A and B, respectively. The last set of HWPs and PBSs, HWP4+PBS4 and HWP5+PBS5, were placed to compensate for potential differences between the two PBS3 outputs. To this end, we set the pump polarization diagonally using HWP3 (LO blocked) and adjusted the HWP4 and HWP5 angles such that I_- vanishes. We discard any spectral broadening across the optical elements on the LO and pump field paths because the group velocity dispersion is negligible for pulse durations on the order of tens of picoseconds.

Please note that we did not use a 50:50 BS in our experimental setup to overlap the LO

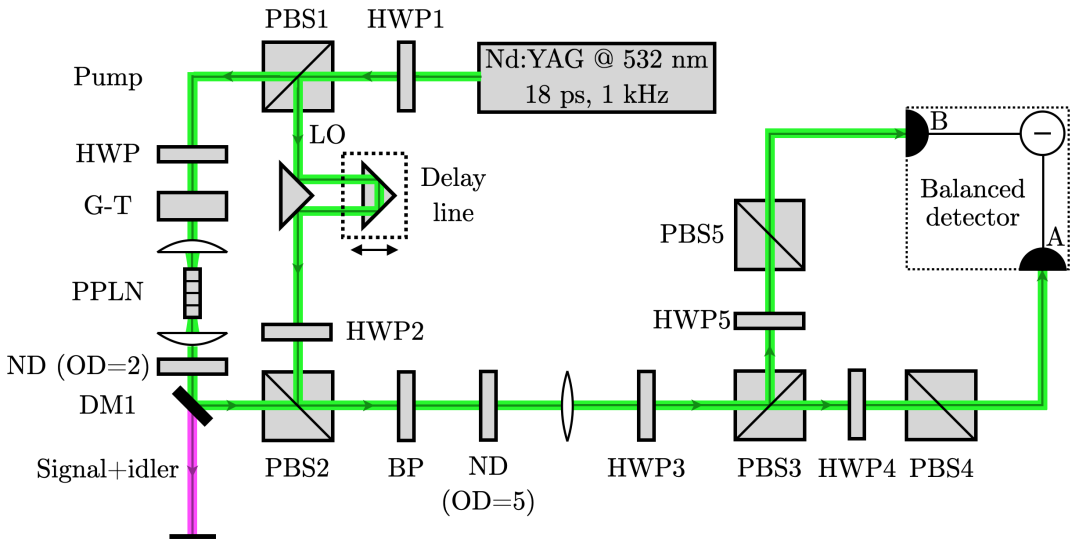

FIGURE 5.3: Experimental setup to balanced homodyne the pump field after a PDC process with pump depletion. Nd:YAG: neodymium-doped yttrium aluminium garnet (laser), HWP: half-wave plate, PBS: polarizing beam splitter, G-T: Glan-Thompson (prism), PPLN: periodically-poled lithium niobate (crystal), ND: neutral density (filter), OD: optical density, DM: dichroic mirror, LO: local oscillator, BP: band-pass (filter). The HWP behind the G-T prism is not enumerated to match the notation in Fig. 4.1.

and the pump field, as was suggested by the BHD scheme in Fig. 5.2. This balanced BS, from which the term "balanced" in BHD comes from, removes classical-like fluctuations on the LO and allows us to make measurements at the shot-noise level [YC83], as we will explain in Sec. 5.3. However, commercially available 50:50 BSs display a non-balanced and non-tunable splitting ratio in practice. Therefore, we used a combination of PBS+HWP+PBS (PBS2, HWP3 and PBS3, respectively) to overlap the LO and pump field in the most balanced way possible. Both HWP2 and HWP3 provided fine control over this balancing by tuning the polarization of the fields. This combination of PBSs and HWPs has been used elsewhere to overcome the technical limitations on 50:50 BS in the BHD context [Smi+93a; Smi+93b].

In Sec. 5.3 we provide further details on how we balanced our BHD setup. Moreover, we test the validity of Eq. (5.5) for our balanced detector and illustrate its working principle.

5.3 Balanced homodyne detection in time domain

Balanced homodyne detection is based on the subtraction of two photocurrents, as previously illustrated in Figs. 5.2 and 5.3. Suppose the light source used in the experiment is a pulsed laser, like in Fig. 5.3. In that case, one can measure the photocurrent difference I_- on a pulse-by-pulse basis, i.e. we can obtain a single value of I_- from each detected pulse. If this is the case, we are dealing with BHD in *time* domain, a technique used for the first time by D.T. Smithey et al. [Smi+92], and subsequently used by others [Smi+93b; And+95; Han+01]. In contrast, *frequency*-domain BHD requires selecting a low-noise detection bandwidth to measure the quadrature variances of the signal field. Some authors have implemented frequency-domain BHD with pulsed lasers [HM90; DF00], but this method implies sampling the signal field only within the detection bandwidth chosen for measurement.

Given our expertise in detecting and processing laser pulses from Chapter 4, we decided to perform time-domain BHD in our experiment. To do so, we used a custom-made photodetector similar to Pd1 in Fig. 4.1 but with two photodiodes on the printed circuit board instead of one. A picture of the actual device is shown in Fig. 5.4, panel (a), along with a simplified version of the circuit in panel (b). In this device, the photocurrent subtraction takes place analogically in a 470 pF capacitor upon pulsed laser illumination of photodiodes A and B (Hamamatsu S3883). The quantum efficiency of the photodiodes is 75% at 532 nm, which can be enhanced to 86% if another set of photodiodes (Hamamatsu S3072) is used instead. Then, preamplification (Amptek 250) and amplification (Amptek 275×2) stages transform the photocurrent difference into an output voltage pulse, as indicated by dotted arrows in Fig. 5.4(b). Finally, we record the output voltage pulses with a 14-bit analogue-to-digital converter card (NI PCI-5122, not shown in Fig. 5.4). The design of the described device is based on the one reported by H. Hansen et al. to measure the Wigner function of a coherent state with a few photons per pulse [Han+01]. Further details about the circuit working principle can be found in Ref. [RB04].

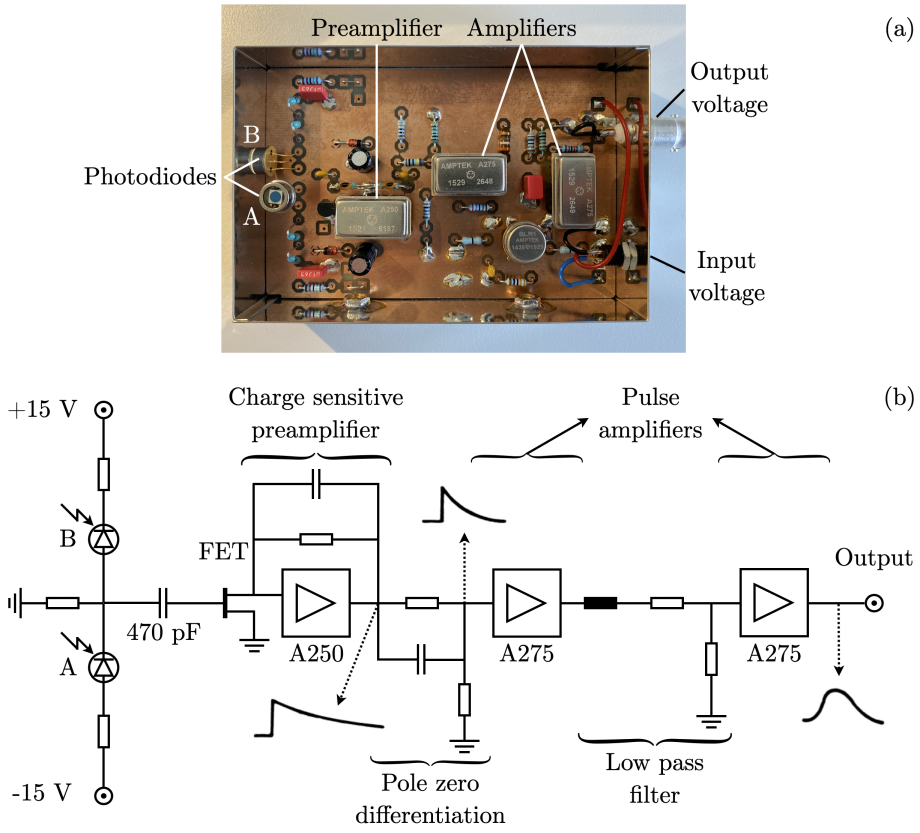

FIGURE 5.4: Balanced detector used in homodyne detection. In panel (a), we show an actual picture of the device, which was built on a printed circuit board and placed inside a metal box with dimensions 150 mm × 100 mm × 30 mm. The output voltage provides a voltage pulse whose temporal integral gives the photocurrent difference I_-. In panel (b), we present a simplified version of the circuit diagram. FET: field-effect transistor.

The temporal response of our balanced detector is presented in Fig. 5.5. If we block one of the two photodiodes, the other one yields either a positive or negative voltage pulse upon detecting a laser pulse, depending on which photodiode we block. For example, if photodiode B is blocked, we get a positive pulse due to photodiode A, like the one shown in panel (a). This behaviour is the same as the one displayed by Pd1 in Fig. 4.1. Conversely, if photodiode A is blocked, we get a negative pulse due to photodiode B, as we also show in Fig. 5.5(a). When both photodiodes are unblocked, the resulting difference pulse displays positive and negative voltages, as shown in panel (b). These positive and negative voltages come from a mismatch between the temporal responses of the two photodiodes. Although we picked the two most similar photodiodes from a batch of ten photodiodes in terms of dark current and capacitance, their temporal response is different. For comparison, we also show the electronic noise when blocking both photodiodes.

Nevertheless, we integrated each pulse difference and obtained a positive or negative area

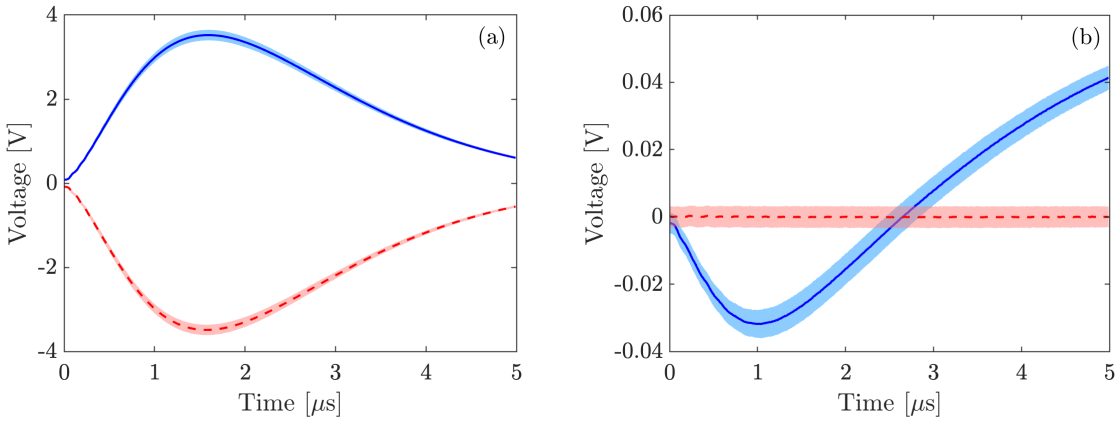

FIGURE 5.5: Temporal response of the balanced detector. In panel (a), we show the voltage pulse for each photodiode, where the one on top (blue solid) corresponds to photodiode A and the one on the bottom (red dashed) to photodiode B. In panel (b), we have the pulse difference (blue solid) and the electronic noise (red dashed). Each point in these plots has been obtained after averaging over 2000 measurements. The shaded area in panel (a) has a total width of ten times the standard deviation for visualization reasons, while in panel (b), it is twice the standard deviation.

that we interpreted as the photocurrent difference in units of volt times second ($\mathrm{V}\cdot\mathrm{s}$). This integration was also carried out in Chapter 4 when we calculated the number of photons as a linear function of the area under the voltage pulse. We integrated the temporal response of our balanced detector up to 5 μs because we observed in Fig. 5.5(a) that most of the area under the voltage pulses is contained within this time window. Recall that the time between pulses is 1 ms (from a laser repetition rate of 1 kHz), meaning that a voltage pulse of a few microseconds effectively corresponds to a single light pulse. However, it would be worth exploring the effect of a longer integration time.

According to Eq. (5.5), the variance of I_- is expected to grow linearly with respect to the LO intensity $|\beta|^2$ for a fixed quadrature variance $\mathrm{Var}(X_\theta)$. If this is so, authors often say that the detection scheme is fundamentally limited by the shot-noise level of the LO [Smi+93a; Smi+93b; Han+01]. To test if our balanced detector satisfies Eq. (5.5), the most convenient signal field to sample is the vacuum state because it has a constant quadrature variance in all directions in phase space, as we explained in Sec. 5.1 and illustrated in Fig. 5.1. Therefore, Eq. (5.5) reduces to $\mathrm{Var}(I_-) \propto |\beta|^2$. Experimentally, we can easily sample the vacuum state by blocking the pump field at the entrance of PBS2 in Fig. 5.3. The result for I_- and the corresponding variance is shown in Fig. 5.6 as a function of the photocurrent sum I_+, which is proportional to $|\beta|^2$. Unfortunately, we only have access to I_- in the balanced detector shown in Fig. 5.4, and not to the photocurrents from photodiodes A and B separately. Therefore, to obtain both I_- and I_+, we run the experiment three times in total, one with both photodiodes

unblocked and two more with either of the two photodiodes blocked. We registered I_- during the first run, while I_+ is the sum of the photocurrents for the last two runs.

When the detector is balanced, i.e. when I_- vanishes in Fig. 5.6(a), we observe that $\mathrm{Var}(I_-)$ scales linearly with I_+ in panel (b). Hence, our balanced detector satisfies Eq. (5.5) for a fixed quadrature variance or, in other words, it is fundamentally limited by the shot-noise level of the LO within the studied range of I_+ values. In particular, our detector can resolve vacuum noise from individual pulses with a signal-to-noise ratio of 4.8 dB with respect to the electronic noise, calculated at $I_+ = 2.1\times10^{-5}$ V·s from Fig. 5.6(b). This signal-to-noise ratio implies that the electronic noise variance is approximately three times lower than the LO shot-noise level, which is twice the signal-to-noise ratio reported in a similar BHD setup [Smi+93a]. Despite this low signal-to-noise ratio, it is enough to carry out the characterization of the pump field. More careful engineering of our homemade balanced detector may increase the signal-to-noise ratio by reducing the electronic noise.

We studied a second scenario in Fig. 5.6 where we carefully unbalanced I_- by tuning HWP3 in Fig. 5.3 so that there is more light illuminating photodiode A. The purpose of unbalancing the detector is to test the ability to properly measure the field quadrature $\hat{X}_\theta$ when its mean value $\langle\hat{X}_\theta\rangle$ is relatively large, as we expect for the attenuated pump field. We observe in Fig. 5.6(a) that, while I_- is unbalanced but constant around 2.2×10^{-7} V · s, its variance increases linearly with I_+ in panel (b), as in the balanced scenario. However, there is a slight discrepancy in the linear fit slopes depending on the balancing. In the balanced scenario, this slope is equal to $8.2(2)\times10^{-12}$ V · s, while in the unbalanced one it is $7.1(2)\times10^{-12}$ V · s. We attribute such a discrepancy ($\sim 13\%$) to slight nonlinearities in the detector amplification stages for an unbalanced signal with respect to a balanced one.

The physical meaning of the slopes in Fig. 5.6(b) is the following. Any I_- registered by the detector is proportional to the photon number difference N_- in the photodiodes, i.e. $I_- = AN_-$, where A is a constant with photocurrent units (V · s). Therefore, the variances of I_- and N_- satisfy

$$\mathrm{Var}(I_-) = A^2\mathrm{Var}(N_-).$$

However, $\mathrm{Var}(N_-)$ is exactly equal to $|\beta|^2$ for the vacuum state [GK04]. Thus,

$$\mathrm{Var}(I_-) = A^2|\beta|^2 = AI_+, \tag{5.6}$$

where we have used $I_+ = A|\beta|^2$ to get the last equality. According to Eq. (5.6), the slope in a $\mathrm{Var}(I_-)$ vs I_+ plot when homodyning the vacuum state is the calibration constant A of our balanced detector. Since we have two slopes in Fig. 5.6(b), we decided to take the average of these two results to get a more accurate calibration constant. This is $A = 7.7(3)\times10^{-12}$ V·s, which allows us to find the mean number of LO photons associated to any I_+ value. For instance, $I_+ = 2.1\times10^{-5}$ V · s is equivalent to $\sim 2.8\times10^6$ photons per pulse. We can also estimate the electronic noise in terms of electrons per pulse. This is the ratio between

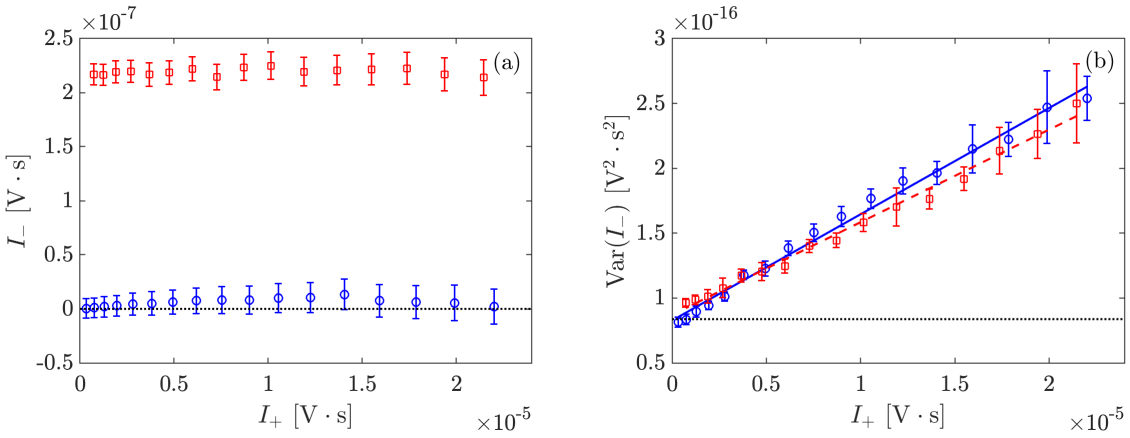

FIGURE 5.6: Photocurrent difference I_- (a) and its variance (b) as a function of the LO intensity I_+. In each panel, we examine two scenarios, when the detector is balanced (blue circles) and when it is unbalanced (red squares). In both scenarios, the resulting variance depends linearly on I_+, although with a greater slope in the balanced scenario (blue solid) with respect to the unbalanced one (red dashed). We also display the electronic noise and its variance by black dotted lines in panels (a) and (b), respectively. Each data point is a statistics over 10000 experimental values.

the electronic-noise variance square root and the calibration constant. The result is ~ 1200 electrons per pulse.

Now that we have characterized our balanced detector in the time domain, showing in particular that it reaches the shot-noise level when sampling the vacuum state, we shall report the Wigner function of the pump field after a PDC process in Sec. 5.4.

5.4 Homodyne detection results

Before performing time-domain BHD on the pump field, we decided to measure the Wigner function of our laser source without any PDC process involved. This measurement will allow us to contrast the laser field BHD results with those for the pump field to discriminate the state of the pump field in the depleted regime. To measure the laser field, we just removed the PPLN crystal from our experimental setup in Fig. 5.3 and set the laser brightness similar to the pump one that we shall investigate later.

The BHD results and the reconstructed Wigner function for the laser field are shown in Fig. 5.7. In particular, we present single-shot data points of the quadrature amplitude X_θ in Fig. 5.7(a). We obtained these points by periodically varying the relative phase θ and registering ~ 5000 oscillation periods of the photocurrent difference I_- with 60 data points each. We adjusted each period to a cosine function, and from the resulting fit, we retrieved θ associated with each I_- point. To obtain X_θ from I_-, we used the "equality" version of

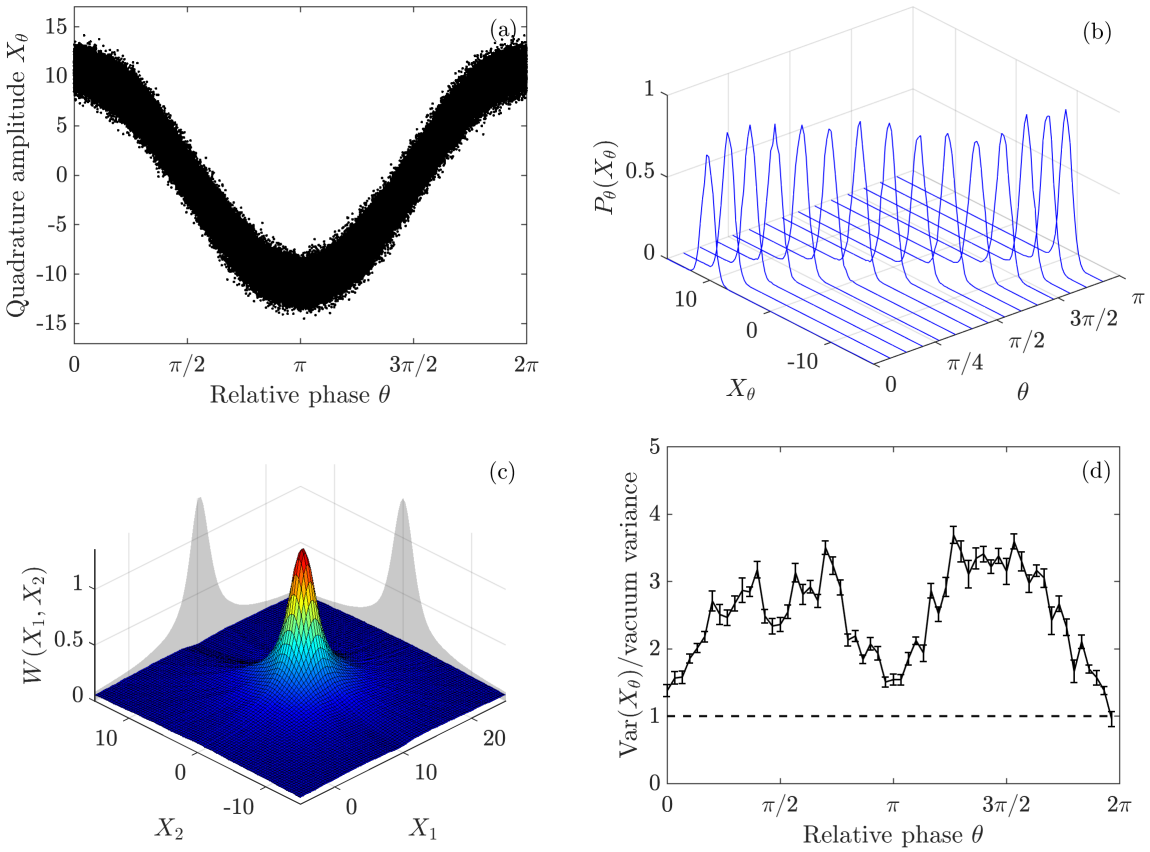

FIGURE 5.7: Time-domain balanced homodyne detection of the laser field with ~ 100 photons per pulse on average. In panel (a), we have $\sim 3 \times 10^5$ single-shot data points of the quadrature amplitude X_θ as a function of the relative phase θ. In panel (b), we plot the marginal distributions $P_\theta(X_\theta)$ required to reconstruct the Wigner function via the inverse Radon transform, which is shown in panel (c). Only half of these marginal distributions are plotted in the $0 \leq \theta < \pi$ range for visualization reasons. In panel (d), we have the quadrature X_θ variance after subtracting the electronic noise variance according to Eq. (5.8). The error bars were multiplied by a factor of 5 for improved visibility. The horizontal (black dashed) line indicates the vacuum state variance.

Eq. (5.3). This is,

$$X_\theta = \frac{I_-}{2A|\beta|}, \tag{5.7}$$

where we first divide I_- by the calibration constant A from Sec. 5.3 to get the photo number difference N_- and then divide the result by two times the LO amplitude [GK04].

Based on the single-shot X_θ data points, we defined 60 marginal distributions $P_\theta(X_\theta)$ in the $0 \leq \theta < 2\pi$ range, with 360 bins each. However, only those distributions in the $0 \leq \theta < \pi$ range are required to reconstruct the Wigner function since the projections along the θ, and $\theta + \pi$ phase-space axes are exactly the same [VR89]. For instance, the Wigner function projection

along the $\pi/4$ axis is the same as the one along the $5\pi/4$ axis. The marginal distributions in the $0 \leq \theta < \pi$ range and the resulting Wigner function for the laser field are presented in Fig. 5.7(b) and (c), respectively. We reconstructed the Wigner function from the marginal distributions via the inverse Radon transform [Rad17; VR89], a widely used method in medical computed tomography [KS88] and other applications [Dea07]. In quantum optics, it has been used to reconstruct the Wigner function of different light quantum states [Smi+93b; BSM97; Han+01; Lvo+01; LM02]. A review of the inverse Radon transform application in quantum optics, also known as quantum state tomography, can be found in Refs. [Sch01; Leo10].

Using the X_θ data points in Fig. 5.7(a), we can directly reconstruct the density matrix of the laser field using the maximum likelihood algorithm, as mentioned earlier. From this density matrix, we can compute the corresponding Wigner function with several improvements over the one obtained via the inverse Radon transform in Fig. 5.7(c) [Lvo04]. However, our emphasis is not to get a precise representation of the laser field in phase space but to examine the response of our BHD setup and balanced detector instead. Recall that the main challenge in our experiment is to sample a bright pump field properly, in contrast to the weak fields commonly studied in time-domain BHD [Smi+93a; Han+01; Zav+02]. Therefore, we focused our attention on the quadrature X_θ variance and used it to characterize our BHD setup and detector response to bright light fields.

For the laser field, the resulting X_θ variance normalized to the vacuum variance ($= 1/4$) is presented in Fig. 5.7(d). We calculated the X_θ variance from Eq. (5.7) as

$$\mathrm{Var}(X_\theta) = \frac{\mathrm{Var}(I_-)}{4A^2|\beta|^2} = \frac{\mathrm{Var}(I_-)}{4AI_+},$$

where we used $I_+ = A|\beta|^2$ again to get the last equality. As in the case of the vacuum state in Sec. 5.3, I_+ is the sum of the photocurrents from photodiodes A and B when we blocked the laser field. Now, we must consider the electronic noise in calculating this variance. If we assume that X_θ and the electronic noise are two independent variables, which is a reasonable assumption in our experiment, then the X_θ and electronic noise variances add up and are equal to the I_- variance, i.e.

$$4AI_+\mathrm{Var}(X_\theta) + \mathrm{Var}(\text{electronic noise}) = \mathrm{Var}(I_-).$$

From this expression, we obtain

$$\mathrm{Var}(X_\theta) = \frac{\mathrm{Var}(I_-) - \mathrm{Var}(\text{electronic noise})}{4AI_+}, \tag{5.8}$$

which tells us that we must subtract the electronic noise variance from $\mathrm{Var}(I_-)$ in order to get a result for $\mathrm{Var}(X_\theta)$.

Under ideal experimental conditions, we expect the laser field to reproduce the features

of a coherent state, although this was not exactly our case. On the one hand, the Wigner function in Fig. 5.7(c) qualitatively approaches the Gaussian Wigner function of a coherent state depicted in Fig. 5.1(a). Indeed, we can estimate a number of ~ 100 photons per pulse in this field after attenuation and losses in our experimental setup in Fig. 5.3. This is the largest number of photons in a coherent state that has been sampled using time-domain BHD, with the second-largest being 5.01 photons per pulse [Han+01], to the best of our knowledge. In frequency-domain BHD, the brightest coherent state sampled so far had 25.2 photons on average [BSM97]. However, on the other hand, the X_θ variance in Fig. 5.7(d) is not constant in all directions in phase space, as it should be for a coherent state. Instead, it is close to the expected value at $\theta = 0$, π and 2π, which is up to four times the coherent (or vacuum) state X_θ variance at any other relative phase.

The reason for this excess noise is still under debate. One possibility is the fact that our laser pulses are not Fourier transform-limited, which means that the pulse duration (~ 18 ps) is greater than the minimum possible duration (~ 5 ps, the pulse coherence time) for a given pulse spectral width (~ 0.2 nm) [Die+06]. In practical terms, this means that the pulse front end has a random phase relative to the back end, adding a phase noise when many pulses are sampled. Having transform-limited pulses seems to play an essential role in time-domain BHD [Smi+93a; Han+01; Lvo+01], but we are undecided as to what extent the non-transform-limited pulses introduce excess noise in our quadrature measurements. In Appendix E, we discuss possible solutions to make our laser pulses Fourier transform-limited. Nevertheless, we measured the pump field, keeping in mind that any excess noise in the X_θ variance at relative phases different from 0, π and 2π may come from our laser source and not from the PDC process.

After putting the PPLN crystal back in place, as shown in Fig. 5.3, the resulting single-shot X_θ data points for the pump field are shown in Fig. 5.8. We chose four different input pump powers, two of them in the undepleted pump regime, 52 μW and 86 μW, panels (a) and (b), and two in the depleted regime, 116 μW and 205 μW, panels (c) and (d), respectively. In the undepleted regime, we observe that the X_θ data points are distributed over a cosine-like band, as for the laser field in Fig. 5.7(a). Interestingly, the amplitude of such a band increases as we raise the input pump power from 52 μW to 86 μW. This increment agrees with what we expect from a coherent state $|\alpha\rangle$, namely that X_θ reaches greater values as $|\alpha|$ increases. As illustrated in Fig. 5.1(a), when $|\alpha|$ increases, the distance from the Wigner function to the phase-space origin increases as well, leading to greater X_θ values. Recall that $|\alpha|^2$ is the mean number of photons, and therefore it is directly proportional to the input pump power. In quantitative terms, the amplitude of the cosine band for the pump fields in panels (a) and (b) is $\sim 8.0(5)$ and $\sim 10.0(5)$ respectively, which approximately correspond to a number of photons of $\sim 64(8)$ and $\sim 100(10)$ per pulse. The ratio between these two numbers of photons, 0.6(1), is close to the ratio between the input pump powers 52(1) μW and 86(1) μW, 0.60(1). Therefore, the pump field behaves in agreement with a coherent state in terms of the

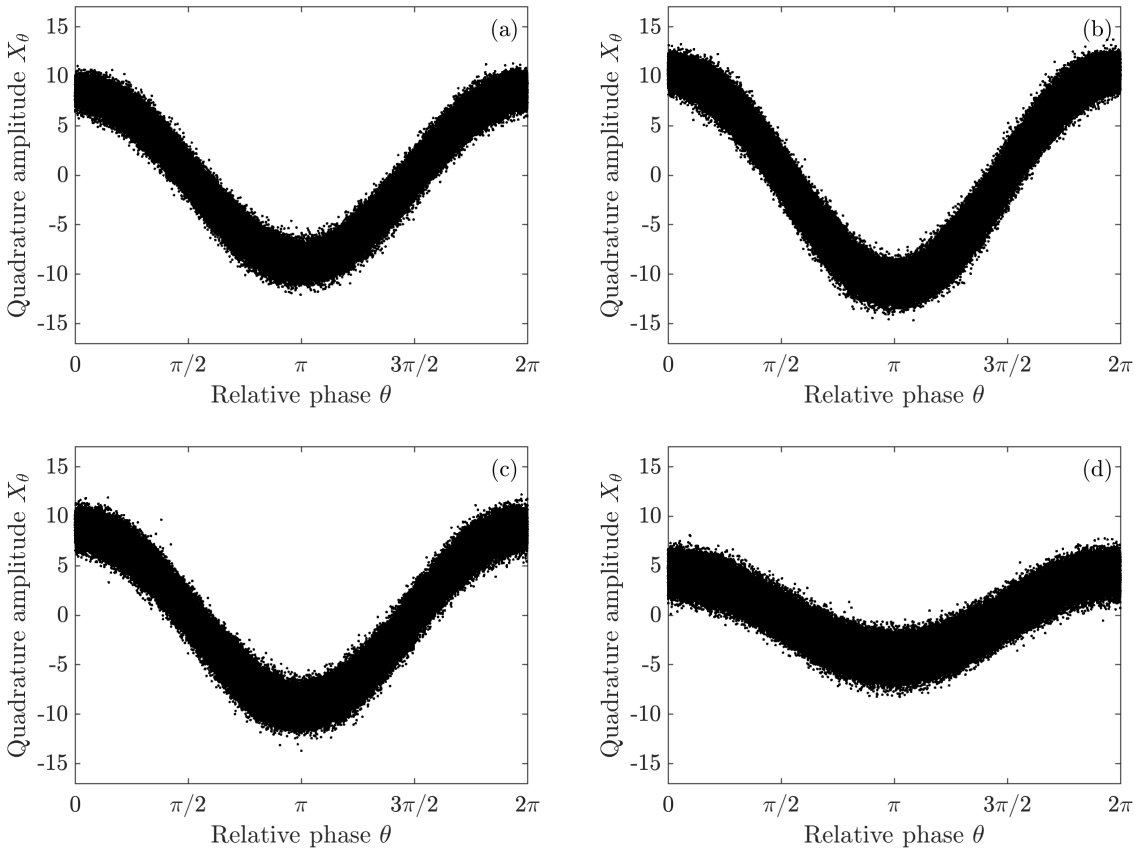

FIGURE 5.8: Quadrature amplitude X_θ for the pump field after a parametric down-conversion process with different input pump powers: 52 μW (a), 86 μW (b), 116 μW (c), 205 μW (d). There are $\sim 3 \times 10^5$ data points in each panel.

quadrature amplitude X_θ in the undepleted pump regime.

In the depleted pump regime, the X_θ data points behave differently. They are still spread over a cosine band, but the amplitude of this band decreases as we raise the input pump power to 116 μW and 205 μW, in contrast to what we observed in the undepleted regime. In particular, for a 205 μW input pump power, the amplitude of the cosine band nearly halves compared to the one at 116 μW. This is direct evidence that the pump field no longer resembles a coherent state in the depleted regime. Furthermore, the vanishing cosine band amplitude suggests that the pump field transitions towards a thermal state, whose X_θ data points are distributed over a non-oscillating band located around $X_\theta = 0$ [BS97]. Recall that the Wigner function of a thermal state is located at the phase-space origin, as depicted in Fig. 5.1(c), which means that all its marginal distributions are centred at $X_\theta = 0$.

Now, if we take a look at the X_θ variances in Fig. 5.9 for the same input pump powers investigated in Fig. 5.8, we find further evidence that supports the previous observations. On the one hand, in the undepleted regime, the X_θ variance approaches the expected value for a

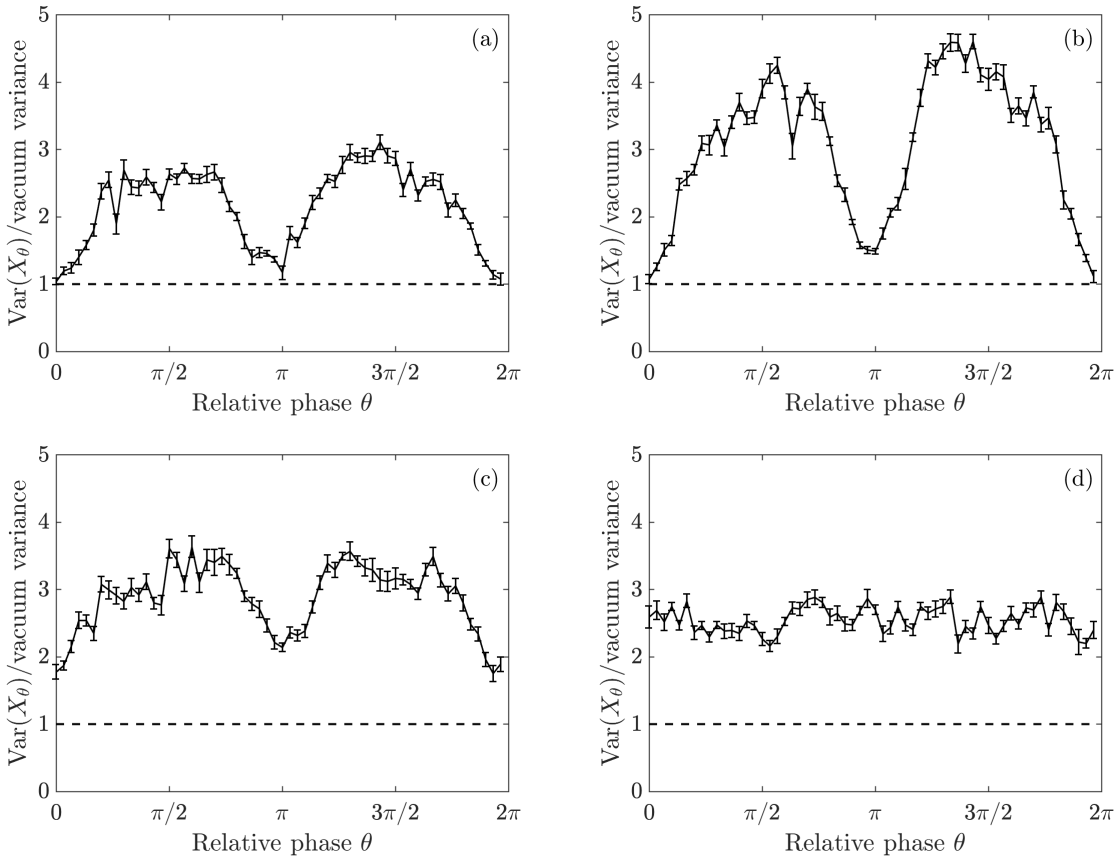

FIGURE 5.9: Quadrature X_θ variance of the pump field after a parametric down-conversion process with different input pump powers. As in Fig. 5.8, the input powers are: 52 μW (a), 86 μW (b), 116 μW (c), 205 μW (d). The error bars were multiplied by a factor of 5 for improved visibility. The horizontal (black dashed) line indicates the vacuum state variance.

coherent state at $\theta = 0$, π and 2π, with excess noise at other θ values. Indeed, such a noise is higher at 86 μW, just before the depleted regime starts. We have already concluded that this excess noise is not a consequence of the PDC process, but it is probably related to the laser source. On the other hand, in the depleted regime, a new type of noise is observed at $\theta = 0$, π and 2π, which takes the X_θ variance away from the coherent variance. This noise is more remarkable at 205 μW, the highest input power investigated in this chapter, where the X_θ variance is almost three times the one for a coherent state and more or less the same for all θ values. This result is what we expect from a thermal state, namely that the X_θ variance be θ independent, as Eq. (5.2) dictates. According to Fig. 5.1(c), the Wigner function of a thermal state is rotationally symmetric in phase space, leading to a uniform X_θ variance regardless of the X_θ axis. Therefore, the results in Fig. 5.9 suggest one more time that the pump field resembles a thermal state in the depleted regime. We also observe that, whatever the source of the excess noise around $\theta = \pi/2$ and $3\pi/2$ is, it vanishes as we enter the depleted

regime and equals the one at $\theta = 0$, π and 2π.

In Sec. 5.5, we summarize what we have achieved and discovered by homodyning the pump field after a PDC process.

5.5 The pump field in phase space

In this chapter we investigated the Wigner function of the pump field after a PDC process in both the depleted and undepleted regimes. We designed and tested a BHD setup for bright light fields to accomplish such a task, expanding the usual BHD capabilities beyond the few-photon level. Despite the technical difficulties attributed to our pulsed laser source, our experimental results displayed distinctive pump features for input pump powers in the depleted vs the undepleted regime. In particular, the single-shot X_θ results follow a cosine band with a decreasing amplitude as the PDC process enters the depleted regime. For example, the amplitude of this cosine band halved when the input pump power nearly doubled in the depleted regime. Likewise, the X_θ fluctuations increased up to three times at the relative phases where the variances were those of a coherent state. These observations resemble the features of a thermal state, whose quadratures X_θ follow a non-oscillatory band and whose X_θ variances are larger than for a coherent state. Therefore, we conclude that in phase space, the pump field approaches a thermal state when transitioning to the depleted regime, as we also claimed in Chapter 4 based on the photon number statistics. Following the same reasoning there, this thermal transition is in qualitative agreement with the increasing von Neumann entropy for the pump predicted by K. Brádler et al. [BA16], and shown in Fig. 1.2, before the Page time. However, no experimental evidence for the turning point in the pump entropy at the Page time was observed, probably due to our PDC process's limited conversion efficiency (33%).

Although we did not measure the von Neumann entropy or the purity for the pump field, we managed to measure its Wigner function after a PDC process, allowing us to draw some conclusions about the black hole evaporation. Mainly, the pump field transitions to a thermal state that resembles what we expect for a black hole; this is, it releases information when evaporating. This information would not be lost but encoded in the outgoing Hawking radiation, which is one of the possible solutions to the information loss paradox described in Chapter 1. Unfortunately, we could not characterize the black hole at the latest stages of its evaporation based on the HR-OPA parallel because we did not observe complete pump depletion. Moreover, it is essential to emphasize that the results on the Wigner function presented here do not fully describe the pump field at the quantum level because of its brightness, as discussed in the introduction of this chapter.

The Wigner function is a widely applied tool in quantum optics nowadays, and yet the study of the pump field after a PDC process using this function had remained mostly elusive [Cas+07]. On top of that, the depleted pump regime is barely explored by the PDC

community [All+14; AB14; PJ+16], which makes the contributions in this chapter novel and a rich line of research. For example, given the multimode character of the down-converted fields, one can investigate the depleted regime in simpler terms via the pump field, which is closer to a single-mode field. Thus, phenomena predicted by the trilinear Hamiltonian, like single-mode squeezing for the pump and tripartite entanglement [DJB93], can be witnessed in principle by looking at the pump. Another line of research can be to illuminate the PPLN crystal with brighter pump fields. In this regard, the two input pump powers P in the depleted regime studied in this chapter, 116 μW and 205 μW, led to a gradual thermalization of the pump field, with the sharpest thermal features occurring at 205 μW. This gradual transition was also observed in terms of the second-order correlation function for the pump field as a function of P in Chapter 4, Fig. 4.4(b). However, the maximum input power considered there was 163 μW, while in the present chapter, we went up to 205 μW. Therefore, a more detailed study of the depleted regime up to input pump powers just below the damage threshold of the PPLN crystal, including both the photon number statistics and the Wigner function, would be an exciting research area.

Chapter 6

Conclusions and future directions

An open problem in modern physics, the black hole information paradox, led us to explore a widely-used device in nonlinear optics, the OPA, under particular operation conditions, where the pump-field dynamics matter. As a result, we investigated the classical nonlinear interaction of three evolving optical waves, the phase sensitivity of a fully quantum nonlinear interferometer, and the properties of the pump and signal fields after PDC in the laboratory. We summarized the conclusions of these investigations as follows.

- Chapter 2: The second-order nonlinear interaction of the pump and down-converted classical fields provides a full description of the number of photons in these fields as they propagate across the nonlinear material. In particular, an oscillatory and complementary behaviour between the pump on the one hand, and the down-converted fields on the other, accompanied by pump depletion and full conversion efficiency, was observed. When comparing with the quantum predictions based on the trilinear Hamiltonian, we concluded that both models provide similar predictions as long as the nonlinear process is seeded, i.e. when the signal or idler fields are in an initial state different from vacuum. However, the classical model predicts no interaction for a vanishing initial number of signal or idler photons, whereas the quantum model provides a maximum conversion efficiency of 78.3% for large input numbers of pump photons.

- Chapter 3: A three-mode nonlinear interferometer exhibits a phase sensitivity that fundamentally scales with the inverse of the input number of pump photons, in what is called the Heisenberg limit [Fl18b]. This result provides the proper phase sensitivity over an extended range of parametric gains, unlike the parametric approximation that predicts an overestimated Heisenberg scaling in the high-gain regime. We also took a look at the three-mode photon number distribution inside the interferometer and found that the optimal phase sensitivity is reached when the corresponding quantum state approaches an N00N-like state.

- Chapter 4: We implemented a PDC process in the laboratory displaying conversion efficiencies up to 33% after being optimized to witness the pump dynamics effect [FLC20]. We concluded that the parametric approximation is no longer valid beyond a specific

input pump power, defining the so-called depleted pump regime. In this regime, the number of signal photons grows linearly with the input pump power and not exponentially, as observed in the undepleted regime. In the case of the pump field, the number of photons reaches a plateau, even when the input power increases. Furthermore, the photon number variance suggests that the signal becomes more coherent while the pump becomes more chaotic when entering the depleted pump regime. Interestingly, the described photon number statistics of the pump and signal fields resembles those of a laser or an optical parametric oscillator, but in the absence of an optical cavity.

- Chapter 5: We achieved the first characterization of the pump field in phase space after a PDC process, to the best of our knowledge. To do so, we implemented a time-domain BHD setup and tested it for bright light fields, i.e. those with a number of photons beyond the few-photon level studied by others so far. Despite some technical difficulties attributed to the non-Fourier transform-limited pulses generated by our laser, we concluded that the pump field quadratures and their respective variances are those of a field transitioning to a thermal state as the PDC process enters the depleted pump regime.

More importantly, we carry out the first attempt to experimentally investigate the black hole information paradox by considering an evolving pump field within the OPA dynamics. If we ignore experimental complications, our results suggest that the pump field evolves into a thermal state while the signal field experiences precisely the opposite effect. If the pump is analogous to a component of the black hole, e.g. the event horizon or the curvature, this would imply that information can flow out of the black hole during its evolution. In this way, information would not be destroyed, and the unitarity of quantum mechanics would be saved.

Nevertheless, our conclusions based on the OPA-HR parallel are far from solving this paradox, partially because of the following experimental challenges:

1. The quantum nature of the pump field quantified via the von Neumann entropy or purity is still elusive in our experiment due to the large number of photons involved in the PDC process. We guess that an OPA based on a physical process involving a significantly less amount of quanta ($\sim 1-10$) [Din+17] would allow the full quantum characterization of the pump field and, thereby, a calculation of e.g. the entropy.

2. The down-converted fields in the PDC process studied in this thesis are generated in multiple modes, making it difficult to compare with the single-mode trilinear Hamiltonian predictions. This multimode feature is unavoidable in a bulk nonlinear crystal but is less remarkable in other configurations, like waveguides [Eck+11].

3. There are wave phenomena like diffraction and group-velocity walk-off involved in the PDC process that may affect the pump and down-converted field properties. For example, preliminary simulations have shown that the pump becomes highly non-Gaussian in

space and time when wave phenomena are taken into account. Once our simulations are completed, we will submit the resulting observations for publication.

Despite these practical challenges, there is still room for at least a couple of improvements in our experimental setup to get enhanced results. For example:

1. We can make our laser pulses Fourier transform-limited, which could correct the excess noise in the pump quadrature variances discussed in Chapter 5. A complete discussion on making Fourier transform-limited pulses by spectrally filtering the laser is presented in Appendix E.

2. We can try input pump powers higher than 205 μW and possibly observe conversion efficiencies beyond 50%, which is when the Page time takes place according to the theoretical results by K. Brádler et al. [BA16] reproduced in Chapter 1. The damage threshold is the only limitation on illuminating the PPLN crystal with higher pump powers. Since this threshold depends on wavelength, pulse duration, average power and repetition rate, it is not easy to find its actual value in the particular case of our laser. Therefore, we can illuminate an unpoled region on the crystal and find out the highest input pump power achieved without damaging the crystal.

We also suggest experimentally investigating a nonlinear interferometer in the depleted pump regime, not only to test our findings in Chapter 3 but also to take advantage of the exciting properties that the pump and down-converted fields display in this regime.

We hope this thesis paves the way to exploring the black hole information paradox based on PDC or other OPA implementation.

Appendix A

Purity calculation for the pump field

In Chapter 1 we reviewed the expected von Neumann entropy for a black hole from the one-shot decoupling method proposed by K. Brádler et al. [BA16]. However, it is challenging to measure the entropy of a quantum system in the laboratory unless we get the full density matrix $\hat{\rho}$ describing the system. Therefore, when the size of $\hat{\rho}$ in the Fock basis is very large, it is worth considering other figures of merit that can be more accessible experimentally speaking and, at the same time, still capture the quantum nature of the system. In this appendix we consider purity as one of those figures of merit, which is defined as

$$\text{Purity} = \text{Tr}(\hat{\rho}^2). \tag{A.1}$$

At first sight, the purity is a more straightforward functional of $\hat{\rho}$ compared to the von Neumann entropy

$$S(\hat{\rho}) = -\text{Tr}\left(\hat{\rho}\ln\hat{\rho}\right),$$

which can be an advantage in practical terms, as we shall see by the end of this appendix in connection with the Wigner function. Another advantage of the purity is that it only takes values between zero (for a maximally mixed state) and one (for a pure state) if $\hat{\rho}$ is appropriately normalized, while $S(\hat{\rho})$ is bounded between zero (for a pure state) and the logarithm of the dimension of the Hilbert space where $\hat{\rho}$ is defined (for a maximally mixed state). If such a dimension tends to infinite, $S(\hat{\rho})$ is unbounded from the top, like in Fig. 1.1 for the signal mode of the OPA under the parametric approximation.

Furthermore, purity is a helpful tool to characterize the degree of entanglement of a composite system, like the black hole plus the radiation fields. If the purity of one of the subsystems is unity, the constituent subsystems are not entangled with each other, and the quantum state for the total system can be represented by the tensor product of the states for each subsystem [GK04]. However, if the purity of one of the subsystems is less than one, we may conclude that the total system is described by an entangled state, which can no longer be factorized into the states for each subsystem. Let us find out if the purity provides the same insight as to the entropy in black hole evaporation.

We obtain the purity of the black hole following the same steps for the von Neumann

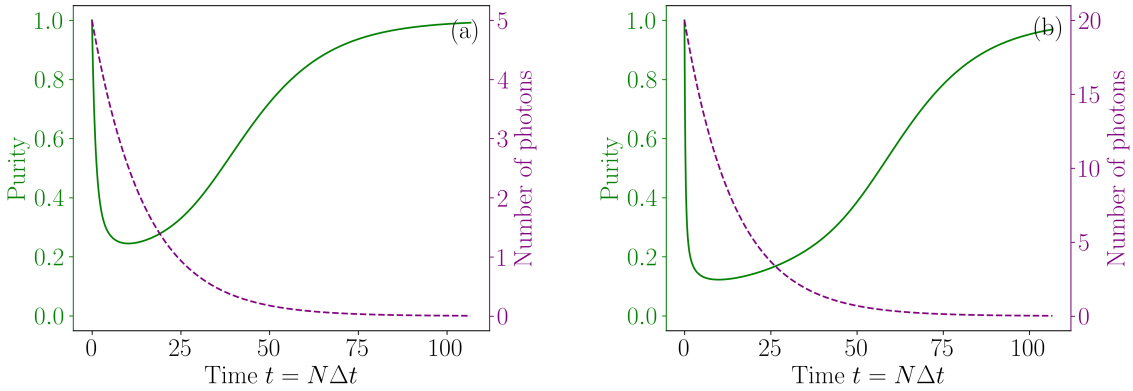

FIGURE A.1: Black hole purity (green solid) from the one-shot decoupling method for $\Delta t = 1/15$ and $N_p = 5$ (a) and $N_p = 20$ (b). We also show the mean number of pump photons (purple dashed). The one-shot decoupling method was implemented via the Quantum Toolbox in Python (QuTiP) [JNN12; JNN13].

entropy in Fig. 1.2. This is, we calculate the density matrix of the total system composed by the black hole and the radiation fields at time $t = N\Delta t$ after N finite time slices of duration Δt. In each time slice, the unitary evolution of the total system is given by the trilinear Hamiltonian, starting with the black hole in the Fock state $|N_p\rangle_a$ at $t = 0$, where $N_p = 1, 2, 3, \ldots$, and the radiation fields in the vacuum state $|0\rangle_b|0\rangle_c$ at every slice. Finally, we take the partial trace over the radiation fields at every slice to get the black hole density matrix and then compute its purity via Eq. (A.1). The result is shown in Fig. A.1.

The first observation about Fig. A.1 is that the purity exhibits the opposite trend than the von Neumann entropy in Fig. 1.2. At $t = 0$, it is maximum due to the black hole starts in the pure state $|N_p\rangle_a$. Then, it decreases as the black hole gets entangled with the radiation fields. When the black hole has depleted to about half of its original size, the purity reaches a minimum value and then increases as it depletes even more and gets disentangled from the radiation fields. For long times, the purity reaches unity again because the black hole has completely evaporated, i.e. it is in the pure state $|0\rangle_a$. Therefore, we conclude that purity is a suitable figure of merit to characterize the black hole evaporation dynamics.

Interestingly, the purity can be calculated from the Wigner function using the trace product rule [Sch01]

$$\mathrm{Tr}(\hat{\rho}_1\hat{\rho}_2) = 2\pi\hbar \int_{-\infty}^{\infty} dq \int_{-\infty}^{\infty} dp W_{\hat{\rho}_1}(q,p) W_{\hat{\rho}_2}(q,p), \tag{A.2}$$

where $W_{\hat{\rho}_j}(q,p)$ denotes the Wigner function associated with the density matrix $\hat{\rho}_j$, $j = 1, 2$. If $\hat{\rho}_1 = \hat{\rho}_2 \equiv \hat{\rho}$, Eq. (A.2) reduces to

$$\mathrm{Tr}(\hat{\rho}^2) = 2\pi\hbar \int_{-\infty}^{\infty} dq \int_{-\infty}^{\infty} dp W_{\hat{\rho}}^2(q,p),$$

which means that the purity of an arbitrary quantum system is given by its squared Wigner function integrated over phase space. Therefore, a full quantum mechanical characterization of the pump field in phase space would lead to Page-like curves by simply integrating its Wigner function squared.

Appendix B

MATLAB code to numerically solve the trilinear Hamiltonian

The following MATLAB code diagonalizes matrix $\mathbf{M}(\theta)$ in Eq. (1.26) (lines 19-28), finds the coefficients $c_\nu(t)$ in Eq. (1.28) (lines 30-35), and reproduces the results in Fig. 1.3 (lines 37-91). It takes 70 s to run in a standard laptop computer (processor 2.5 GHz Quad-Core Intel Core i7 (I7-4870HQ), memory 16 GB 1600 MHz DDR3.)

```
1  clear; % Clear the Workspace
2  close all; % Close all MATLAB figure windows
3
4  % Set font size to 22 points in plots
5  set(0,'DefaultTextFontSize',22)
6  set(0,'DefaultAxesFontSize',22)
7
8  Np = [1,10,100,1000]; % Initial number of pump photons
9  Ns = 0; % Initial number of signal photons
10 theta = 0; % Relative phase between the pump and down-converted
      fields
11 tstep = 0.001; % Time step
12
13 % For each Np, we solve the eigenvalue problem and find the mean
      number of pump, signal and idler photons
14 for p = 1:1:length(Np)
15     Gammaf = 20; % Final parametric gain Gamma considered
16     tf = round(Gammaf/sqrt(Np(p)),3); % Final time
17     T = round(tf/tstep+1); % Number of time intervals
18
19     %Definition of matrix M
20     mu = @(v,theta) exp(1i*theta)*sqrt((Np(p)-v)*(Ns+v+1)*(v+1));
```

```
21      M = zeros(Np(p)+1,Np(p)+1);
22      for v = 0:1:Np(p)-1
23          M(v+1,v+2) = conj(mu(v,theta));
24          M(v+2,v+1) = mu(v,theta);
25      end
26
27      %Diagonalization of matrix M
28      [V,L] = eig(M);
29
30      %Definition of the coefficients cv (the coupling magnitude
            kappa has been absorbed in t)
31      cv = zeros(Np(p)+1,T);
32      for t = 0:1:T-1
33          c = V*diag(exp(-1i*diag(L)*tstep*t))*V';
34          cv(:,t+1) = c(:,1);
35      end
36
37      %Preallocation
38      na = zeros(length(Np),T);
39      nb = zeros(length(Np),T);
40      nc = zeros(length(Np),T);
41
42      %Mean number of signal photons
43      for t=0:1:T-1
44          deltanabar = 0;
45          nabarold = 0;
46          nabarnew = 0;
47
48          deltanbbar = 0;
49          nbbarold = 0;
50          nbbarnew = 0;
51
52          deltancbar = 0;
53          ncbarold = 0;
54          ncbarnew = 0;
55
56          for n=0:1:Np(p)
57              deltanabar = n*abs(cv(Np(p)-n+1,t+1))^2;
58              nabarnew = nabarold + deltanabar;
```

```
59              nabarold = nabarnew;
60
61              deltancbar = n*abs(cv(n+1,t+1))^2;
62              ncbarnew = ncbarold + deltancbar;
63              ncbarold = ncbarnew;
64          end
65
66          for n=Ns:1:Np(p)+Ns
67              deltanbbar = n*abs(cv(n-Ns+1,t+1))^2;
68              nbbarnew = nbbarold + deltanbbar;
69              nbbarold = nbbarnew;
70          end
71
72          na(p,t+1) = nabarnew;
73          nb(p,t+1) = nbbarnew;
74          nc(p,t+1) = ncbarnew;
75      end
76
77      Gamma = (0:tstep:tf)*sqrt(Np(p)); % Parametric gain Gamma
78
79      figure(1)
80      plot(Gamma,na(p,:)/(Np(p)+Ns),'-','Color'
            ,[128/255,0,128/255],'LineWidth',2);
81      hold on
82      plot(Gamma,nb(p,:)/(Np(p)+Ns),'--b','LineWidth',2);
83      %plot(x,nc(p,:)/(Na(p)+Ns),'--r','LineWidth',2);
84      plot(Gamma,(Ns*cosh(Gamma).^2+sinh(Gamma).^2)/(Np(p)+Ns),':k'
            ,'LineWidth',2);
85      %plot(x,(Ns*sinh(x).^2+sinh(x).^2)/(Np(p)+Ns),'--g','
           LineWidth',2);
86      hold off
87      axis([0 20 0 1])
88      set(gca,'YTick',[0.0 0.2 0.4 0.6 0.8 1.0]);
89      xlabel('Parametric gain \Gamma')
90      ylabel('Relative number of photons')
91      saveas(gcf,['MeanPhotonNumber_Np',num2str(Np(p)),'_Ns',
           num2str(Ns),'.png'])
92
93  end
```

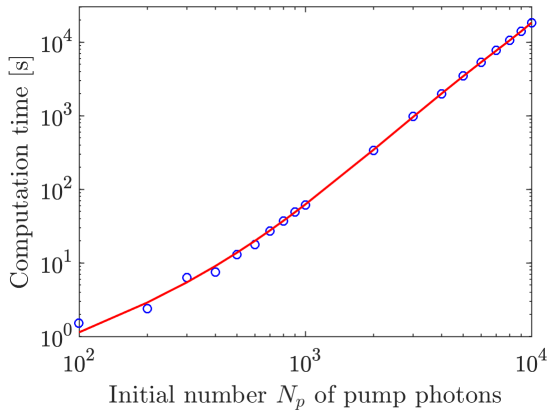

FIGURE B.1: Computation time (blue circles) of the MATLAB code presented in this appendix for different N_p values. Sixth-order polynomial fit (red solid) to the computation time.

In Fig. B.1 we present the computation time of the previous code as a function of the initial number N_p of pump photons. We also present a polynomial fit $a_1N_p + a_2N_p^2 + a_3N_p^3 + a_4N_p^4 + a_5N_p^5 + a_6N_p^6$ to the computation time, with the fitting parameters given in Table B.1. Although a sixth-order polynomial fit seems to describe the computation time accurately, we think a comprehensive study on N_p may reveal a higher-order polynomial dependence. We also suspect that the previous code can be optimized by both diagonalizing matrix $\mathbf{M}(\theta)$ in line 28 and calculating the matrix multiplication in line 33 in a more efficient way.

TABLE B.1: Sixth-order polynomial fitting parameters ($a_1N_p + a_2N_p^2 + a_3N_p^3 + a_4N_p^4 + a_5N_p^5 + a_6N_p^6$) for the computation time to numerically solve the trilinear Hamiltonian.

Parameter	**Value**
a_1	9.0×10^{-3}
a_2	2.0×10^{-5}
a_3	3.6×10^{-8}
a_4	-2.5×10^{-12}
a_5	-4.3×10^{-17}
a_6	1.0×10^{-20}
R^2	0.999998

Appendix C

A variable partially polarizing beam splitter

The first year of my doctoral studies was devoted to developing an optical device that we call a variable partially polarizing beam splitter. This device is a polarizing beam splitter whose transmission and reflection coefficients can be controlled independently for the horizontal and vertical polarization. Since this device has no relation with the OPA, we chose to present the design proposals, theoretical models, and experimental demonstration by attaching the resulting publication, Ref. [Fl18a], to this appendix. This reference is reprinted with the permission of AIP Publishing under license number 5076000419596. The contributions from the coauthors are as stated in the Declaration of Authorship at the beginning of this thesis.

A variable partially-polarizing beam splitter has applications in a wide range of very active quantum optics subfields, such as quantum logic gates, quantum state estimation techniques, and wave-particle duality studies (see references within the attached paper). Currently, progress in these areas is being hindered because partially polarizing beam splitters must be custom fabricated by specialist companies and usually miss their target performance specifications. Our designs allow the performance to be tuned. Furthermore, the devices can be constructed with components available in most optics laboratories.

Our group tested the capabilities of our proposed variable partially polarizing beam splitter in the context of quantum state engineering. In particular, we experimentally demonstrated a way to project two photons onto any polarization state based on Hong-Ou-Mandel interference and post-selection [The+18]. Thanks to the variable partially polarizing beam splitter, there were no ancillary photons or nonlinear optics involved. An arbitrary two-photon polarization projector may find applications on loophole-free tests of Bell's theorem [Giu+15; Sha+15], quantum state discrimination [BC09] and quantum computing [Spe08; How+14].

A variable partially polarizing beam splitter

Jefferson Flórez,[a] Nathan J. Carlson, Codey H. Nacke, Lambert Giner, and Jeff S. Lundeen

Department of Physics and Centre for Research in Photonics, University of Ottawa, 25 Templeton Street, Ottawa, Ontario K1N 6N5, Canada

(Received 15 September 2017; accepted 21 January 2018; published online 7 February 2018)

We present designs for variably polarizing beam splitters. These are beam splitters allowing the complete and independent control of the horizontal and vertical polarization splitting ratios. They have quantum optics and quantum information applications, such as quantum logic gates for quantum computing and non-local measurements for quantum state estimation. At the heart of each design is an interferometer. We experimentally demonstrate one particular implementation, a displaced Sagnac interferometer configuration, that provides an inherent instability to air currents and vibrations. Furthermore, this design does not require any custom-made optics but only common components which can be easily found in an optics laboratory. *Published by AIP Publishing.* https://doi.org/10.1063/1.5004805

I. INTRODUCTION

Typical polarizing beam splitters are intended to spatially separate the horizontal (H) and vertical (V) polarization components of an input beam. However, there are several applications in which a particular set of transmission and reflection coefficients for each polarization are required, like in quantum logic gates,[1–3] quantum state estimation techniques,[4,5] and wave-particle duality studies.[6] A device that provides such coefficients is called a partially polarizing or polarization-dependent, beam splitter (PPBS). To illustrate its properties, consider a PPBS illuminated by a diagonally polarized beam, as shown in Fig. 1. Depending on the values of the transmission (T) and reflection (R) coefficients for H and V, one can have any chosen splitting ratio (i.e., T:R) between the two PPBS output ports independently for the horizontally and vertically polarized light.

A PPBS can be built using multilayered dielectric coatings designed for specific T and R coefficients for each polarization. The drawback of this custom-fabricated beam splitter is that such coefficients cannot be tuned for different purposes, including the correction of fabrication caused deviations from the target values of T and R. These can lead to a reduced performance in some applications.[6] Moreover, these devices are not available off-the-shelf and are, thus, expensive. In this paper, a *variable* partially polarizing beam splitter (VPPBS) is introduced featuring a complete and independent control of the horizontal and vertical T and R coefficients. Furthermore, it is based on bulk optical components that are usually available in any optics laboratory.

The working principle of the VPPBS presented here is the interference of two beams in a simple interferometer like a Mach-Zehnder. Consider light entering only one input of the first beam splitter in that interferometer, as shown in Fig. 2. Light interferes constructively or destructively at the last beam splitter depending on the phase between the two optical paths. It follows that the interferometer input light can be made to exit the last beam splitter entirely via output 1 or, alternately, entirely via output 2, or some combination of the two output ports. By tuning the interferometer phase, one can set any desired splitting ratio between these two output ports. Considered in its entirety, the Mach-Zehnder is a beam splitter, with outputs 1 and 2 arbitrarily defined as the effective transmission and reflection beam splitter ports. And so, one can vary the beam splitter T and R coefficients by varying the phase. Now consider both H and V entering the interferometer input. By tuning the phase for each of these polarizations independently, the splitting ratios for H and V can be set independently. With this independent phase control, the Mach-Zehnder is a VPPBS.

II. THEORY

In this section, a theoretical description of the VPPBS mechanism outlined above is presented. (For completeness, in Appendix A, a theoretical description of a nominally distinct, but actually closely related, configuration is presented based on polarizing beam splitters in the place of non-polarizing beam splitters.) Consider an incoming light beam entering at input 1 of the Mach-Zehnder interferometer in Fig. 2. In the H/V basis, such a light beam is characterized by an electric field $\mathbf{E}_{\text{in}}(t)$ of the form

$$\mathbf{E}_{\text{in}}(t) = \begin{bmatrix} E_{\text{in}}^{H}(t) \\ E_{\text{in}}^{V}(t) \end{bmatrix}, \tag{1}$$

where $E_{\text{in}}^{H}(t)$ and $E_{\text{in}}^{V}(t)$ are the H and V polarization components, respectively. After the first 50:50 non-polarizing beam splitter (NPBS) in Fig. 2, the electric fields describing the upper and lower paths just before the phase retarders differ by a phase of $\pi/2$ due to the different number of reflections. This is,

$$\mathbf{E}_{\text{upper}}(t) = \frac{1}{\sqrt{2}}\mathbf{E}_{\text{in}}(t), \quad \mathbf{E}_{\text{lower}}(t) = \frac{e^{i\pi/2}}{\sqrt{2}}\mathbf{E}_{\text{in}}(t). \tag{2}$$

Now, the two phase retarders in the interferometer arms introduce independent phases ϕ_H and ϕ_V to the H and V polarization, respectively. These phase retarders can be, for

[a]Electronic mail:

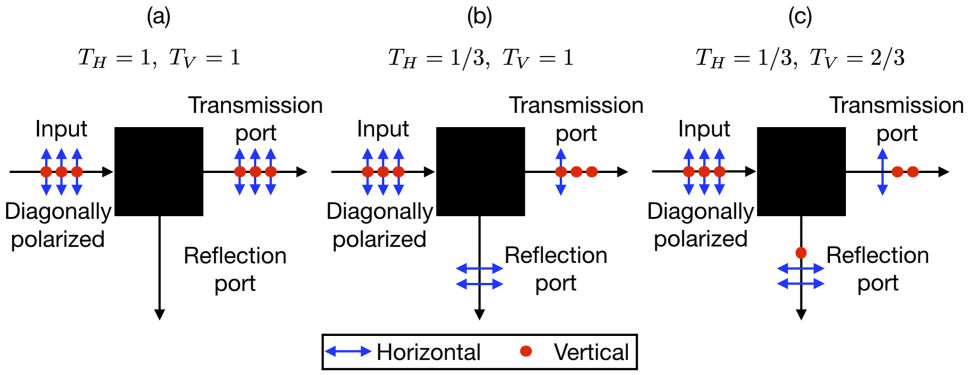

FIG. 1. Schematic representation of a partially polarizing beam splitter. If $T_H = 1 = T_V$ as in panel (a), one will have both the horizontally and vertically polarized light being transmitted by the PPBS, whereas there will be no light coming out at the reflection port. If $T_H = 1/3$ and $T_V = 1$ as in panel (b), one will have one third of the incoming horizontally polarized light being transmitted and the rest reflected, whereas all the vertically polarized light is transmitted by the PPBS. Finally, if $T_H = 1/3$ and $T_V = 2/3$ as in panel (c), one third and two thirds of the horizontally and vertically polarized light are transmitted, respectively, and the rest is reflected.

example, two liquid crystal cells with crystal axes orthogonally oriented to one another, i.e., either along the H or V directions. The electric fields just after the phase retarders and before the second NPBS in Fig. 2 read

$$\tilde{\mathbf{E}}_{\text{upper}}(t) = \frac{1}{\sqrt{2}} \begin{bmatrix} E^H_{\text{in}}(t) \\ e^{i\phi_V} E^V_{\text{in}}(t) \end{bmatrix}, \tag{3}$$

$$\tilde{\mathbf{E}}_{\text{lower}}(t) = \frac{e^{i\pi/2}}{\sqrt{2}} \begin{bmatrix} e^{i\phi_H} E^H_{\text{in}}(t) \\ E^V_{\text{in}}(t) \end{bmatrix}, \tag{4}$$

where it has been assumed without loss of generality that the phase retarder in the upper path introduces the phase ϕ_V, while the one in the lower path introduces ϕ_H. After the second NPBS, i.e., at the outputs of the Mach-Zehnder interferometer, the electric fields become

$$\mathbf{E}_{\text{out},1}(t) = \begin{bmatrix} e^{i\phi_H/2} E^H_{\text{in}}(t) \cos\left(\frac{\phi_H}{2}\right) \\ e^{i\phi_V/2} E^V_{\text{in}}(t) \cos\left(\frac{\phi_V}{2}\right) \end{bmatrix}, \tag{5}$$

$$\mathbf{E}_{\text{out},2}(t) = \begin{bmatrix} -ie^{i\phi_H/2} E^H_{\text{in}}(t) \sin\left(\frac{\phi_H}{2}\right) \\ ie^{i\phi_V/2} E^V_{\text{in}}(t) \sin\left(\frac{\phi_V}{2}\right) \end{bmatrix}. \tag{6}$$

The T coefficient for the horizontal polarization is defined as the ratio between the horizontal light intensity in output 1 and the intensity of that polarization in the input beam. Similarly, T_V corresponds to the ratio between the vertical light intensity in output 1 and the initial intensity of such polarization. In terms of Eqs. (5) and (6), this is

$$T_\epsilon \equiv \frac{|E^\epsilon_{\text{out},1}(t)|^2}{|E^\epsilon_{\text{in}}(t)|^2} = \frac{1 + \cos\phi_\epsilon}{2}, \tag{7}$$

where $\epsilon = H, V$. The fields $E^H_{\text{out},1}$ and $E^V_{\text{out},1}$ are, respectively, the H and V components of $\mathbf{E}_{\text{out},1}$. The reflection coefficients for the horizontal and vertical polarizations are given by $R_H = 1 - T_H$ and $R_V = 1 - T_V$, respectively. Thus, by tuning ϕ_H and ϕ_V, any possible value of reflection and transmission coefficients can be chosen. This constitutes a VPPBS.

The challenge in this design is how to vary ϕ_H and ϕ_V. As mentioned earlier, one possibility for the phase retarders is orthogonally oriented two liquid crystals. Here, the relative phases ϕ_H and ϕ_V are independently tuned by means of the AC voltage applied to each liquid crystal. Another possibility, which is the one implemented here, is to vary the tilt of a uniaxial birefringent crystal (i.e., one with parallel input and output faces) in one of the interferometer arms. Both the refractive index and optical path length will vary differently for the two polarizations as the element is tilted. In turn, the introduced phases ϕ^H_b and ϕ^V_b for the H and V polarizations, respectively, will be differently tuned by the tilt. This will set the phase difference $\Delta\phi = \phi_H - \phi_V$. To achieve full independent control of each phase, tilting a second non-birefringent plate (e.g., glass) can be used to introduce an identical phase ϕ_g

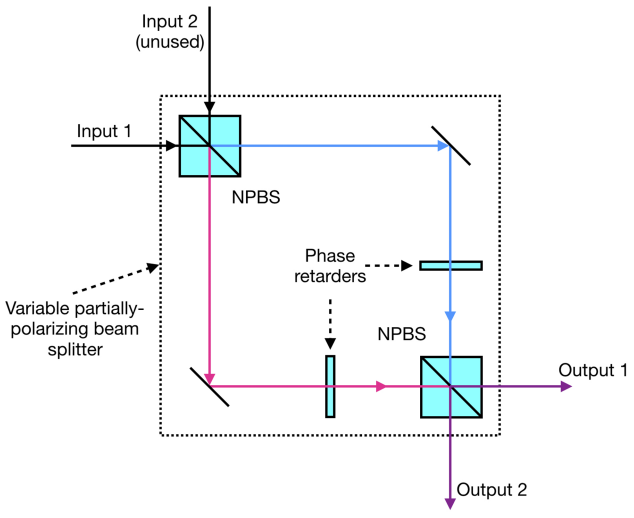

FIG. 2. The basis of the variable partially polarizing beam splitter (VPPBS) presented here is two independent interference processes occurring in a Mach-Zehnder interferometer, one for the horizontal and the other for the vertical polarization. The phase retarders introduce polarization-dependent phases between the two optical paths. Outputs 1 and 2 play the role of the transmission and reflection VPPBS ports, respectively. Non-polarizing beam splitter (NPBS) is a non-polarizing 50:50 beam splitter. That is, a beam-splitter with $T = R = 1/2$ for both polarizations.

offset to the two polarizations so that

$$\phi_H = \phi_b^H - \phi_g, \tag{8}$$

$$\phi_V = \phi_b^V - \phi_g. \tag{9}$$

In summary, with the two tilts as control parameters, it is possible to independently set the two system degrees of freedom, ϕ_H and ϕ_V.

The relative phase ϕ introduced between the two optical paths in a Mach-Zehnder interferometer by a plate of thickness d and refractive index n is $\phi = 2\pi d(n - n_a)/\lambda$, where n_a is the refractive index of air and λ is the wavelength of light. This expression describes the case when the plate is placed in one arm of the interferometer so that it is normal to the beam. In Appendix B, it is shown that if the plate is tilted by θ_p from normal, the relative phase is given by

$$\phi_p^\epsilon = \frac{2\pi d_p}{\lambda}\left[\frac{n_p^\epsilon}{\cos\theta_p'^\epsilon} - n_a\left(\cos\theta_p + \sin\theta_p \tan\theta_p'^\epsilon\right)\right], \tag{10}$$

where $p = b$ or g for the birefringent and glass plates, respectively, and $\theta_p'^\epsilon$ is the angle of light inside the optical medium after refraction. In the case $p = g$, the ϵ label is not used throughout the paper, whereas for $p = b$, $\epsilon = H, V$. In particular, there are two refractive indices n_b^H and n_b^V for the birefringent medium. The angle $\theta_p'^\epsilon$ is given by Snell's law,

$$\theta_p'^\epsilon = \arcsin\left(\frac{n_a}{n_p^\epsilon}\sin\theta_p\right). \tag{11}$$

For simplicity, $\theta_b' \equiv \theta_b'^H$ in the reminder of the paper.

In the present work, the birefringent crystal is tilted around the laboratory vertical axis, which is parallel to the vertical polarization and perpendicular to the optical table, as shown in Fig. 3. Furthermore, the optic axis $\vec{c}$ of the crystal lies on the horizontal plane, which means that the angle θ_c' between $\vec{c}$ and the beam propagation direction changes as the crystal is allowed to rotate around the vertical axis. In this arrangement, the refractive index is constant for the vertical (ordinary) polarization, whereas the effective refractive index for the horizontal (extraordinary) polarization changes as the crystal is tilted according to[7]

$$n_b^H = \left[\frac{\cos^2(\theta_c')}{n_o^2} + \frac{\sin^2(\theta_c')}{n_e^2}\right]^{-\frac{1}{2}}, \tag{12}$$

with n_o and n_e being the ordinary and extraordinary refractive indices of the birefringent crystal, respectively, and θ_c' defined as $\theta_c' = \theta_c + \theta_b'$. We allow for the fact that the chosen crystal might potentially be cut so that crystal axis $\vec{c}$ is at an angle θ_c to the crystal face normal. For the vertical polarization, n_b^V is identically equal to n_o, whereas for the horizontal polarization, the refractive index n_b^H depends on the crystal tilt, as seen from the last equation.

According to Eq. (12), one must know θ_b' to find n_b^H, but at the same time, one needs n_b^H to get θ_b' by means of Eq. (11). Unfortunately, this pair of equations do not have analytic solution for θ_b' and n_b^H. So, in order to be able to contrast the experimental results in Sec. IV with the theoretical predictions, n_b^H is estimated in the following way. First, θ_b' is approximated by θ_b in Eq. (12), resulting in $\theta_c' \approx \theta_c + \theta_b$ which is used to find a zero-order approximation for n_b^H. Second, using this result, a value for θ_b' is calculated via Eq. (11). Third, that result for θ_b' is substituted in Eq. (12) to finally obtain a first-order approximation for n_b^H. Repeating the same steps, a second-order approximation for n_b^H can be calculated. The discrepancy between the zero- and first-order approximations is less than 0.5% and between the first- and second-order approximations is less than 0.004%. In this paper, the second-order approximation is used.

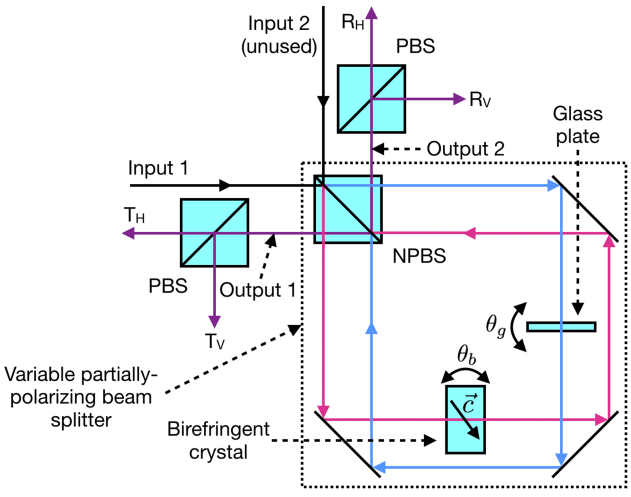

FIG. 3. Experimental realization of a variable partially polarizing beam splitter using a displaced Sagnac interferometer composed of three mirrors and a non-polarizing beam splitter (NPBS). Two polarizing beam splitters (PBSs) have been placed at each output port to study the transmission and reflection coefficients for each polarization. The thickness of the birefringent crystal has been exaggerated to indicate the orientation of its optic axis $\vec{c}$.

III. EXPERIMENTAL REALIZATION

The Mach-Zehnder interferometer shown in Fig. 2 can be used to implement a VPPBS. However, depending on its spatial dimensions and external factors like vibrations and air currents, this interferometer might require active phase stabilization in order to hold a specific set of T and R coefficients for a long period of time, e.g., hours. A variation of the Mach-Zehnder interferometer, called a displaced Sagnac interferometer,[8–10] is used instead to reduce this inherent instability. In this, the light is split by and returns to the same NPBS using three mirrors, as shown in Fig. 3. The two counter-propagating beams inside the interferometer play the same role as the two arms in a Mach-Zehnder. In the non-displaced version of the Sagnac interferometer, the counter-propagating beams inside the interferometer follow exactly the same paths. This makes it difficult to introduce a relative phase between the beams, as it is required in the current scheme. It also means that the beam in output 1 exits along the exact path of the input beam, which makes the output beam difficult to access. A displaced Sagnac interferometer eliminates these issues. In it, one translates the mirror in the Sagnac interferometer that is diagonally opposite to the NPBS. This separates the two counter-propagating paths while maintaining their collinearity.

Given that the transverse separation between the paths is small (~2 cm) compared to the footprint of the interferometer (70 cm × 70 cm) and the fact that the beams are reflected

TABLE I. Comparison between tilted optical medium and liquid crystal methods to control the relative phase in the displaced Sagnac interferometer in Fig. 3.

	Tilted birefringent crystal and glass plate	Liquid crystals
Advantages	Need to align axis only for the birefringent crystal Induced phase is stable over months Tilted medium is usable to its edge, which allows for counterpropagating beam clearance	ϕ_H and ϕ_V each have their own control Normal incidence (i.e., no beam displacement), implying bigger aperture for a given device width
Disadvantages	ϕ_H and ϕ_V are not independently controlled Refractive beam displacement can reduce interference visibility Requires a precision rotation mount (e.g., vernier)	Need to align axes for both liquid crystals Liquid crystal response can change from one voltage ramp to the next Since they are not usable up to their edge, a large Sagnac path separation is required Easy to damage with a DC voltage

and transmitted by the same mirrors and NPBS in the interferometer, any vibration or air current affects both optical paths roughly in the same way, making the Sagnac interferometer stable without active stabilization.[9]

The experiment was carried out using a HeNe laser in free space with wavelength $\lambda = 632.8$ nm. The displaced Sagnac interferometer was built using a broadband (400–700 nm) 50:50 NPBS cube with 2.54 cm side length (Thorlabs BS013) and three 5.08 cm diameter silver mirrors. As mentioned above, the phase retarders can be either two liquid crystals driven by an AC voltage or a birefringent crystal plus a glass plate tilted as shown in Fig. 3. However, only the second case was considered here since such elements are easily accessible in the laboratory. For a full comparison between the tilted optical medium and liquid crystal methods, we refer the reader to Table I. The birefringent crystal was a β barium borate (BBO) crystal of nominal thickness $d_b = 0.245$ mm and nominal optic axis at $\theta_c = 33.4°$; the glass plate was a microscope cover slide of nominal thickness $d_g = 0.16$ mm. These two elements were mounted in automated rotation stages and tilted between $-10°$ and $10°$ in steps of $0.1°$ for θ_b and $0.25°$ for θ_g. The input light was diagonally polarized by means of a polarizing beam splitter (PBS) plus a half-wave plate with its fast axis at $22.5°$ with respect to the horizontal direction. As seen in Fig. 3, at each output port of the VPPBS, a PBS was placed to study the T and R coefficient for both polarizations. The intensities were recorded for each value of θ_b and θ_g by four photodiodes after averaging 100 measurements taken over 2 s.

IV. EXPERIMENTAL RESULTS

To demonstrate the working principle of a VPPBS based on the Sagnac interferometer in Fig. 3, the four coefficients T_H, T_V, R_H, and R_V were measured as described in Sec. III and are shown in Fig. 4(a).

The first observation in Fig. 4(a) is that the VPPBS coefficients exhibit several maxima and minima in the range of θ_b and θ_g values studied here. At these points, there is either constructive or destructive interference due to the relative phases introduced by the birefringent crystal and glass plate. As expected, the T_H and R_H coefficients are complementary to one another, i.e., when T_H is maximum R_H is minimum and vice versa. This complementarity happens as well for T_V and R_V. Furthermore, the coefficients in Fig. 4(a) are symmetric with respect to the axis $\theta_g = 0$, which comes from the fact that the relative phase introduced by the glass plate is the same for both positive and negative θ_g angles. The same happens for T_V and R_V with respect to the axis $\theta_b = 0$ since n_b^V is a constant. By contrast, T_H and R_H are asymmetric with respect to the axis $\theta_b = 0$ because the angle θ_c of the optic axis $\vec{c}$ is not zero when the face of the birefringent crystal is perpendicular to the beam. This creates a difference between a positive or negative tilt of the crystal that only affects the horizontal polarization, in accordance with Eq. (12).

In order to compare the experimental results in Fig. 4(a) with the theoretical model in Sec. II, Eqs. (7)–(12), a least-squares fitting of the experimental data is performed in the following way. First, the experimental visibilities for the four coefficients in Fig. 4(a) are taken into account in the theoretical model by using a modified version of Eq. (7),

$$T_\epsilon = \frac{1 + \mathcal{V}_\epsilon \cos\phi_\epsilon}{2}, \tag{13}$$

where $\mathcal{V}_\epsilon$ is the experimental visibility for the coefficient T_ϵ ($\epsilon = H, V$). The reflection coefficients are still given by $R_\epsilon = 1 - T_\epsilon$. Second, the thicknesses d_b and d_g for the phase retarders are adjusted iteratively using only T_V in Fig. 4(a) since the index of refraction for the V polarization is a constant and therefore independent of θ_c, the third fitted parameter described below (R_V could have been used as well). The adjusted values for d_b and d_g are 0.2724 mm and 0.1477 mm, respectively. Third, using these adjusted thicknesses, the experimental coefficient T_H is iteratively fitted using θ_c and a tilt angle offset θ_0 for the birefringent crystal (such that $\theta_b \to \theta_b + \theta_0$) as fitting parameters. The results for θ_c and θ_0 are, respectively, $32.14°$ and $0.061°$. Finally, the four adjusted parameters are introduced in the theoretical model and the resulting coefficients are depicted in Fig. 4(b). The values for the refractive indices are $n_g = 1.5151$ (BK7 refractive index[11]), and $n_o = 1.6672$ and $n_e = 1.5496$ (from Sellmeier's equations[12] for BBO at $\lambda = 632.8$ nm).

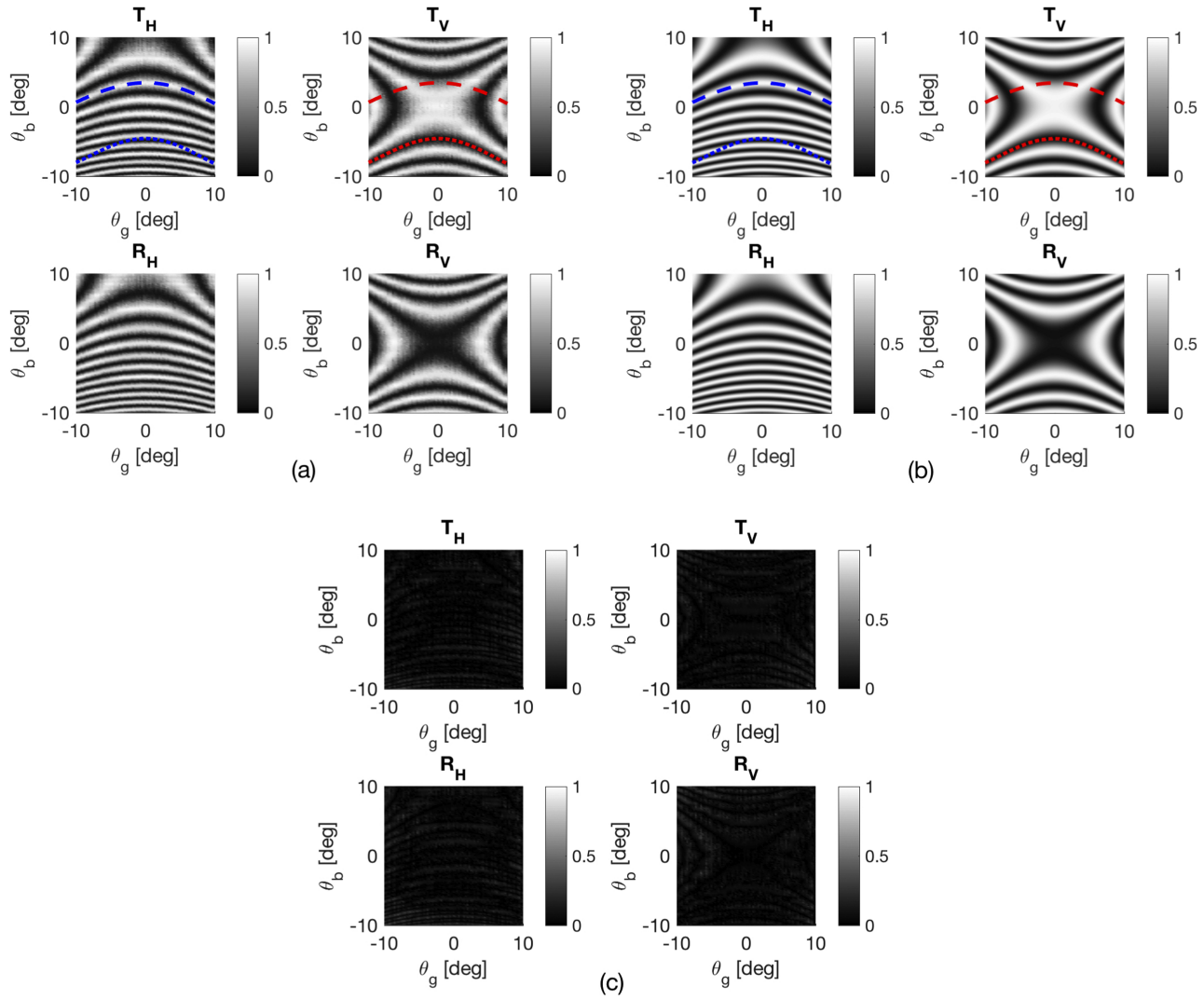

FIG. 4. (a) Experimental transmission T and reflection R coefficients for the horizontal H and vertical V polarizations in the output ports of the variable partially polarizing beam splitter shown in Fig. 3. The axes, θ_b and θ_g, are the tilts of the birefringent crystal and glass plate, respectively. (b) Theoretically expected T and R coefficients for the H and V polarizations of the variable partially polarizing beam splitter in Fig. 3 according to the theoretical model in Sec. II and the fitting procedure explained in Sec. IV. (c) Absolute difference between experiment and theory. The maximum absolute difference for each coefficient is 0.36 (T_H), 0.39 (T_V), 0.43 (R_H), and 0.41 (R_V). The dashed and dotted lines in (a) and (b) correspond to the bands used to illustrate a complete and independent control of the variable partially polarizing beam splitter coefficients in Fig. 5.

In order to easily compare the experimental results to the theory in Fig. 4, a plot showing the absolute difference between the two is presented in Fig. 4(c). Qualitatively, the theoretical model reproduces the experimental VPPBS performance. However, even after all the careful fitting described above, the maximum absolute difference, 0.43, is remarkably large. The refractive indices are the only parameters that were not fitted, which suggests that they may be a contributor to this discrepancy. In any case, we conclude that the theoretical model is insufficiently accurate to predict the required tilt angles for a desired transmission coefficient. Instead, the experimental characterization in Fig. 4(a) must be used.

The VPPBS working principle can be illustrated using Fig. 4(a) by finding the tilt angles at which one of the transmission coefficients is kept constant while the other varies. As an example, it is shown here the case when T_H is kept constant while T_V varies. This can be accomplished by selecting any band in the T_H plot for which this coefficient is constant, e.g., the one marked with a dashed (blue) line in Fig. 4(a). For the same tilt angles that describe such a line in the T_H contour plot, a set of values between 0 and 1 is found for the T_V coefficient, as indicated by a dashed (red) line in Fig. 4(a). The latter case is illustrated in Fig. 5(a), where the T_H and T_V coefficients are shown as a function of θ_g that parametrizes the dashed line in Fig. 4(a). In Fig. 5(b), a second case is considered, T_V set to its minimum value while T_H is varied. One of the bands in the plot for T_V in Fig. 4(a) that fulfills this condition is highlighted with a dotted (red) line. In this case, the T_H coefficient achieves values between 0 and 1 indicated by a dotted (blue) line in Fig. 4(a). Therefore, by selecting an appropriate value for θ_g that parametrizes the dotted line, it is possible to get an arbitrary value for T_H.

The two cases summarized in Fig. 5 illustrate the fact that the T_H and T_V coefficients, and therefore their reflection counterparts, can be controlled at will by choosing two tilt angles. In other words, the relative phases introduced by the birefringent

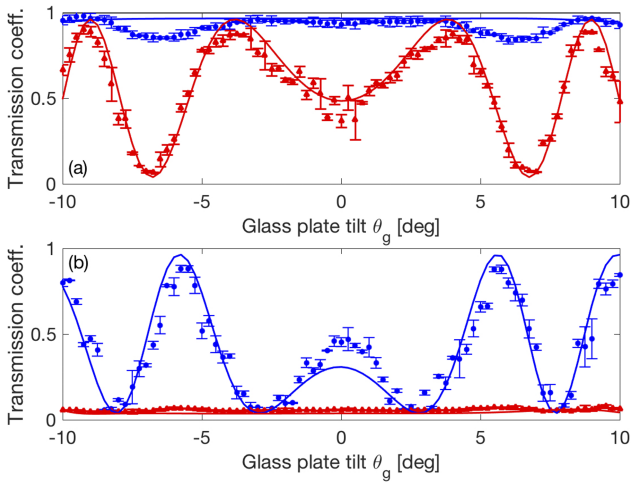

FIG. 5. Transmission coefficients for the horizontal (blue circles) and vertical (red triangles) polarizations in two particular cases: (a) when T_H is maximum and T_V varies, and (b) when T_V is minimum and T_H varies. These two plots, respectively, correspond to the dashed and dotted lines in Fig. 4(a). The solid curves correspond to the theoretical transmission coefficients along the same two lines. In order to be visible, the error bars correspond to three times the standard deviation over the 100 measurements taken for each data point. The noise observed is mainly due to laser instability arising from back reflections.

crystal and glass plate allow a complete and independent control of the T and R coefficients for both polarizations, which is the defining feature of a VPPBS.

The performance of the VPPBS presented here can be quantified in terms of the interferometer visibility for each polarization. On the one hand, the overall visibility for the H polarization [T_H coefficient in Fig. 4(a)] was 93%, while for the V polarization [T_V coefficient in Fig. 4(a)] was 92%. In the particular cases shown in Fig. 5, the T_V [panel (a)] and T_H [panel (b)] coefficients display visibilities of 89% and 86%, respectively. We have investigated and ruled out a number of possible sources for the imperfect visibility, including imbalanced NPBS splitting ratios, fluctuations in the signal, and polarization. This leaves the most likely source to be alignment of the interferometer. In any case, the main impact of imperfect visibility will be to limit the achievable range of the transmission coefficient, as can be seen in Eq. (13). Despite this fact, the Sagnac interferometer remained stable over 12 h without the need for active feedback or constant readjustment, which suggests that the VPPBS could successfully be used as an element in a larger experimental setup.

Lastly, we discuss the theoretical lines in Fig. 5. Qualitatively, the strongly varying transmission coefficients in panels (a) (red curve) and (b) (blue curve) follow the behaviour of the experimental points. However, the transmission coefficients that are meant to be constant do vary unlike their corresponding theoretical curves. Moreover, for all four curves, the discrepancy between theory and experiment is greater than the experimental uncertainty for most data points. Given the low accuracy of the theoretical model and its relative complexity, this discrepancy again confirms that it is better to use the experimental characterization of the VPPBS presented in Fig. 4(a) to determine the correct tilt media angles for a target transmission coefficient.

V. CONCLUSIONS

A variable partially polarizing beam splitter is presented based on a displaced Sagnac interferometer. The transmission and reflection coefficients for the horizontal and vertical polarizations are controlled via the tilts of a birefringent crystal and a glass plate, which introduce a relative phase to each polarization. The overall effect of these two phase retarders is a complete and independent manipulation of the VPPBS splitting ratios for the two polarizations. Since this design includes optical elements that can be found in any optics laboratory, its implementation is straightforward and inexpensive.

ACKNOWLEDGMENTS

This work was supported by the Canada Research Chairs (CRC) Program, the Natural Sciences and Engineering Research Council (NSERC), and the Canada Excellence Research Chairs (CERC) Program. J.F. acknowledges support from COLCIENCIAS.

APPENDIX A: ALTERNATIVE VPPBS CONFIGURATIONS

A VPPBS can also be created using a variation of the Mach-Zehnder interferometer in Fig. 2. As shown in Fig. 6, by replacing the NPBSs by PBSs and implementing the phase retarders via half-wave plates (HWPs), similar expressions for $\mathbf{E}_{\text{out},1}(t)$ and $\mathbf{E}_{\text{out},1}(t)$ in Eqs. (5) and (6) are obtained. Indeed, the interferometer in Fig. 6 has its own displaced Sagnac-interferometer version presented in Refs. 13 and 14, except for the HWP at 45° in one of its outputs. The main reason to implement experimentally the Sagnac interferometer in Fig. 3 instead of the one in Refs. 13 and 14 is that the separation between the counter-propagating paths does not provide enough room to place the HWP rotating mounts at our disposal without blocking one of the beams.

To see explicitly how the Mach-Zehnder interferometer in Fig. 6 works as a VPPBS, consider light entering at input 1 with the electric field $\mathbf{E}_{\text{in}}(t)$ in Eq. (1). After the first PBS, the upper and lower fields read

$$\mathbf{E}_{\text{upper}}(t) = \begin{bmatrix} E_{\text{in}}^{H}(t) \\ 0 \end{bmatrix}, \tag{A1}$$

$$\mathbf{E}_{\text{lower}}(t) = e^{i\frac{\pi}{2}} \begin{bmatrix} 0 \\ E_{\text{in}}^{V}(t) \end{bmatrix}. \tag{A2}$$

After the HWPs with fast axes oriented at θ_H and θ_V in the upper and lower paths, respectively, the electric fields become

$$\tilde{\mathbf{E}}_{\text{upper}}(t) = E_{\text{in}}^{H}(t) \begin{bmatrix} \cos(2\theta_H) \\ \sin(2\theta_H) \end{bmatrix}, \tag{A3}$$

$$\tilde{\mathbf{E}}_{\text{lower}}(t) = e^{i\frac{\pi}{2}} E_{\text{in}}^{V}(t) \begin{bmatrix} \sin(2\theta_V) \\ -\cos(2\theta_V) \end{bmatrix}. \tag{A4}$$

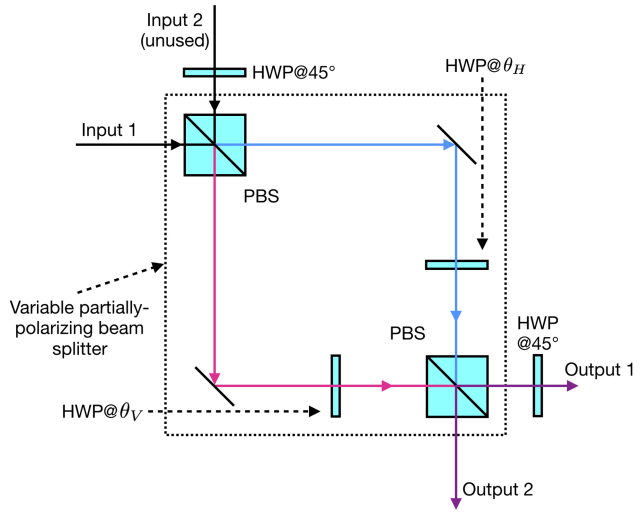

FIG. 6. Variable partially polarizing beam splitter based on a Mach-Zehnder interferometer with polarizing beam splitters (PBSs) instead of non-polarizing beam splitters as in Fig. 2, and half-wave plates (HWPs) as phase retarders. Although input 2 is unused in the current description of the VPPBS, a HWP at 45° must be placed at this input to convert the horizontal polarization at input 2 to vertical so that it travels into the same arm as the horizontal polarization at input 1. Consequently, the two inputs can then be mixed by the HWP in that arm. A similar argument holds for the vertical polarizations at inputs 1 and 2. This HWP at input 2 is necessary when both inputs of the VPPBS are required, as in two-photon quantum logic gate operations.[1–3,15]

Finally, at outputs 1 and 2, including the HWP at 45° in the first one, the electric fields are

$$\mathbf{E}_{\text{out},1}(t) = \begin{bmatrix} E_{\text{in}}^{H}(t)\sin(2\theta_H) \\ \\ E_{\text{in}}^{V}(t)\sin(2\theta_V) \end{bmatrix}, \tag{A5}$$

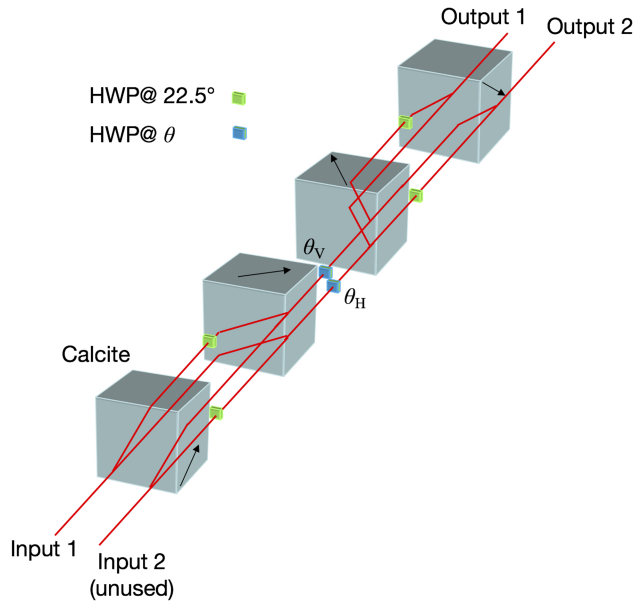

FIG. 7. Alternative VPPBS configuration using PBSs made of birefringent crystals in a linear configuration. The resulting interferometer exhibits phase stability, much like the displaced Sagnac interferometer described in the main part of the paper. The arrow on each walk-off crystal indicates the direction of its optic axis.

$$\mathbf{E}_{\text{out},2}(t) = \begin{bmatrix} E_{\text{in}}^{H}(t)\cos(2\theta_H) \\ \\ E_{\text{in}}^{V}(t)\cos(2\theta_V) \end{bmatrix}. \tag{A6}$$

These expressions are physically identical to Eqs. (5) and (6) and therefore allow the definition of the VPPBS transmission and reflection coefficients as in Eq. (7).

Alternatively, PBSs in Fig. 6 can be implemented using two birefringent walk-off crystals (e.g., calcite) in a linear configuration.[15,16] The VPPBS based on the resulting interferometer is shown in Fig. 7. In this design, the separation between optical paths is small and all paths pass through the same crystals. Consequently, much like the displaced Sagnac interferometer, this linear interferometer exhibits an inherent phase stability.

APPENDIX B: PHASE INTRODUCED BY A TILTED OPTICAL PLATE

In Sec. II, the relative phase ϕ in Eq. (10) is obtained as follows. Consider an optical medium of thickness d and refractive index n that is tilted by an angle θ, as shown in Fig. 8. As mentioned in Sec. II, when the optical medium is perpendicular to the input beam, the relative phase between the optical paths in a Mach-Zehnder interferometer is given by

$$\phi = \frac{2\pi d}{\lambda}(n - n_a), \tag{B1}$$

with λ the light wavelength and n_a the refractive index of air. When the optical medium is tilted, the relative phase between the two optical paths corresponds to

$$\phi = \frac{2\pi \ell}{\lambda}n - \frac{2\pi(d+\delta)}{\lambda}n_a, \tag{B2}$$

where ℓ is the length that light travels through the optical medium, and δ is a small length that, together with d, defines the longitudinal component of ℓ. One can understand Eq. (B2) considering two optical media, the first one of thickness ℓ and refractive index n in one arm of the interferometer and the second one of thickness $d + \delta$ and refractive index n_a ("made" of air) in the other arm.

According to Fig. 8, ℓ is equal to

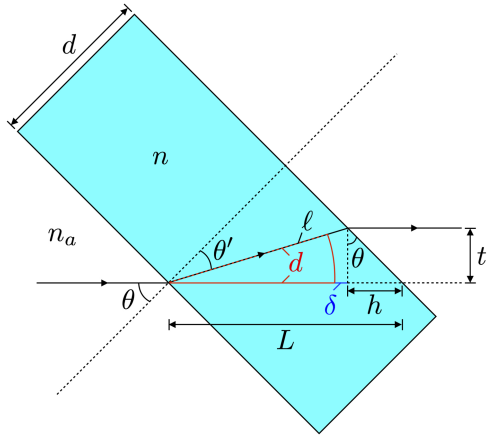

FIG. 8. Optical medium of thickness d and refractive index n tilted by an angle θ. Such an angle has been exaggerated to introduce all the important quantities in the calculation of the relative phase ϕ in Eq. (10).

$$\ell = \frac{d}{\cos\theta'}, \tag{B3}$$

where θ' is the angle of refraction given by Snell's law in Eq. (11). In terms of ℓ, the transverse separation t between the input and output beams is equal to

$$t = \ell \sin(\theta - \theta') = \frac{d}{\cos\theta'} \sin(\theta - \theta'), \tag{B4}$$

allowing us to find an expression for h in Fig. 8,

$$h = t \tan\theta = \frac{d}{\cos\theta'} \sin(\theta - \theta') \tan\theta. \tag{B5}$$

On the other hand, the quantity L, defined as the total length that light would travel through if there were no optical medium, is

$$L = \frac{d}{\cos\theta}. \tag{B6}$$

However, according to Fig. 8, $d + \delta$ is equal to $L - h$. Thus the relative phase in Eq. (B2) becomes

$$\phi = \frac{2\pi\ell}{\lambda} n - \frac{2\pi(L-h)}{\lambda} n_a. \tag{B7}$$

Substituting Eqs. (B3), (B5), and (B6) into the last expression, ϕ reduces to

$$\phi = \frac{2\pi d}{\lambda} \times \left[\frac{n}{\cos\theta'} - n_a \left(\frac{1}{\cos\theta} - \frac{\sin(\theta - \theta')\tan\theta}{\cos\theta'} \right) \right], \tag{B8}$$

which can be simplified to finally obtain Eq. (10) in Sec. II,

$$\phi = \frac{2\pi d}{\lambda} \left[\frac{n}{\cos\theta'} - n_a \left(\cos\theta + \sin\theta \tan\theta' \right) \right]. \tag{B9}$$

[1] N. Kiesel, C. Schmid, U. Weber, R. Ursin, and H. Weinfurter, "Linear optics controlled-phase gate made simple," Phys. Rev. Lett. **95**, 210505 (2005).

[2] R. Okamoto, H. F. Hofmann, S. Takeuchi, and K. Sasaki, "Demonstration of an optical quantum controlled-not gate without path interference," Phys. Rev. Lett. **95**, 210506 (2005).

[3] N. K. Langford, T. J. Weinhold, R. Prevedel, K. J. Resch, A. Gilchrist, J. L. O'Brien, G. J. Pryde, and A. G. White, "Demonstration of a simple entangling optical gate and its use in Bell-state analysis," Phys. Rev. Lett. **95**, 210504 (2005).

[4] A. Ling, K. P. Soh, A. Lamas-Linares, and C. Kurtsiefer, "Experimental polarization state tomography using optimal polarimeters," Phys. Rev. A **74**, 022309 (2006).

[5] Z. E. D. Medendorp, F. A. Torres-Ruiz, L. K. Shalm, G. N. M. Tabia, C. A. Fuchs, and A. M. Steinberg, "Experimental characterization of qutrits using symmetric informationally complete positive operator-valued measurements," Phys. Rev. A **83**, 051801 (2011).

[6] F. Kaiser, T. Coudreau, P. Milman, D. B. Ostrowsky, and S. Tanzilli, "Entanglement-enabled delayed-choice experiment," Science **338**, 637 (2012).

[7] R. W. Boyd, *Nonlinear Optics*, 3rd ed. (Academic Press, 2008).

[8] T. Nagata, R. Okamoto, J. L. O'Brien, K. Sasaki, and S. Takeuchi, "Beating the standard quantum limit with four-entangled photons," Science **316**, 726 (2007).

[9] M. Mičuda, E. Doláková, I. Straka, M. Miková, M. Dušek, J. Fiurášek, and M. Ježek, "Highly stable polarization independent Mach-Zehnder interferometer," Rev. Sci. Instrum. **85**, 083103 (2014).

[10] J. M. Ashby, P. D. Schwarz, and M. Schlosshauer, "Observation of the quantum paradox of separation of a single photon from one of its properties," Phys. Rev. A **94**, 012102 (2016).

[11] Schott, Optical glass data sheets, 2015.

[12] K. Kato, "Second-harmonic generation to 2048 A in beta-BaB_2O_4," IEEE J. Quantum Electron. **QE-22**, 1013 (1986).

[13] Y.-C. Jeong, J.-C. Lee, and Y.-H. Kim, "Experimental implementation of a fully controllable depolarizing quantum operation," Phys. Rev. A **87**, 014301 (2013).

[14] A. Cuevas, M. Proietti, M. A. Ciampini, S. Duranti, P. Mataloni, M. F. Sacchi, and C. Macchiavello, "Experimental detection of quantum channel capacities," Phys. Rev. Lett. **119**, 100502 (2017).

[15] J. L. O'Brien, G. J. Pryde, A. G. White, T. C. Ralph, and D. Branning, "Demonstration of an all-optical quantum controlled-not gate," Nature **426**, 264 (2003).

[16] P. G. Evans, R. S. Bennink, W. P. Grice, T. S. Humble, and J. Schaake, "Bright source of spectrally uncorrelated polarization-entangled photons with nearly single-mode emission," Phys. Rev. Lett. **105**, 253601 (2010).

Appendix D

Parametric down-conversion angular spectrum

In this appendix we calculate the emission angles for the signal and idler wavelengths when there is imperfect phase-matching in the component of $\Delta\mathbf{k}$ parallel to the collinear direction. Let us assume that the pump field propagates in the perpendicular direction to the PPLN optic axes, as illustrated in Fig. 4.2(a), and allow the signal and idler fields to be emitted at respective angles θ_1 and θ_2, defined from the collinear direction. This second assumption is in contrast to what we assumed in Eq. (4.1), where both θ_1 and θ_2 vanished. Then, the component of $\Delta\mathbf{k} = \mathbf{k}_1 + \mathbf{k}_2 - \mathbf{k}_3 + \mathbf{K}$ perpendicular to the collinear direction reads

$$\Delta k_\perp = k_1 \sin\theta_1 - k_2 \sin\theta_2,$$

with $k_j = 2\pi n_e(\lambda_j, T)/\lambda_j$, $j = 1, 2, 3$, and $n_e(\lambda_j, T)$ the extraordinary refractive index given by O. Gayer et al. for 5% MgO doped lithium niobate [Gay+08]. Assuming perfect phase-matching in the perpendicular plane to the collinear direction, i.e. $\Delta k_\perp = 0$, we can express θ_2 in terms of θ_1,

$$\theta_2 = \arcsin\left(\frac{k_1}{k_2}\sin\theta_1\right), \tag{D.1}$$

and substitute θ_2 in the component of the wave vector mismatch $\Delta\mathbf{k}$ parallel to the collinear direction,

$$\Delta k_\parallel = k_1 \cos\theta_1 + k_2 \cos\theta_2 - k_3 + K.$$

Here, $K = 2\pi/\Lambda$ is the grating wave vector magnitude, with Λ the grating period. The resulting expression for $\Delta k_\parallel$ is

$$\Delta k_\parallel = \frac{2\pi n_e(\lambda_1, T)}{\lambda_1}\cos\theta_1 + \frac{2\pi n_e(\lambda_2, T)}{\lambda_2}\cos\left[\arcsin\left(\frac{n_e(\lambda_1, T)\lambda_2}{n_e(\lambda_2, T)\lambda_1}\sin\theta_1\right)\right] - \frac{2\pi n_e(\lambda_3, T)}{\lambda_3} + \frac{2\pi}{\Lambda}.$$

Finally, λ_2 can be expressed in terms of λ_1 and λ_3, according to Eq. (4.2). After this substitution, $\Delta k_\parallel$ can be replaced in the PDC angular spectrum, which is proportional to the squared

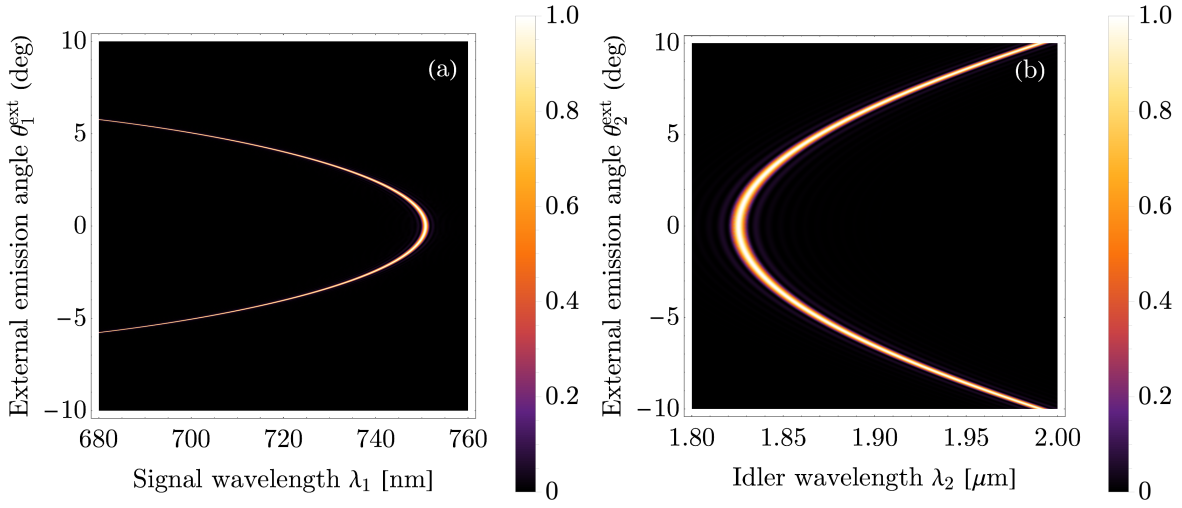

FIGURE D.1: Angular spectrum for the signal (a) and idler (b) fields generated via parametric down-conversion. To obtain these spectra, we use $\lambda_3 = 532$ nm, $T = 22$ °C, $\Lambda = 8.12$ μm, and $L = 5$ mm.

sine cardinal function of the product $\Delta k_{\parallel} L$ [BH68; Kly88],

$$S(\lambda_1, \theta_1) \propto \text{sinc}^2\left(\frac{\Delta k_{\parallel} L}{2}\right),$$

with L the crystal length. The resulting angular spectrum for the signal field is shown in Fig. D.1(a). By repeating the same steps, but now solving for θ_2 and λ_2 in Eqs. (D.1) and (4.2), or what is the same, by switching the labels 1 and 2 in all the expressions in this appendix, we obtain the angular spectrum for the idler field shown in Fig. D.1(b). We make an additional substitution to express the internal emission angles θ_1 and θ_2 in terms of the external angles θ_1^{ext} and θ_2^{ext} via Snell's law,

$$\theta_j = \arcsin\left(\frac{\sin\theta_j^{\text{ext}}}{n_e(\lambda_j, T)}\right),$$

with $j = 1, 2$ in this particular expression. Therefore, the final angular spectra in Fig. D.1 are in terms of θ_j^{ext} instead of θ_j.

According to Fig. D.1, the signal and idler fields are mostly emitted in the collinear direction, i.e. $\theta_1^{\text{ext}} = 0 = \theta_2^{\text{ext}}$, with wavelengths $\lambda_1 = 751$ nm and $\lambda_2 = 1.83$ μm, as already mentioned in Chapter 4. However, the phase-matching conditions allow PDC at different external emission angles in the intervals $(-6°, 6°)$ and $(-10°, 10°)$ for the signal and idler fields, respectively, although with less probability than in the collinear direction. Interestingly, the PDC spectra are quite broad, ranging from a few tens of nanometers for the signal field up to a few hundreds of nanometers for the idler.

Appendix E

Making our laser pulses Fourier transform limited

As discussed in Chapter. 5, one possible limitation in our BHD setup is the non-Fourier transform-limited pulses produced by our laser source. This limitation may explain the excess noise in the X_θ variance around $\theta = \pi/2$ and $3\pi/2$ for a coherent state in e.g. Fig. 5.7. Hence, we study in this appendix a couple of strategies to spectrally filter our laser so that its coherence time (~ 5 ps) is comparable to the pulse duration (~ 18 ps). We could also engineer our laser to reduce the pulse duration down to the coherence time, but we do not consider this solution here because it requires to access the laser enclosure box. In this regard, the laser company (EKSPLA) explained that the Kerr effect broadens the spectrum in the regenerative amplifier and that a BBO crystal can compensate for this effect. However, introducing such a crystal in the regenerative amplification cavity is a demanding procedure that the company engineers must execute. Moreover, once the BBO crystal is introduced, the temporal/spectral properties of the laser change, affecting other experiments that use the same laser source.

Ideally, placing a narrow bandpass filter at the laser output can increase the pulse coherence time without broadening the pulse duration. In frequency terms, we require a bandpass filter with a spectral bandwidth $\Delta\nu$ equal to $1/\tau'$, where $\tau' = 18$ ps is the coherence time we want to achieve. From the relation $\nu = c/\lambda$, with $\lambda = 532$ nm the central laser wavelength, we get a filter bandwidth in wavelength terms equal to

$$\Delta\lambda = \frac{\lambda^2}{c}\Delta\nu = \frac{\lambda^2}{c\tau'} = 0.05 \text{ nm}.$$

This bandwidth is four times less than the pulse spectral width (~ 0.2 nm) and thus relatively narrow to achieve via an interference bandpass filter or a monochromator. For example, commercially available ultra-narrow bandpass filters at 532 nm provide bandwidths of 0.2 nm and above. Moreover, their spectral peak-to-peak separation, also known as the free spectral range, must be larger than the pulse spectral width. In the case of a monochromator, the narrowest bandwidth provided by the one at our disposal (Horiba TRIAX 190) was 0.15 nm. Therefore, our first strategy to spectrally filter our laser is based on a Fabry-Pérot etalon,

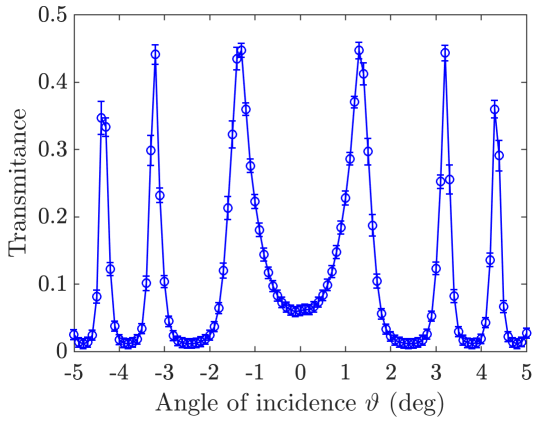

FIGURE E.1: Fabry-Pérot etalon transmittance as a function of the laser beam angle of incidence ϑ. The error bars were multiplied by a factor of 5 for improved visibility. A 0° angle of incidence means normal incidence.

which can reach the desired bandwidth by proper design.

A Fabry-Pérot etalon is made of two parallel partially reflective surfaces separated by a material of thickness l [FP99]. Depending on the surface reflectance, the material in between and its thickness, a Fabry-Pérot etalon defines a set of transmission peaks with specific bandwidth and free spectral range [Hec17]. The ratio between the free spectral range and the bandwidth is the etalon finesse in wavelength terms. The etalon displays sharper peaks and lower transmission minima if the finesse is high than a low-finesse etalon. The transmission peaks are observed when the rays undergoing multiple reflections within the two partially reflective surfaces interfere constructively. In particular, the maximum of a transmission peak is observed when the phase difference δ between these rays satisfies [Hec17]

$$\delta = \frac{2\pi}{\lambda} 2nl \cos \vartheta',$$

where n is the etalon material refractive index, and $\vartheta' = \arcsin(\sin\vartheta/n)$ is the refraction angle inside the material, with ϑ the incidence angle. For a given λ, n and l, we get several transmission peaks by tuning ϑ due to a change in the effective path travelled by the rays inside the etalon.

After an online search, we found an off-the-shelf Fabry-Pérot etalon (LightMachinery) that roughly met our requirements. This etalon is based on a fused silica substrate of thickness $l =$ 0.3 mm with 82% reflectance surfaces deposited on top and bottom ends. These construction parameters provide a peak bandwidth of 0.02 nm, a free spectral range equal to 0.32 nm and a finesse of 16. These nominal values were calculated using an online etalon design tool offered by the manufacturing company [Lig]. Although the resulting peak bandwidth is narrower than required, we still tested it to witness any impact on the X_θ variance. Using the laser in

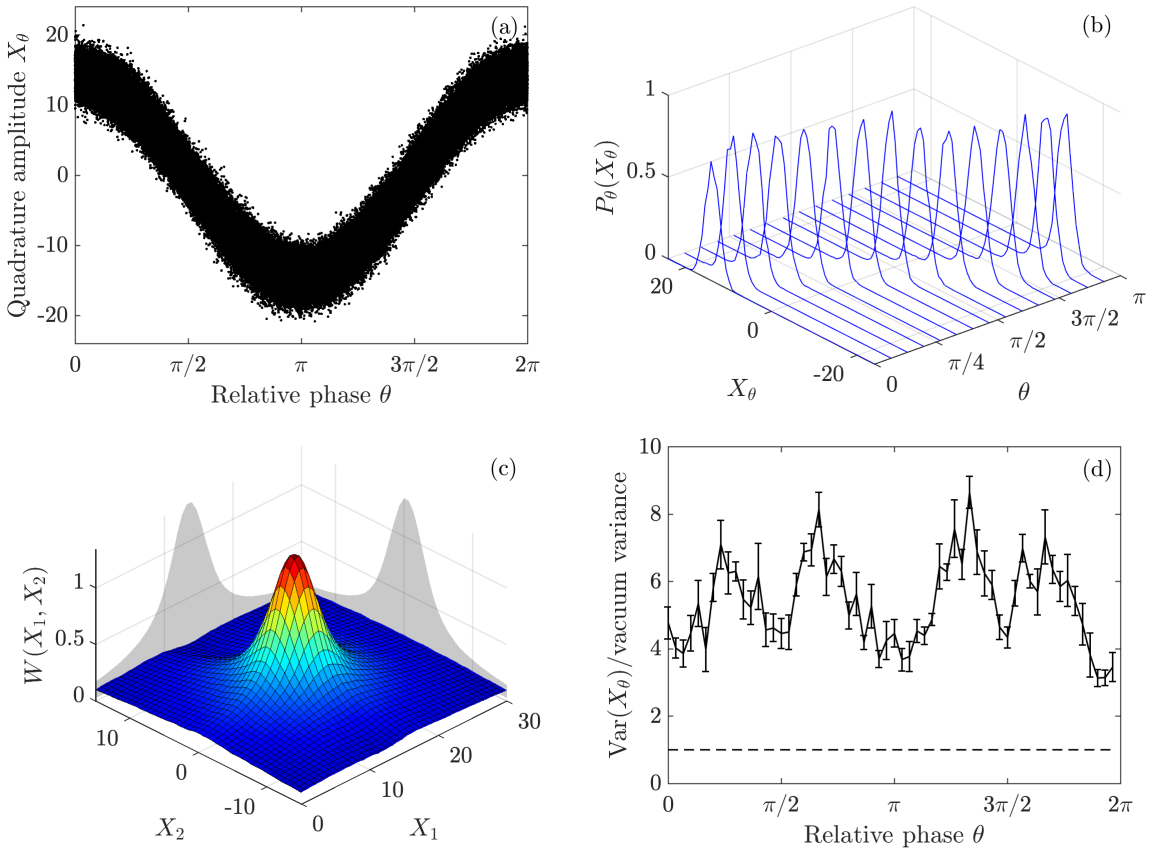

FIGURE E.2: Time-domain balanced homodyne detection of the spectrally filtered laser field with $\sim$ 200 photons per pulse on average. In panel (a), we have $\sim 3 \times 10^5$ single-shot data points of the quadrature amplitude X_θ as a function of the relative phase θ. In panel (b), we plot the marginal distributions $P_\theta(X_\theta)$ required to reconstruct the Wigner function via the inverse Radon transform, which is shown in panel (c). Only half of these marginal distributions are plotted in the $0 \leq \theta < \pi$ range for visualization reasons. In panel (d), we have the quadrature X_θ variance after subtracting the electronic noise variance according to Eq. (5.8). The error bars were multiplied by a factor of 5 for improved visibility. The horizontal (black dashed) line indicates the vacuum state variance.

Fig. 5.3 as the light source, the measured transmittance of the Fabry-Pérot etalon described above is shown in Fig. E.1 as a function of ϑ. Based on this plot, we set ϑ such that the etalon transmittance is maximized ($\vartheta \approx 1.3°$), and perform time-domain BHD on a laser field with $\sim$ 200 photons per pulse by following the same steps to characterize the laser field in Fig. 5.7. The experimental results are shown in Fig. E.2.

In general terms, the results in Fig. E.2 look very similar to those in Fig. 5.7, so most of the analysis from the latter applies to the former. However, the X_θ variance displays new features. On the one hand, the lowest X_θ variance obtained is four times the value expected

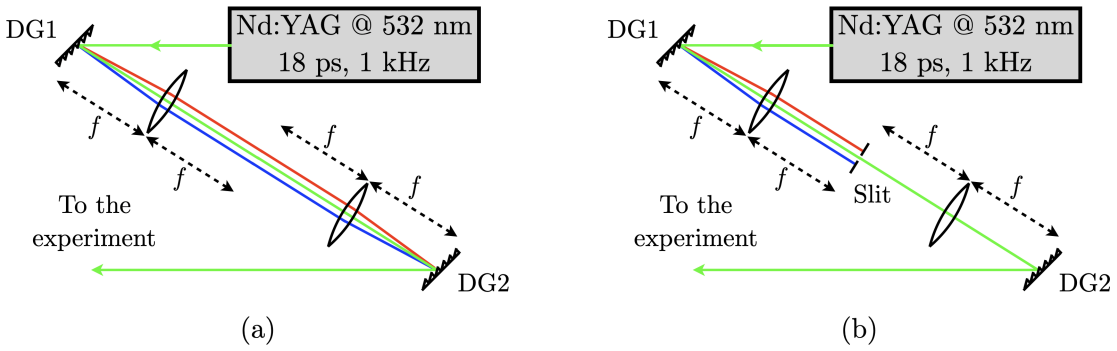

FIGURE E.3: Spectral filtering implemented via diffraction gratings to make our laser pulses Fourier transform-limited. In panel (a), two identical diffraction gratings, DG1 and DG2, and two identical positive lenses of focal length f form a $4f$ system, with DG2 reversing the effect of DG1. We present this configuration to illustrate how DG2 collimates the laser beam and removes any chirp introduced by DG1 when the actual filtering occurs. In panel (b), a narrow slit is placed in the middle of the $4f$ system to remove the unwanted wavelength components.

for a coherent state. The reason for this overall noise may be the high number of photons per pulse in the laser field (~ 200), which is twice the one sampled in Fig. 5.7. It would be worth studying a new light field with ~ 100 photons per pulse on average to tell whether this overall noise vanishes or comes from the Fabry-Pérot etalon implementation. On the other hand, the X_θ variance at $\theta = \pi/2$ and $3\pi/2$ is now at the same level as the one at $\theta = 0$, π and 2π, meaning that there is a noise reduction thanks to the introduction of the Fabry-Pérot etalon. Unfortunately, new excess noise appears at odd multiples of $\theta = \pi/4$.

One drawback of Fabry-Pérot etalons is that they must be carefully designed and fabricated for each particular application, which makes them expensive and not readily available. Moreover, any fine tuning during its actual implementation, like the peak bandwidth in our case, is forbidden. Therefore, we consider a more versatile spectral filtering strategy to make our pulses Fourier transform limited. This second strategy is based on a diffraction grating (DG1) that diffracts light at different angles depending on its wavelength [Hec17], as shown in Fig. E.3. Then, a $2f$ system plus a narrow slit remove the unwanted wavelength components at the Fourier plane. In particular, a slit of width $s = 100$ μm in combination with a positive lens of focal length $f = 1.0$ m and a 1800 grooves/mm diffraction grating, allows light of wavelength $\lambda = 532$ nm to pass through with a bandwidth $\Delta\lambda$ equal to [Hec17]

$$\Delta\lambda = \frac{as}{|m|f}\cos\theta_m = 0.054 \text{ nm}, \tag{E.1}$$

as required for our purposes. In Eq. (E.1), $m = -1$ is the diffraction order, $a = (1800)^{-1}$ mm

is the grating line size, and $\theta_{m=-1} = -14.5°$ is the diffraction angle obtained from the expression [Hec17]

$$m\lambda = a\left(\sin\theta_m - \sin\theta_i\right), \tag{E.2}$$

assuming an incident angle of $\theta_i = 45°$. Diffraction orders $m = +1, \pm 2, \pm 3, \ldots$ are forbidden by Eq. (E.2), i.e. they lead to a complex θ_m. Moreover, to achieve the desired spectral resolution, a total number $N = \lambda/\Delta\lambda$ of grating lines must be illuminated by the laser beam. To achieve this N, the beam must be $Na \approx 6$ mm in diameter at DG1 [Hec17]. After the slit, an identical $2f$ system and diffraction grating, DG2 in Fig. E.3, collimate the laser beam and remove any chirp by reversing the effect of DG1 on the laser pulses. An illustration of this reversal process is depicted in Fig. E.3(a), while the actual spectral filtering with the slit in place is shown in panel (b).

Preliminary results have shown a three times increase in the coherence time of the laser source by only using DG1 and the described slit. Once we remove the excess noise in the X_θ variance for a coherent state, we will submit our results on the Wigner function of the pump field for publication.

List of Figures

1.1 von Neumann entropy and number of photons in the signal mode of an optical parametric amplifier operating in the spontaneous case 10
1.2 Black hole von Neumann entropy from the one-shot decoupling method 14
1.3 Mean number of pump and signal photons resulting from the trilinear Hamiltonian 18

2.1 Schematic of difference-frequency generation 24
2.2 Classical vs quantum number of pump and signal photons from the optical parametric amplifier 31
2.3 Classical vs quantum number of pump and signal photons for difference-frequency generation 32
2.4 (a) Conversion efficiency of an optical parametric amplifier at the first turning point in the number of photons according to the quantum model; (b) classical number of photons in a realistic experimental scenario 33

3.1 Linear and nonlinear interferometer in a Mach-Zehnder configuration 37
3.2 Interference pattern of a three-mode nonlinear interferometer 42
3.3 Phase sensitivity of a three-mode nonlinear interferometer as a function of the relative phase 43
3.4 Phase sensitivity of a three-mode nonlinear interferometer as a function of the parametric gain in the interferometer OPAs 44
3.5 Optimal phase sensitivities as a function of the initial number of pump photons 45
3.6 Photon number probability distribution inside the nonlinear interferometer optical parametric amplifier A 47

4.1 Experimental setup to observe type-0 high-gain parametric down-conversion with a dynamic pump field 51
4.2 Periodically-poled lithium niobate crystal and tuning curves 53
4.3 Experimental number of photons from parametric down-conversion in the high-gain regime with pump depletion 55
4.4 Photon number probability distribution for the pump field, and second-order correlation function for the pump and signal fields 58

5.1 Wigner function of a coherent, vacuum and a thermal state 65

5.2 Balanced homodyne detection scheme 68
5.3 Experimental setup to balanced homodyne the pump field after a PDC process with pump depletion 69
5.4 Balanced detector used in homodyne detection 71
5.5 Temporal response of the balanced detector 72
5.6 Photocurrent difference and its variance as a function of the LO intensity. . . . 74
5.7 Time-domain balanced homodyne detection of the laser field with ~ 100 photons per pulse on average 75
5.8 Quadrature amplitude X_θ of the pump field after a parametric down-conversion process with different input pump powers 78
5.9 Quadrature X_θ variance of the pump field after a parametric down-conversion process with different input pump powers 79

A.1 Black hole purity from the one-shot decoupling method 86

B.1 Computation time to numerically solve the trilinear Hamiltonian 91

D.1 Parametric down-conversion angular spectrum 102

E.1 Fabry-Pérot etalon transmittance as a function of the laser beam angle of incidence 104
E.2 Time-domain balanced homodyne detection of the spectrally filtered laser field with ~ 200 photons per pulse on average 105
E.3 Spectral filtering implemented via diffraction gratings to make our laser pulses Fourier transform limited 106

List of Tables

1.1 Some phenomena described by the trilinear Hamiltonian with the role played by each bosonic mode 15

3.1 Fitting parameters for the first optimal phase sensitivity of a three-mode nonlinear interferometer 46

B.1 Sixth-order polynomial fitting parameters for the computation time to numerically solve the trilinear Hamiltonian 91

List of Abbreviations

AdS	**A**nti-**d**e **S**itter space
BBO	β-**B**arium **B**orate
BHD	**B**alanced **H**omodyne **D**etection
BP	**B**and-**P**ass (filter)
BS	**B**eam **S**plitter
CFT	**C**onformal **F**ield **T**heory
CG	**C**olor **G**lass (filter)
DG	**D**iffraction **G**rating
DM	**D**ichroic **M**irror
G-T	**G**lan-**T**hompson (prism)
HR	**H**awking **R**adiation
HWP	**H**alf-**W**ave **P**late
KTP	**P**otassium **T**itanyl **P**hosphate
LO	**L**ocal **O**scillator
ND	**N**eutral **D**ensity (filter)
Nd:YAG	**N**eodymium-**d**oped **Y**ttrium **A**luminium **G**arnet (laser)

OPA **O**ptical **P**arametric **A**mplifier

PA **P**arametric **A**pproximation

PBS **P**olarizing **B**eam **S**plitter

Pd **P**hoto**d**etector

PDC **P**arametric-**D**own **C**onversion

PPLN **P**eriodically-**P**oled **L**ithium **N**iobate (crystal)

QuTiP **Qu**antum **T**oolbox **i**n **P**ython

Bibliography

[AB14] A. Allevi and M. Bondani. "Statistics of twin-beam states by photon-number resolving detectors up to pump depletion". In: *Journal of the Optical Society of America B* 31 (2014), B14. DOI: 10.1364/JOSAB.31.000B14.

[Ace+19] F. Acernese et al. "Increasing the Astrophysical Reach of the Advanced Virgo Detector via the Application of Squeezed Vacuum States of Light". In: *Physics Review Letters* 123 (2019), p. 231108. DOI: 10.1103/PhysRevLett.123.231108.

[AF16] P.M. Alsing and M.L. Fanto. "A discrete analogue for black hole evaporation using approximate analytical solutions of a one-shot decoupling trilinear Hamiltonian". In: *Classical and Quantum Gravity* 33 (2016), p. 015005. DOI: 10.1088/0264-9381/33/1/015005.

[All+14] A. Allevi, O. Jedrkiewicz, E. Brambilla, A. Gatti, J. Peřina, O. Haderka, and M. Bondani. "Coherence properties of high-gain twin beams". In: *Physical Review A* 90 (2014), p. 063812. DOI: 10.1103/PhysRevA.90.063812.

[Alm+19] A. Almheiri, N. Engelhardt, D. Marolf, and H. Maxfield. "The entropy of bulk quantum fields and the entanglement wedge of an evaporating black hole". In: *Journal of High Energy Physics* 2019 (2019), p. 63. DOI: 10.1007/JHEP12(2019)063.

[Alm+20a] A. Almheiri, T. Hartman, J. Maldacena, E. Shaghoulian, and A. Tajdini. "Replica wormholes and the entropy of Hawking radiation". In: *Journal of High Energy Physics* 2020 (2020). DOI: 10.1007/JHEP05(2020)013.

[Alm+20b] A. Almheiri, R. Mahajan, J. Maldacena, and Y. Zhao. "The Page curve of Hawking radiation from semiclassical geometry". In: *Journal of High Energy Physics* 2020 (2020), p. 149. DOI: 10.1007/JHEP03(2020)149.

[Als15] P.M. Alsing. "Parametric down conversion with a depleted pump as a model for classical information transmission capacity of quantum black holes". In: *Classical and Quantum Gravity* 32 (2015), p. 075010. DOI: 10.1088/0264-9381/32/7/075010.

[And+95] M.E. Anderson, M. Beck, M.G. Raymer, and J.D. Bierlein. "Quadrature squeezing with ultrashort pulses in nonlinear-optical waveguides". In: *Optics Letters* 20 (1995), p. 620. DOI: 10.1364/OL.20.000620.

[Arm+62] J.A. Armstrong, N. Bloembergen, J. Ducuing, and P.S. Pershan. "Interactions between Light Waves in a Nonlinear Dielectric". In: *Physical Review* 127 (1962), p. 1918. DOI: 10.1103/PhysRev.127.1918.

[A.S+20] Ashik A.S., P. Tidemand-Lichtenberg, O. Rodenko, and C. Pedersen. "Pulse-to-pulse spectral noise in a spontaneous parametric down conversion light source". In: *Optics Letters* 45 (2020), p. 2772. DOI: 10.1364/OL.392067.

[BA16] K. Brádler and C. Adami. "One-Shot Decoupling and Page Curves from a Dynamical Model for Black Hole Evaporation". In: *Physical Review Letters* 116 (2016), p. 101301. DOI: 10.1103/PhysRevLett.116.101301.

[Ban+99] K. Banaszek, G.M. D'Ariano, M.G.A. Paris, and M.F. Sacchi. "Maximum-likelihood estimation of the density matrix". In: *Physical Review A* 61 (1999), p. 010304. DOI: 10.1103/PhysRevA.61.010304.

[Bas79] M.J. Bastiaans. "Wigner distribution function and its application to first-order optics". In: *Journal of the Optical Society of America* 69 (1979), p. 1710. DOI: 10.1364/JOSA.69.001710.

[BC09] S.M. Barnett and S. Croke. "Quantum state discrimination". In: *Advances in Optics and Photonics* 1 (2009), p. 238. DOI: 10.1364/AOP.1.000238.

[Bel+10] F. Belgiorno, S.L. Cacciatori, M. Clerici, V. Gorini, G. Ortenzi, L. Rizzi, E. Rubino, V.G. Sala, and D. Faccio. "Hawking Radiation from Ultrashort Laser Pulse Filaments". In: *Physics Review Letters* 105 (2010), p. 203901. DOI: 10.1103/PhysRevLett.105.203901.

[Ben+04] R.S. Bennink, S.J. Bentley, R.W. Boyd, and J.C. Howell. "Quantum and Classical Coincidence Imaging". In: *Physical Review Letters* 92 (2004). DOI: 10.1103/physrevlett.92.033601.

[Ber+02] P. Bertet, A. Auffeves, P. Maioli, S. Osnaghi, T. Meunier, M. Brune, J.M. Raimond, and S. Haroche. "Direct Measurement of the Wigner Function of a One-Photon Fock State in a Cavity". In: *Physical Review Letters* 89 (2002), p. 200402. DOI: 10.1103/PhysRevLett.89.200402.

[Ber77] M.V. Berry. "Semi-classical mechanics in phase space: A study of Wigner's function". In: *Philosophical Transactions of the Royal Society of London. Series A, Mathematical and Physical Sciences* 287 (1977), p. 237. DOI: http://doi.org/10.1098/rsta.1977.0145.

[BGRB10] G. Brida, M. Genovese, and I. Ruo Berchera. "Experimental realization of sub-shot-noise quantum imaging". In: *Nature Photonics* 4 (2010), p. 227. DOI: 10.1038/nphoton.2010.29.

[BGT84] D.A. Bryan, R. Gerson, and H.E. Tomaschke. "Increased optical damage resistance in lithium niobate". In: *Applied Physics Letters* 44 (1984), p. 847. DOI: 10.1063/1.94946.

[BH68] R.L. Byer and S.E. Harris. "Power and Bandwidth of Spontaneous Parametric Emission". In: *Physical Review* 168 (1968), p. 1064. DOI: 10.1103/PhysRev.168.1064.

[BHS18] L. Barsotti, J. Harms, and R. Schnabel. "Squeezed vacuum states of light for gravitational wave detectors". In: *Reports on Progress in Physics* 82 (2018), p. 016905. DOI: 10.1088/1361-6633/aab906.

[BL+14] G. Barreto-Lemos, V. Borish, G.D. Cole, S. Ramelow, R. Lapkiewicz, and A. Zeilinger. "Quantum imaging with undetected photons". In: *Nature* 512 (2014), p. 409. DOI: 10.1038/nature13586.

[Blo65] N. Bloembergen. *Nonlinear Optics*. 1st ed. W. A. Benjamin, INC., 1965.

[Bog58] N.N. Bogoljubov. "On a new method in the theory of superconductivity". In: *Il Nuovo Cimento* 7 (1958), p. 794. DOI: 10.1007/bf02745585.

[Bol72] C.T. Bolton. "Identification of Cygnus X-1 with HDE 226868". In: *Nature* 235 (1972), p. 271. DOI: 10.1038/235271b0.

[Bon+09] M. Bondani, A. Allevi, A. Agliati, and A. Andreoni. "Self-consistent characterization of light statistics". In: *Journal of Modern Optics* 56 (2009), p. 226. DOI: 10.1080/09500340802357307.

[Bos+96] W.R. Bosenberg, A. Drobshoff, J.I. Alexander, L.E. Myers, and R.L. Byer. "93% pump depletion, 3.5-W continuous-wave, singly resonant optical parametric oscillator". In: *Optics Letters* 21 (1996), p. 1336. DOI: 10.1364/OL.21.001336.

[Bow+65] S. Bowyer, E.T. Byram, T.A. Chubb, and H. Friedman. "Cosmic X-ray Sources". In: *Science* 147 (1965), p. 394. DOI: 10.1126/science.147.3656.394.

[Boy08] R.W. Boyd. *Nonlinear Optics*. 3rd ed. Academic Press, 2008. ISBN: 9780080485966.

[Boy19] R.W. Boyd. "Quantum Imaging". In: *Foundations of Quantum Theory*. Volume 197: Proceedings of the International School of Physics "Enrico Fermi". IOS Press, 2019, p. 285. DOI: 10.3254/978-1-61499-937-9-285.

[BP70] R. Bonifacio and G. Preparata. "Coherent Spontaneous Emission". In: *Physical Review A* 2 (1970), p. 336. DOI: 10.1103/PhysRevA.2.336.

[BS97] G. Breitenbach and S. Schiller. "Homodyne tomography of classical and nonclassical light". In: *Journal of Modern Optics* 44 (1997), p. 2207. DOI: 10.1080/09500349708231879.

[BSM97] G. Breitenbach, S. Schiller, and J. Mlynek. "Measurement of the quantum states of squeezed light". In: *Nature* 387 (1997), p. 471. DOI: 10.1038/387471a0.

[BW96] K. Banaszek and K. Wódkiewicz. "Direct Probing of Quantum Phase Space by Photon Counting". In: *Physical Review Letters* 76 (1996), p. 4344. DOI: 10.1103/PhysRevLett.76.4344.

[Car73] B. Carter. "Properties of the Kerr metric". In: *Black Holes. Proceedings of 1972 session of Ecole d'été de pysique theorique*. Ed. by C. DeWitt and B.S. DeWitt. Gordon and Breach, 1973. ISBN: 0677156103.

[Cas+07] K.N. Cassemiro, A.S. Villar, M. Martinelli, and P. Nussenzveig. "The quest for three-color entanglement: experimental investigation of new multipartite quantum correlations". In: *Optics Express* 15 (2007), p. 18236. DOI: 10.1364/OE.15.018236.

[Cav+16] A. Cavanna, F. Just, P.R. Sharapova, M.T., G. Leuchs, and M.V. Chekhova. "Tunable optical parametric generator based on the pump spatial walk-off". In: *Optics Letters* 41 (2016), p. 646. DOI: 10.1364/OL.41.000646.

[Cav81] C.M. Caves. "Quantum-mechanical noise in an interferometer". In: *Physical Review D* 23 (1981), p. 1693. DOI: 10.1103/PhysRevD.23.1693.

[CC16] LIGO Scientific Collaboration and Virgo Collaboration. "Observation of Gravitational Waves from a Binary Black Hole Merger". In: *Physical Review Letters* 116 (2016), p. 061102. DOI: 10.1103/PhysRevLett.116.061102.

[CO16] M.V. Chekhova and Z.Y. Ou. "Nonlinear interferometers in quantum optics". In: *Advances in Optics and Photonics* 8 (2016), p. 104. DOI: 10.1364/AOP.8.000104.

[Col19] The Event Horizon Telescope Collaboration. "First M87 Event Horizon Telescope Results. I. the Shadow of the Supermassive Black Hole". In: *The Astrophysical Journal Letters* 875 (2019). DOI: 10.3847/2041-8213/ab0ec7.

[Cor97] J.F. Cornwell. *Group Theory in Physics: An Introduction*. ISSN. Academic Press, 1997. ISBN: 0121898008.

[Cra46] H. Cramér. *Mathematical Methods of Statistics (PMS-9)*. Princeton University Press, 1946. DOI: 10.1515/9781400883868.

[DB94] G. Drobný and V. Bužek. "Fundamental limit on energy transfer in k-photon down-conversion". In: *Physical Review A* 50 (1994), p. 3492. DOI: 10.1103/PhysRevA.50.3492.

[Dea07] S.R. Deans. *The Radon Transform and Some of Its Applications*. Dover Publications, 2007. ISBN: 9780486462417.

[DF00] E.M. Daly and A.I. Ferguson. "Parametric amplification and squeezing of a mode-locked pulse train: A comparison of MgO:$LiNbO_3$ with bulk periodically poled $LiNbO_3$". In: *Physical Review A* 62 (2000), p. 043807. DOI: 10.1103/PhysRevA.62.043807.

[Die+06] J.C. Diels, W. Rudolph, P.F. Liao, and P. Kelley. *Ultrashort Laser Pulse Phenomena*. 2nd ed. Elsevier Science, 2006. ISBN: 9780080466408.

[Din+17] S. Ding, G. Maslennikov, R. Hablützel, H. Loh, and D. Matsukevich. "Quantum Parametric Oscillator with Trapped Ions". In: *Physical Review Letters* 119 (2017), p. 150404. DOI: 10.1103/PhysRevLett.119.150404.

[DJ92] G. Drobný and I. Jex. "Quantum properties of field modes in trilinear optical processes". In: *Physical Review A* 46 (1992), p. 499. DOI: 10.1103/PhysRevA.46.499.

[DJB93] G. Drobný, I. Jex, and V. Bužek. "Mode entanglement in nondegenerate down-conversion with quantized pump". In: *Physical Review A* 48 (1993), p. 569. DOI: 10.1103/PhysRevA.48.569.

[DMP94] G.M. D'Ariano, C. Macchiavello, and M.G.A. Paris. "Detection of the density matrix through optical homodyne tomography without filtered back projection". In: *Physical Review A* 50 (1994), p. 4298. DOI: 10.1103/PhysRevA.50.4298.

[Dup+14] F. Dupuis, M. Berta, J. Wullschleger, and R. Renner. "One-Shot Decoupling". In: *Communications in Mathematical Physics* 328 (2014), p. 251. DOI: 10.1007/s00220-014-1990-4.

[Eck+11] A. Eckstein, A. Christ, P.J. Mosley, and C. Silberhorn. "Highly Efficient Single-Pass Source of Pulsed Single-Mode Twin Beams of Light". In: *Physical Review Letters* 106 (2011), p. 013603. DOI: 10.1103/PhysRevLett.106.013603.

[ED01] M. Ebrahimzadeh and M.H. Dunn. "Optical Parametric Oscillators". In: *Handbook of Optics IV*. McGraw-Hill, 2001, p. 22.49. DOI: 10.1036/0071414797.

[Eic+11] C. Eichler, D. Bozyigit, C. Lang, L. Steffen, J. Fink, and A. Wallraff. "Experimental State Tomography of Itinerant Single Microwave Photons". In: *Physical Review Letters* 106 (2011), p. 220503. DOI: 10.1103/PhysRevLett.106.220503.

[EPR35] A. Einstein, B. Podolsky, and N. Rosen. "Can Quantum-Mechanical Description of Physical Reality Be Considered Complete?" In: *Physical Review* 47 (1935), p. 777. DOI: 10.1103/PhysRev.47.777.

[FF05] L. Ferrarese and H. Ford. "Supermassive Black Holes in Galactic Nuclei: Past, Present and Future Research". In: *Space Science Reviews* 116 (2005), p. 523. DOI: 10.1007/s11214-005-3947-6.

[Fl18a] J. Flórez, N.J. Carlson, C.H. Nacke, L. Giner, and J.S. Lundeen. "A variable partially polarizing beam splitter". In: *Review of Scientific Instruments* 89 (2018), p. 023108. DOI: 10.1063/1.5004805.

[Fl18b] J. Flórez, E. Giese, D. Curic, L. Giner, R.W. Boyd, and J.S. Lundeen. "The phase sensitivity of a fully quantum three-mode nonlinear interferometer". In: *New Journal of Physics* 20 (2018), p. 123022. DOI: 10.1088/1367-2630/aaf3d2.

[FLC20] J. Flórez, J.S. Lundeen, and M.V. Chekhova. "Pump depletion in parametric down-conversion with low pump energies". In: *Optics Letters* 45 (2020), p. 4264. DOI: 10.1364/OL.394925.

[FP99] C. Fabry and A. Pérot. "Théorie et applications d'une nouvelle méthode de spectroscopie interférentielle". In: *Annales de chimie et de physique* 7 (1899), p. 115.

[FSSMF01] M. França Santos, E. Solano, and R.L. de Matos Filho. "Conditional Large Fock State Preparation and Field State Reconstruction in Cavity QED". In: *Physical Review Letters* 87 (2001), p. 093601. DOI: 10.1103/PhysRevLett.87.093601.

[FT20] C. Fabre and N. Treps. "Modes and states in quantum optics". In: *Review of Modern Physics* 92 (2020), p. 035005. DOI: 10.1103/RevModPhys.92.035005.

[G&21] G&H. *Periodically-Poled Lithium Niobate (PPLN)*. Apr. 2021. URL: https://gandh.com/product-categories/periodically-poled-lithium-niobate/.

[Gay+08] O. Gayer, Z. Sacks, E. Galun, and A. Arie. "Temperature and wavelength dependent refractive index equations for MgO-doped congruent and stoichiometric $LiNbO_3$". In: *Applied Physics B* 91 (2008), p. 343. DOI: 10.1007/s00340-008-2998-2.

[GEG10] R. Genzel, F. Eisenhauer, and S. Gillessen. "The Galactic Center massive black hole and nuclear star cluster". In: *Reviews of Modern Physics* 82 (2010), p. 3121. DOI: 10.1103/RevModPhys.82.3121.

[Gen16] M. Genovese. "Real applications of quantum imaging". In: *Journal of Optics* 18 (2016), p. 073002. DOI: 10.1088/2040-8978/18/7/073002.

[Ghe+08] A.M. Ghez et al. "Measuring Distance and Properties of the Milky Way's Central Supermassive Black Hole with Stellar Orbits". In: *The Astrophysical Journal* 689 (2008), p. 1044. DOI: 10.1086/592738.

[Gie+17] E. Giese, S. Lemieux, M. Manceau, R. Fickler, and R.W. Boyd. "Phase sensitivity of gain-unbalanced nonlinear interferometers". In: *Physical Review A* 96 (2017), p. 053863. DOI: 10.1103/PhysRevA.96.053863.

[Gil+09] S. Gillessen, F. Eisenhauer, S. Trippe, T. Alexander, R. Genzel, F. Martins, and T. Ott. "MONITORING STELLAR ORBITS AROUND THE MASSIVE BLACK HOLE IN THE GALACTIC CENTER". In: *The Astrophysical Journal* 692 (2009), p. 1075. DOI: 10.1088/0004-637x/692/2/1075.

[Giu+15] M. Giustina et al. "Significant-Loophole-Free Test of Bell's Theorem with Entangled Photons". In: *Physical Review Letters* 115 (2015), p. 250401. DOI: 10.1103/PhysRevLett.115.250401.

[GK04] C. Gerry and P. Knight. *Introductory Quantum Optics*. Cambridge University Press, 2004. DOI: 10.1017/CBO9780511791239.

[Gla63] R.J. Glauber. "Coherent and Incoherent States of the Radiation Field". In: *Physical Review* 131 (1963), p. 2766. DOI: 10.1103/PhysRev.131.2766.

[GLM11] V. Giovannetti, S. Lloyd, and L. Maccone. "Advances in quantum metrology". In: *Nature Photonics* 5 (2011), p. 222. DOI: 10.1038/nphoton.2011.35.

[GPS15] M. Gabbrielli, L. Pezzè, and A. Smerzi. "Spin-Mixing Interferometry with Bose-Einstein Condensates". In: *Physical Review Letters* 115 (2015), p. 163002. DOI: 10.1103/PhysRevLett.115.163002.

[Han+01] H. Hansen, T. Aichele, C. Hettich, P. Lodahl, A.I. Lvovsky, J. Mlynek, and S. Schiller. "Ultrasensitive pulsed, balanced homodyne detector: application to time-domain quantum measurements". In: *Optics Letters* 26 (2001), p. 1714. DOI: 10.1364/OL.26.001714.

[Haw67] S.W. Hawking. "The Occurrence of Singularities in Cosmology. III. Causality and Singularities". In: *Proceedings of the Royal Society of London. Series A, Mathematical and Physical Sciences* 300 (1967), p. 187. URL: http://www.jstor.org/stable/2415769.

[Haw74] S.W. Hawking. "Black hole explosions?" In: *Nature* 248 (1974), p. 30. DOI: 10.1038/248030a0.

[Haw75] S.W. Hawking. "Particle creation by black holes". In: *Communications in Mathematical Physics* 43 (1975), p. 199. DOI: 10.1007/BF02345020.

[Haw78] S.W. Hawking. "Quantum gravity and path integrals". In: *Physical Review D* 18 (1978), p. 1747. DOI: 10.1103/PhysRevD.18.1747.

[Hec17] E. Hecht. *Optics*. 5th ed. Pearson Education, 2017. ISBN: 9780133977226.

[Hew+68] A. Hewish, S.J. Bell, J.D.H. Pilkington, P.F. Scott, and R.A. Collins. "Observation of a Rapidly Pulsating Radio Source". In: *Nature* 217 (1968), p. 709. DOI: 10.1038/217709a0.

[HIM20] K. Hashimoto, N. Iizuka, and Y. Matsuo. "Islands in Schwarzschild black holes". In: *Journal of High Energy Physics* 2020 (2020), p. 85. DOI: 10.1007/JHEP06(2020)085.

[HM90] T. Hirano and M. Matsuoka. "Broadband squeezing of light by pulse excitation". In: *Optics Letters* 15 (1990), p. 1153. DOI: 10.1364/OL.15.001153.

[HOB67] S.E. Harris, M.K. Oshman, and R.L. Byer. "Observation of Tunable Optical Parametric Fluorescence". In: *Physical Review Letters* 18 (18 1967), p. 732. DOI: 10.1103/PhysRevLett.18.732.

[HOM87] C.K. Hong, Z.Y. Ou, and L. Mandel. "Measurement of subpicosecond time intervals between two photons by interference". In: *Physical Review Letters* 59 (1987), p. 2044. DOI: 10.1103/PhysRevLett.59.2044.

[How+14] M. Howard, J. Wallman, V. Veitch, and J. Emerson. "Contextuality supplies the 'magic' for quantum computation". In: *Nature* 510 (2014), p. 351. DOI: 10.1038/nature13460.

[Hra97] Z. Hradil. "Quantum-state estimation". In: *Physical Review A* 55 (1997), R1561. DOI: 10.1103/PhysRevA.55.R1561.

[Hud+14] F. Hudelist, J. Kong, C. Liu, J. Jing, Z.Y. Ou, and W. Zhang. "Quantum metrology with parametric amplifier-based photon correlation interferometers". In: *Nature Communications* 5 (2014). DOI: 10.1038/ncomms4049.

[Hud74] R.L. Hudson. "When is the Wigner quasi-probability density non-negative?" In: *Reports on Mathematical Physics* 6 (1974), p. 249. DOI: https://doi.org/10.1016/0034-4877(74)90007-X.

[Hus40] K. Husimi. "Some Formal Properties of the Density Matrix". In: *Proceedings of the Physico-Mathematical Society of Japan. 3rd Series* 22 (1940), p. 264. DOI: 10.11429/ppmsj1919.22.4_264.

[İ+67] K. İmre, E. Özizmir, M. Rosenbaum, and P.F. Zweifel. "Wigner Method in Quantum Statistical Mechanics". In: *Journal of Mathematical Physics* 8 (1967), p. 1097. DOI: 10.1063/1.1705323.

[ICL09] T. Iskhakov, M.V. Chekhova, and G. Leuchs. "Generation and Direct Detection of Broadband Mesoscopic Polarization-Squeezed Vacuum". In: *Physical Review Letters* 102 (2009), p. 183602. DOI: 10.1103/PhysRevLett.102.183602.

[Isk+12a] T.Sh. Iskhakov, I.N. Agafonov, M.V. Chekhova, and G. Leuchs. "Polarization-Entangled Light Pulses of 10^5 Photons". In: *Physical Review Letters* 109 (2012), p. 150502. DOI: 10.1103/PhysRevLett.109.150502.

[Isk+12b] T.Sh. Iskhakov, A.M. Pérez, K.Yu. Spasibko, M.V. Chekhova, and G. Leuchs. "Superbunched bright squeezed vacuum state". In: *Optics Letters* 37 (2012), p. 1919. DOI: 10.1364/OL.37.001919.

[Iva+06] O.A. Ivanova, T.Sh. Iskhakov, A.N. Penin, and M.V. Chekhova. "Multiphoton correlations in parametric down-conversion and their measurement in the pulsed regime". In: *Quantum Electronics* 36 (2006), p. 951. DOI: 10.1070/qe2006v036n10abeh013300.

[Jam+01] D.F.V. James, P.G. Kwiat, W.J. Munro, and A.G. White. "Measurement of qubits". In: *Physical Review A* 64 (2001), p. 052312. DOI: 10.1103/PhysRevA.64.052312.

[Jan32] K.G. Jansky. "Directional Studies of Atmospherics at High Frequencies". In: *Proceedings of the Institute of Radio Engineers* 20 (1932), p. 1920. DOI: 10.1109/JRPROC.1932.227477.

[Jan33] K.G. Jansky. "Electrical Disturbances Apparently of Extraterrestrial Origin". In: *Proceedings of the Institute of Radio Engineers* 21 (1933), p. 1387. DOI: 10.1109/JRPROC.1933.227458.

[JNN12] J.R. Johansson, P.D. Nation, and F. Nori. "QuTiP: An open-source Python framework for the dynamics of open quantum systems". In: *Computer Physics Communications* 183 (2012), p. 1760. DOI: 10.1016/j.cpc.2012.02.021.

[JNN13] J.R. Johansson, P.D. Nation, and F. Nori. "QuTiP 2: A Python framework for the dynamics of open quantum systems". In: *Computer Physics Communications* 184 (2013), p. 1234. DOI: 10.1016/j.cpc.2012.11.019.

[JWK20] M.J. Jacquet, S. Weinfurtner, and F. König. "The next generation of analogue gravity experiments". In: *Philosophical Transactions of the Royal Society A: Mathematical, Physical and Engineering Sciences* 378 (2020), p. 20190239. DOI: 10.1098/rsta.2019.0239.

[Kal+16] D.A. Kalashnikov, A.V. Paterova, S.P. Kulik, and L.A. Krivitsky. "Infrared spectroscopy with visible light". In: *Nature Photonics* 10 (2016), p. 98. DOI: 10.1038/nphoton.2015.252.

[Ker63] R.P. Kerr. "Gravitational Field of a Spinning Mass as an Example of Algebraically Special Metrics". In: *Physical Review Letters* 11 (1963), p. 237. DOI: 10.1103/PhysRevLett.11.237.

[KLM01] E. Knill, R. Laflamme, and G.J. Milburn. "A scheme for efficient quantum computation with linear optics". In: *Nature* 409 (2001), p. 46. DOI: 10.1038/35051009.

[Kly88] D.N. Klyshko. *Photons and Nonlinear Optics*. Gordon and Breach Science Publishers, 1988. ISBN: 9782881246692.

[KR95] J. Kormendy and D. Richstone. "Inward Bound—The Search for Supermassive Black Holes in Galactic Nuclei". In: *Annual Review of Astronomy and Astrophysics* 33 (1995), p. 581. DOI: 10.1146/annurev.aa.33.090195.003053.

[KS88] A.C. Kak and M. Slaney. *Principles of Computerized Tomographic Imaging*. IEEE Press, 1988. ISBN: 9780898714944.

[Lah+10] O. Lahav, A. Itah, A. Blumkin, C. Gordon, S. Rinott, A. Zayats, and J. Steinhauer. "Realization of a Sonic Black Hole Analog in a Bose-Einstein Condensate". In: *Physics Review Letters* 105 (2010), p. 240401. DOI: 10.1103/PhysRevLett.105.240401.

[LB02] A.I. Lvovsky and S.A. Babichev. "Synthesis and tomographic characterization of the displaced Fock state of light". In: *Physical Review A* 66 (2002), p. 011801. DOI: 10.1103/PhysRevA.66.011801.

[Lee95] H.-W. Lee. "Theory and application of the quantum phase-space distribution functions". In: *Physics Reports* 259 (1995), p. 147. DOI: https://doi.org/10.1016/0370-1573(95)00007-4.

[Lei+96] D. Leibfried, D.M. Meekhof, B.E. King, C. Monroe, W.M. Itano, and D.J. Wineland. "Experimental Determination of the Motional Quantum State of a Trapped Atom". In: *Physical Review Letters* 77 (1996), p. 4281. DOI: 10.1103/PhysRevLett.77.4281.

[Lem+16] S. Lemieux, M. Manceau, P.R. Sharapova, O.V. Tikhonova, R.W. Boyd, G. Leuchs, and M.V. Chekhova. "Engineering the Frequency Spectrum of Bright Squeezed Vacuum via Group Velocity Dispersion in an SU(1,1) Interferometer". In: *Physical Review Letters* 117 (2016), p. 183601. DOI: 10.1103/PhysRevLett.117.183601.

[Lem+19] S. Lemieux, E. Giese, R. Fickler, M.V. Chekhova, and R.W. Boyd. "A primary radiation standard based on quantum nonlinear optics". In: *Nature Physics* 15 (2019), p. 529. DOI: 10.1038/s41567-019-0447-2.

[Leo10] U. Leonhardt. *Essential Quantum Optics. From Quantum Measurements to Black Holes*. Cambridge University Press, 2010. ISBN: 9780521869782.

[Leo+96] U. Leonhardt, M. Munroe, T. Kiss, Th. Richter, and M.G. Raymer. "Sampling of photon statistics and density matrix using homodyne detection". In: *Optics Communications* 127 (1996), p. 144. DOI: https://doi.org/10.1016/0030-4018(96)00061-2.

[Li+14] D. Li, C.-H. Yuan, Z.Y. Ou, and W. Zhang. "The phase sensitivity of an SU(1,1) interferometer with coherent and squeezed-vacuum light". In: *New Journal of Physics* 16 (2014), p. 073020. DOI: 10.1088/1367-2630/16/7/073020.

[Lig] *Etalon Designer - User's Guide*. Accessed: 2020-07-31. URL: https://lightmachinery.com/optical-design-center/etalon-designer/.

[Lin+16] D. Linnemann, H. Strobel, W. Muessel, J. Schulz, R.J. Lewis-Swan, K.V. Kheruntsyan, and M.K. Oberthaler. "Quantum-Enhanced Sensing Based on Time Reversal of Nonlinear Dynamics". In: *Physical Review Letters* 117 (2016), p. 013001. DOI: 10.1103/PhysRevLett.117.013001.

[LKD02] H. Lee, P. Kok, and J.P. Dowling. "A quantum Rosetta stone for interferometry". In: *Journal of Modern Optics* 49 (2002), p. 2325. DOI: 10.1080/0950034021000011536.

[LM02] A.I. Lvovsky and J. Mlynek. "Quantum-Optical Catalysis: Generating Nonclassical States of Light by Means of Linear Optics". In: *Physical Review Letters* 88 (2002), p. 250401. DOI: 10.1103/PhysRevLett.88.250401.

[LoP03] M.C. LoPresto. "Some Simple Black Hole Thermodynamics". In: *The Physics Teacher* 41 (2003), p. 299. DOI: 10.1119/1.1571268.

[Lou00] R. Loudon. *The Quantum Theory of Light*. Oxford University Press, 2000. ISBN: 9780198501763.

[Lvo+01] A.I. Lvovsky, H. Hansen, T. Aichele, O. Benson, J. Mlynek, and S. Schiller. "Quantum State Reconstruction of the Single-Photon Fock State". In: *Physical Review Letters* 87 (2001), p. 050402. DOI: 10.1103/PhysRevLett.87.050402.

[Lvo04] A I Lvovsky. "Iterative maximum-likelihood reconstruction in quantum homodyne tomography". In: *Journal of Optics B: Quantum and Semiclassical Optics* 6 (2004), S556. DOI: 10.1088/1464-4266/6/6/014.

[LYS61] W.H. Louisell, A. Yariv, and A.E. Siegman. "Quantum Fluctuations and Noise in Parametric Processes. I." In: *Physical Review* 124 (1961), p. 1646. DOI: 10.1103/PhysRev.124.1646.

[Mal99] J. Maldacena. "The Large-N Limit of Superconformal Field Theories and Supergravity". In: *International Journal of Theoretical Physics* 38 (1999), p. 1113. DOI: 10.1023/A:1026654312961.

[Man+17] M. Manceau, G. Leuchs, F. Khalili, and M.V. Chekhova. "Detection Loss Tolerant Supersensitive Phase Measurement with an SU(1,1) Interferometer". In: *Physical Review Letters* 119 (2017), p. 223604. DOI: 10.1103/PhysRevLett.119.223604.

[MD04] X. Mu and Y.J. Ding. "Investigation of one of the most fundamental limits to parametric processes: two-photon absorption". In: *Optics Communications* 242 (2004), p. 305. DOI: 10.1016/j.optcom.2004.08.026.

[Mey+01] V. Meyer, M.A. Rowe, D. Kielpinski, C.A. Sackett, W.M. Itano, C. Monroe, and D.J. Wineland. "Experimental Demonstration of Entanglement-Enhanced Rotation Angle Estimation Using Trapped Ions". In: *Physical Review Letters* 86 (2001), p. 5870. DOI: 10.1103/PhysRevLett.86.5870.

[MG67] B.R. Mollow and R.J. Glauber. "Quantum Theory of Parametric Amplification. I". In: *Physical Review* 160 (1967), p. 1076. DOI: 10.1103/PhysRev.160.1076.

[Moy49] J.E. Moyal. "Quantum mechanics as a statistical theory". In: *Mathematical Proceedings of the Cambridge Philosophical Society* 45 (1949), p. 99. DOI: 10.1017/S0305004100000487.

[MR56] J.M. Manley and H.E. Rowe. "Some General Properties of Nonlinear Elements-Part I. General Energy Relations". In: *Proceedings of the IRE* 44 (1956), p. 904. DOI: 10.1109/JRPROC.1956.275145.

[MTW73] C.W. Misner, K.S. Thorne, and J.A. Wheeler. *Gravitation*. W.H. Freeman and Company, 1973. ISBN: 9780716703440.

[Nas+03] M.B. Nasr, B.E.A. Saleh, A.V. Sergienko, and M.C. Teich. "Demonstration of Dispersion-Canceled Quantum-Optical Coherence Tomography". In: *Physical Review Letters* 91 (2003), p. 083601. DOI: 10.1103/PhysRevLett.91.083601.

[Nat+12] P.D. Nation, J.R. Johansson, M.P. Blencowe, and F. Nori. "Colloquium: Stimulating uncertainty: Amplifying the quantum vacuum with superconducting circuits". In: *Reviews of Modern Physics* 84 (2012), p. 1. DOI: 10.1103/RevModPhys.84.1.

[NB10] P.D. Nation and M.P. Blencowe. "The trilinear Hamiltonian: a zero-dimensional model of Hawking radiation from a quantized source". In: *New Journal of Physics* 12 (2010), p. 095013. DOI: 10.1088/1367-2630/12/9/095013.

[NC00] M.A. Nielsen and I.L. Chuang. *Quantum Computation and Quantum Information*. Cambridge University Press, 2000. DOI: 10.1017/CBO9780511976667.

[New+65] E.T. Newman, E. Couch, K. Chinnapared, A. Exton, A. Prakash, and R. Torrence. "Metric of a Rotating, Charged Mass". In: *Journal of Mathematical Physics* 6 (1965), p. 918. DOI: 10.1063/1.1704351.

[OKL02] T. Opatrný, N. Korolkova, and G. Leuchs. "Mode structure and photon number correlations in squeezed quantum pulses". In: *Physical Review A* 66 (2002), p. 053813. DOI: 10.1103/PhysRevA.66.053813.

[OL20] Z.Y. Ou and X. Li. "Quantum SU(1,1) interferometers: Basic principles and applications". In: *APL Photonics* 5 (2020), p. 080902. DOI: 10.1063/5.0004873.

[Ono+19] T. Ono, G.F. Sinclair, D. Bonneau, M.G. Thompson, J.C.F. Matthews, and J.G. Rarity. "Observation of nonlinear interference on a silicon photonic chip". In: *Optics Letters* 44 (2019), p. 1277. DOI: 10.1364/OL.44.001277.

[OTBG06] A. Ourjoumtsev, R. Tualle-Brouri, and P. Grangier. "Quantum Homodyne Tomography of a Two-Photon Fock State". In: *Physical Review Letters* 96 (2006), p. 213601. DOI: 10.1103/PhysRevLett.96.213601.

[Ou96] Z.Y. Ou. "Complementarity and Fundamental Limit in Precision Phase Measurement". In: *Physical Review Letters* 77 (1996), p. 2352. DOI: 10.1103/PhysRevLett.77.2352.

[Pag05] D.N. Page. "Hawking radiation and black hole thermodynamics". In: *New Journal of Physics* 7 (2005), p. 203. DOI: 10.1088/1367-2630/7/1/203.

[Pag13] D.N. Page. "Time dependence of Hawking radiation entropy". In: *Journal of Cosmology and Astroparticle Physics* 2013 (2013), p. 028. DOI: 10.1088/1475-7516/2013/09/028.

[Pag93] D.N. Page. "Information in black hole radiation". In: *Physical Review Letters* 71 (1993), p. 3743. DOI: 10.1103/PhysRevLett.71.3743.

[PDA10] W.N. Plick, J.P. Dowling, and G.S. Agarwal. "Coherent-light-boosted, sub-shot noise, quantum interferometry". In: *New Journal of Physics* 12 (2010), p. 083014. DOI: 10.1088/1367-2630/12/8/083014.

[Pen+19] G. Penington, S.H. Shenker, D. Stanford, and Z. Yang. "Replica wormholes and the black hole interior". In: *arXiv e-prints* (2019), arXiv:1911.11977. arXiv: 1911.11977 [hep-th].

[Pen20] G. Penington. "Entanglement wedge reconstruction and the information paradox". In: *Journal of High Energy Physics* 2020 (2020), p. 2. DOI: 10.1007/JHEP09(2020)002.

[Pen65] R. Penrose. "Gravitational Collapse and Space-Time Singularities". In: *Physical Review Letters* 14 (1965), p. 57. DOI: 10.1103/PhysRevLett.14.57.

[Phi+08] T.G. Philbin, C. Kuklewicz, S. Robertson, S. Hill, F. König, and U. Leonhardt. "Fiber-Optical Analog of the Event Horizon". In: *Science* 319 (2008), p. 1367. DOI: 10.1126/science.1153625.

[Pit+95] T.B. Pittman, Y.H. Shih, D.V. Strekalov, and A.V. Sergienko. "Optical imaging by means of two-photon quantum entanglement". In: *Physical Review A* 52 (1995), R3429. DOI: 10.1103/PhysRevA.52.R3429.

[PJ+16] J. Peřina Jr., O. Haderka, A. Allevi, and M. Bondani. "Internal dynamics of intense twin beams and their coherence". In: *Scientific Reports* 6 (2016), p. 22320. DOI: 10.1038/srep22320.

[Rab+72] T.A. Rabson, H.J. Ruiz, P.L. Shah, and F.K. Tittel. "Stimulated parametric fluorescence induced by picosecond pump pulses". In: *Applied Physics Letters* 21 (1972), p. 129. DOI: 10.1063/1.1654312.

[Rad17] J. Radon. "Über die Bestimmung von Funktionen durch ihre Integralwerte längs gewisser Mannigfaltigkeiten". In: *Berichte über die Verhandlungen der Königlich-Sächsischen Gesellschaft der Wissenschaften zu Leipzig, Mathematisch-Physische Klasse* 69 (1917), p. 262.

[RB04] M.G. Raymer and M. Beck. "7 Experimental Quantum State Tomography of Optical Fields and Ultrafast Statistical Sampling". In: *Quantum State Estimation*. Ed. by M. Paris and J. Řeháček. Springer Berlin Heidelberg, 2004, p. 235. ISBN: 9783540444817. DOI: 10.1007/978-3-540-44481-7_7.

[RGN03] W.P. Risk, T.R. Gosnell, and A.V. Nurmikko. *Compact Blue-Green Lasers*. Cambridge University Press, 2003. DOI: 10.1017/CBO9780511606502.

[Rou+08] G. Rousseaux, C. Mathis, P. Maïssa, T.G. Philbin, and U. Leonhardt. "Observation of negative-frequency waves in a water tank: a classical analogue to the Hawking effect?" In: *New Journal of Physics* 10 (2008), p. 053015. DOI: 10.1088/1367-2630/10/5/053015.

[SB12] J.H. Shapiro and R.W. Boyd. "The physics of ghost imaging". In: *Quantum Information Processing* 11 (2012), p. 949. DOI: 10.1007/s11128-011-0356-5.

[SC83] F. Soto and P. Claverie. "When is the Wigner function of multidimensional systems nonnegative?" In: *Journal of Mathematical Physics* 24 (1983), p. 97. DOI: 10.1063/1.525607.

[Sch01] W.P. Schleich. *Quantum Optics in Phase Space*. Wiley-VCH, 2001. DOI: 10.1002/3527602976.

[Sch16a] K. Schwarzschild. "Über das Gravitationsfeld einer Kugel aus inkompressibler Flüssigkeit". In: *Sitzungsberichte der Königlich Preussischen Akademie der Wissenschaften* 7 (1916), p. 189.

[Sch16b] K. Schwarzschild. "Über das Gravitationsfeld eines Massenpunktes nach der Einsteinschen Theorie". In: *Sitzungsberichte der Königlich Preussischen Akademie der Wissenschaften* 7 (1916), p. 189.

[Sha+13] Y. Shalibo, R. Resh, O. Fogel, D. Shwa, R. Bialczak, J.M. Martinis, and N. Katz. "Direct Wigner Tomography of a Superconducting Anharmonic Oscillator". In: *Physical Review Letters* 110 (2013), p. 100404. DOI: 10.1103/PhysRevLett.110.100404.

[Sha+15] L.K. Shalm et al. "Strong Loophole-Free Test of Local Realism". In: *Physical Review Letters* 115 (2015), p. 250402. DOI: 10.1103/PhysRevLett.115.250402.

[Shi12] Y. Shih. "The physics of ghost imaging: nonlocal interference or local intensity fluctuation correlation?" In: *Quantum Information Processing* 11 (2012), p. 995. DOI: 10.1007/s11128-012-0396-5.

[SJS17] D.S. Simon, G. Jaeger, and A.V. Sergienko. "Quantum Metrology". In: *Quantum Metrology, Imaging, and Communication*. 2017, p. 91. DOI: 10.1007/978-3-319-46551-7_4.

[Slu+17] S. Slussarenko, M.M. Weston, H.M. Chrzanowski, L.K. Shalm, V.B. Verma, S.W. Nam, and G.J. Pryde. "Unconditional violation of the shot-noise limit in photonic quantum metrology". In: *Nature Photonics* 11 (2017), p. 700. DOI: 10.1038/s41566-017-0011-5.

[Slu+85] R.E. Slusher, L.W. Hollberg, B. Yurke, J.C. Mertz, and J.F. Valley. "Observation of Squeezed States Generated by Four-Wave Mixing in an Optical Cavity". In: *Physical Review Letters* 55 (1985), p. 2409. DOI: 10.1103/PhysRevLett.55.2409.

[Smi+92] D.T. Smithey, M. Beck, M. Belsley, and M.G. Raymer. "Sub-shot-noise correlation of total photon number using macroscopic twin pulses of light". In: *Physical Review Letters* 69 (1992), p. 2650. DOI: 10.1103/PhysRevLett.69.2650.

[Smi+93a] D.T. Smithey, M. Beck, J. Cooper, and M.G. Raymer. "Measurement of number-phase uncertainty relations of optical fields". In: *Physical Review A* 48 (1993), p. 3159. DOI: 10.1103/PhysRevA.48.3159.

[Smi+93b] D.T. Smithey, M. Beck, M.G. Raymer, and A. Faridani. "Measurement of the Wigner distribution and the density matrix of a light mode using optical homodyne tomography: Application to squeezed states and the vacuum". In: *Physical Review Letters* 70 (1993), p. 1244. DOI: 10.1103/PhysRevLett.70.1244.

[Spe08] R.W. Spekkens. "Negativity and Contextuality are Equivalent Notions of Nonclassicality". In: *Physical Review Letters* 101 (2008), p. 020401. DOI: 10.1103/PhysRevLett.101.020401.

[Sri+14] N. Sridhar, R. Shahrokhshahi, A.J. Miller, B. Calkins, T. Gerrits, A. Lita, S.W. Nam, and O. Pfister. "Direct measurement of the Wigner function by photon-number-resolving detection". In: *Journal of the Optical Society of America B* 31.10 (2014), B34. DOI: 10.1364/JOSAB.31.000B34.

[Str+95] D.V. Strekalov, A.V. Sergienko, D.N. Klyshko, and Y.H. Shih. "Observation of Two-Photon "Ghost" Interference and Diffraction". In: *Physical Review Letters* 74 (1995), p. 3600. DOI: 10.1103/PhysRevLett.74.3600.

[Sud63] E.C.G. Sudarshan. "Equivalence of Semiclassical and Quantum Mechanical Descriptions of Statistical Light Beams". In: *Physical Review Letters* 10 (1963), p. 277. DOI: 10.1103/PhysRevLett.10.277.

[Tak65] H. Takahasi. "Information Theory of Quantum-Mechanical Channels". In: ed. by A.V. Balakrishnan. Vol. 1. Advances in Communication Systems. Elsevier, 1965, pp. 227–310. DOI: https://doi.org/10.1016/B978-1-4832-2938-6.50011-8.

[The+18] G.S. Thekkadath, L. Giner, X. Ma, J. Flórez, and J.S. Lundeen. "Projecting onto any two-photon polarization state using linear optics". In: *New Journal of Physics* 20 (2018), p. 083033. DOI: 10.1088/1367-2630/aad9b9.

[Tse+19] M. Tse et al. "Quantum-Enhanced Advanced LIGO Detectors in the Era of Gravitational-Wave Astronomy". In: *Physics Review Letters* 123 (2019), p. 231107. DOI: 10.1103/PhysRevLett.123.231107.

[TW69] J. Tucker and D.F. Walls. "Quantum Theory of the Traveling-Wave Frequency Converter". In: *Physical Review* 178 (1969), p. 2036. DOI: 10.1103/PhysRev.178.2036.

[Urs+07] R. Ursin et al. "Entanglement-based quantum communication over 144 km". In: *Nature Physics* 3 (2007), p. 481. DOI: 10.1038/nphys629.

[Val+05] A. Valencia, G. Scarcelli, M. D'Angelo, and Y. Shih. "Two-Photon Imaging with Thermal Light". In: *Physical Review Letters* 94 (2005). DOI: 10.1103/physrevlett.94.063601.

[Val58] J.G. Valatin. "Comments on the theory of superconductivity". In: *Il Nuovo Cimento* 7 (1958), p. 843. DOI: 10.1007/bf02745589.

[Vet+16] A. Vetter et al. "Cavity-Enhanced and Ultrafast Superconducting Single-Photon Detectors". In: *Nano Letters* 16 (2016), p. 7085. DOI: 10.1021/acs.nanolett.6b03344.

[VR89] K. Vogel and H. Risken. "Determination of quasiprobability distributions in terms of probability distributions for the rotated quadrature phase". In: *Physical Review A* 40 (1989), p. 2847. DOI: 10.1103/PhysRevA.40.2847.

[Wal70] D.F. Walls. "Quantum versus classical analysis of 2nd harmonic generation". In: *Physics Letters A* 32 (1970), p. 476. DOI: 10.1016/0375-9601(70)90459-7.

[WB70] D.F. Walls and R. Barakat. "Quantum-Mechanical Amplification and Frequency Conversion with a Trilinear Hamiltonian". In: *Physical Review A* 1 (1970), p. 446. DOI: 10.1103/PhysRevA.1.446.

[Wei+11] S. Weinfurtner, E.W. Tedford, M.C.J. Penrice, W.G. Unruh, and G.A. Lawrence. "Measurement of Stimulated Hawking Emission in an Analogue System". In: *Physics Review Letters* 106 (2011), p. 021302. DOI: 10.1103/PhysRevLett.106.021302.

[Wey27] H. Weyl. "Quantenmechanik und Gruppentheorie". In: *Zeitschrift für Physik* 46 (1927), p. 1. DOI: 10.1007/BF02055756.

[Wig32] E. Wigner. "On the Quantum Correction For Thermodynamic Equilibrium". In: *Physical Review* 40 (1932), p. 749. DOI: 10.1103/PhysRev.40.749.

[WM08] D.F. Walls and G.J. Milburn. *Quantum Optics*. 2nd ed. Springer-Verlag, 2008.

[WM72] B.L. Webster and P. Murdin. "Cygnus X-1—a Spectroscopic Binary with a Heavy Companion?" In: *Nature* 235 (1972), p. 37. DOI: 10.1038/235037a0.

[Wu+86] L.-A. Wu, H.J. Kimble, J.L. Hall, and H. Wu. "Generation of Squeezed States by Parametric Down Conversion". In: *Physical Review Letter* 57 (1986), p. 2520. DOI: 10.1103/PhysRevLett.57.2520.

[XWJ16] J. Xin, H. Wang, and J. Jing. "The effect of losses on the quantum-noise cancellation in the SU(1,1) interferometer". In: *Applied Physics Letters* 109 (2016), p. 051107. DOI: 10.1063/1.4960585.

[YC83] H.P. Yuen and V.W.S. Chan. "Noise in homodyne and heterodyne detection". In: *Optics Letters* 8 (1983), p. 177. DOI: 10.1364/OL.8.000177.

[YMK86] B. Yurke, S.L. McCall, and J.R. Klauder. "SU(2) and SU(1,1) interferometers". In: *Physical Review A* 33 (1986), p. 4033. DOI: 10.1103/PhysRevA.33.4033.

[YP87] B. Yurke and M. Potasek. "Obtainment of thermal noise from a pure quantum state". In: *Physical Review A* 36 (1987), p. 3464. DOI: 10.1103/PhysRevA.36.3464.

[Zam+05] G. Zambra, A. Andreoni, M. Bondani, M. Gramegna, M. Genovese, G. Brida, A. Rossi, and M.G.A. Paris. "Experimental Reconstruction of Photon Statistics without Photon Counting". In: *Physical Review Letters* 95 (2005), p. 063602. DOI: 10.1103/PhysRevLett.95.063602.

[Zav+02] A. Zavatta, M. Bellini, P.L. Ramazza, F. Marin, and F.T. Arecchi. "Time-domain analysis of quantum states of light: noise characterization and homodyne tomography". In: *Journal of the Optical Society of America B* 19 (2002), p. 1189. DOI: 10.1364/JOSAB.19.001189.